Simulation of the Deformation Behaviour of Two-phase Composites

Dissertation
zur Erlangung des akademischen Grades

Doktoringenieurin

(Dr.-Ing.)

von MSc. Yanling Schneider
geb. am 25.11.1976 in Langfang, V.R. China
genehmigt durch die Fakultät für Maschinenbau der Otto-von-Guericke-Universität Magdeburg

Gutachter:
Prof. Albrecht Bertram
Prof. Thomas Böhlke
Dr. Christian Hartig

Promotionskolloquium am 12.11.2007

Zusammenfassung

Mehrphasige metallische Verbundwerkstoffe werden häufig in der Automobilindustrie und der Luft- und Raumfahrt verwendet. In dieser Arbeit wird das mechanische Verhalten von mehrphasigen Werkstoffen am Beispiel von zwei-phasigen α-Eisen-Kupfer-Verbundwerkstoffen untersucht. Das Ziel der Arbeit ist es, das mechanische Verhalten von zweiphasigen Polykristallen und dabei insbesondere die Kopplung des Verformungsverhaltens auf der Mikro- und Makroebene bei großen plastischen Verformungen zu verstehen.

Es werden sieben Typen von Fe-Cu-Verbundwerkstoffen mit unterschiedlichem Phasenvolumenanteil untersucht. Fe-Cu Polykristalle zeichnen sich durch eine großen Inhomogenität und Anisotropie bei plastischen Verformungen aus. Zur Untersuchung der plastischen Eigenschaften der betrachteten Fe-Cu-Werkstoffe wird ein elastisch-viskoplastisches Materialmodell verwendet. Mit Hilfe der Finite-Elemente-Methode werden rotationssymmetrische und dreidimensionale Berechnungen durchgeführt. Für das rotationssymmetrische Modell dienen experimentelle Schliffbilder von Fe-Cu als Grundlage. Die 3D-Simulation basiert auf Poisson-Voronoi-Mikrostrukturen mit periodischen Randbedingungen. Es erfolgt ein Vergleich der numerischen Ergebnisse mit experimentellen Daten für das Fließverhalten, das lokale Deformationsverhalten, und die kristallographische Texturentwicklung.

Acknowledgments

I am very grateful to Prof. Dr.-Ing. A. Bertram for accepting me as a member of his team for the years of 2003-2006. The lectures, advice, and supervision of Prof. Dr.-Ing. Bertram and Prof. Dr.-Ing. T. Böhlke are genuinely appreciated. I am very grateful also to Dr.-Ing. Ch. Hartig for the experimental data that he provided. His advice and discussions for the understanding the experiments are highly evaluated.

My gratitude also goes to all my colleagues with whom I enjoyed academic discussions, in particular, I'd like to mention the help of Dipl-Ing. G. Risy. All such team work is highly appreciated. I have enjoyed the research atmosphere provided by the Graduiertenkolleg 828 very much.

I would also like to thank my relatives and my hushand for their encouragement to study abroad and for their help in overcoming the difficulties in doing so.

And last but not least, I am very grateful of the financial support of the Deutsche Forschungsgemeinschaft (DFG) under grant BE1455/10.

Contents

Chapter 1

Introduction

Multi-phase metals are widely applicable in the automobile and aerospace industries, since they can show good ductility, enhanced strength at elevated temperature, and improved corrosion resistance. To study the rather complex mechanical behaviour of such multi-phase materials, we investigate iron-copper polycrystalline composites as a model material. During the deformation process, the microstructure and its evolution are essential for the determination of the macroscopic mechanical behaviour of the aforementioned polycrystals. The main features of a microstructure are the geometry, the arrangement, and the orientation of the grains. The volume fraction of each phase and the interaction among grains are also important factors which influence the global material properties.

The main purpose of the present work is the investigation of mechanical properties of Fe-Cu composites and, particularly, the relationship between the local and macroscopic deformation behaviour under large plastic deformations. Due to the difference of the yield stresses of these two phases ($\sigma_{0.2}^{Fe} \approx 410$ MPa and $\sigma_{0.2}^{Cu} \approx 115$ MPa), both the stress and the strain field are highly heterogeneous. The harder phase shows higher stresses than the softer phase in such two-phase polycrystals (Raabe *et al.*, 1995; Soppa *et al.*, 1998; Commentz *et al.*, 1999). The softer phase has to undergo a larger local deformation which modifies the local stress field (Raabe *et al.*, 1995). The rule of mixture is insufficient to describe the stress-strain behaviour of the aforementioned composites. A reliable model is necessary to successfully describe the plastic behaviour of two-phase polycrystals. The Taylor model (Taylor, 1938) and the Sachs model (Sachs, 1928) are not suitable to predict the mechanical properties of such two-phase materials. In the Taylor model, the

assumption of a homogeneous strain field neglects the fact that the softer phase takes more deformation. The deformation field is essential for the analysis of the mechanical properties. The Sachs model assumes a homogeneous stress field in the grains of aggregates, which is not the case for the stress distribution in reality. These aforementioned two models take no interactions among grains and phases into account, which is important for the deformation process in two-phase polycrystals (Soppa *et al.*, 1998). A viscoplastic self-consistent model has been applied by Commentz *et al.* (1999) to study the mechanical behaviour of Fe-Cu composites, where the simulation results (compressive stress versus strain and rolling textures) are compared with the corresponding measurements. Since this model could not predict the texture development well, Commentz *et al.* (1999) suggested to use the finite element method in order to model the deformation behaviour of two-phase composites. This homogenization method allows for a local interaction of the grains and is able to more accurately describe the texture and the microstructure evolution.

In this work, the mechanical behaviour is simulated for pure iron, pure copper, and five of their composites which are Fe17vol.%-Cu83vol.%, Fe33vol.%-Cu67vol.%, Fe50vol.%-Cu50vol.%, Fe67vol.%-Cu33vol.% and Fe83vol.%-Cu17vol.%. For the first time, Commentz *et al.* (1999); Commentz (2000); Hartig and Mecking (2005); Daymond *et al.* (2005) investigated the complex plastic deformation of this type of composite. We introduce a mechanical approach based on finite elements to numerically study the properties of iron-copper composites and compare the results with experimental data (Commentz *et al.*, 1999; Commentz, 2000).

The outline of the present work is given as following. *Chapter 2* presents a brief description of applied materials, production of samples, and processes of tests including compression and tension (Commentz *et al.*, 1999; Commentz, 2000). The stress-strain data are obtained for pure iron, pure copper, and five of their composites under the compression test until 90% plastic strain. The texture of the iron and the copper phase are measured from the above compressively deformed samples at 90% plastic strain. The measurement of the local strain is performed in a tensile test at about 20% plastic strain.

In *Chapter 3*, the elasto-viscoplastic and the viscoplastic material model for single crystals are described by constitutive equations. The viscoplastic material model

with less internal variables is efficient with respect to the simulation time. The description of the material model begins with the elastic law. A short introduction to the crystal lattice and slip systems is followed by the discussion of the flow rule which is taken from finite crystal plasticity theory. The Kocks-Mecking hardening rule (Voce rule) is chosen, which puts emphasis on mechanisms of the dislocation movement, the accumulation, and the annealing (Kocks, 1976; Kocks and Mecking, 2003). This hardening rule is suitable for both the face-centered-cubic (fcc) and the body-centered-cubic (bcc) crystals.

Chapter 4 describes the homogenisation technique, which establishes the macroscopic material behaviour based on the constitutive equations of single crystals. A short discussion is given for the Taylor (Taylor, 1938), the Sachs (Sachs, 1928), and the modified (Taylor, Sachs) model. For the self-consistent model, we begin with the determination of the average elastic polycrystalline constants (Hershey and Dahlgren, 1954; Kröner, 1958) and give a brief view on the development of different self-consistent methods, e.g. Hill (1965); Budianski and Wu (1962); Berveiller and Zaoui (1979). Reasons are also presented for the preference of the finite element model to simulate mechanical properties of Fe-Cu composites in this work.

In *Chapter 5*, the material parameters are identified based on the experimental $\sigma-\varepsilon$ data in compression tests. The process is performed with the elasto-viscoplastic material law. The slip systems applied in the numerical simulation are discussed for both the iron and the copper phase.

Chapter 6 predicts the mechanical behaviour of Fe-Cu polycrystals using an axisymmetric finite element (FE) model. The Fe17-Cu83 and the Fe50-Cu50 composites are chosen as two examples. Real two-dimensional (2D) microscopic cut-outs are applied as cross-sections. Grain boundaries are meshed finer than other parts of microstructures, with the aim of investigating the local interaction. Since the meshing could not provide a corresponding node on the opposite side for each boundary node, homogeneous boundary conditions are used. We incorporate realistic morphologies (experimental 2D cut-outs as cross-sections) and grain orientations in the aforementioned model which is implemented in the FE software ABAQUS. A study of the local plastic deformation shows the flow behaviour and the misorientation of the iron and the copper phases. This chapter also gives a

prediction of the stress in each phase. Numerical results are compared with the experimental ones for the texture and the strain distribution for both phases.

Chapter 7 is aimed at enhancing and improving the numerical predictions of *Chapter 6*, in which periodic boundary conditions are used in the three-dimensional (3D) model with a regular mesh and a Poisson Voronoi tessellation. Compared to the axisymmetric model with a small number of iron and copper grains and homogeneous boundary conditions, the 3D model with more grains (500-1500) and periodic boundary conditions should give even better results than the axisymmetric model. Simulations are performed for pure iron, pure copper, and five of their composites to study the texture evolution according to the phase volume change which is not predicted in detail by the axisymmetric simulation. Based on simulated results, a quantitative conclusion is drawn for the stress distribution in each phase. The local strain distribution predicted by the finite element model is compared with that of the reality.

Notation

a, b, c, ...	reals
$\boldsymbol{a}, \boldsymbol{b}, \boldsymbol{c}$, ...	vectors
$\boldsymbol{A}, \boldsymbol{B}, \boldsymbol{C}$, ...	2nd-order tensors
$\mathbb{A}, \mathbb{B}, \mathbb{C}$, ...	4th-order tensors
$\{\boldsymbol{e}_i\}$	orthonormal basis
a_i, A_{ij}, A_{ijkl}	components of $\boldsymbol{a}, \boldsymbol{A}$ and $\mathbb{A}$ with respect to $\{\boldsymbol{e}_i\}$
$\boldsymbol{C} = \boldsymbol{a} \otimes \boldsymbol{b}, \mathbb{C} = \boldsymbol{A} \otimes \boldsymbol{B}$	dyadic product between vectors and 2nd-order tensors
$c = \boldsymbol{a} \cdot \boldsymbol{b}, c = a_i b_i$	scalar product of vectors
$c = \boldsymbol{A} \cdot \boldsymbol{B}, c = A_{ij} B_{ij}$	scalar product of 2nd-order tensors
$\boldsymbol{c} = \boldsymbol{A}\boldsymbol{b}, c_i = A_{ij} b_j$	2nd-order tensor and a vector product result in a vector
$\boldsymbol{C} = \boldsymbol{A}\boldsymbol{B}, C_{ik} = A_{ij} B_{jk}$	composition of two 2nd-order tensor

$\boldsymbol{C} = \mathbb{A}[\boldsymbol{B}], C_{ij} = A_{ijkl}B_{kl}$	4th- and 2nd-order tensor product result in 2nd-order tensor
$\boldsymbol{A} \star \mathbb{B} = B_{ijkl}(\boldsymbol{A}\boldsymbol{e}_i) \otimes (\boldsymbol{A}\boldsymbol{e}_j) \otimes (\boldsymbol{A}\boldsymbol{e}_k) \otimes (\boldsymbol{A}\boldsymbol{e}_l)$	Rayleigh product
$\boldsymbol{A}'$	deviatoric part of tensor $\boldsymbol{A}$
$\boldsymbol{A}^\circ$	spherical part of tensor $\boldsymbol{A}$
$\mathrm{grad}\,(\boldsymbol{A})$	gradient of $\boldsymbol{A}$ with respect to the current placement
$\mathrm{Grad}\,(\boldsymbol{A})$	gradient of $\boldsymbol{A}$ with respect to the reference placement
$\mathrm{Sym}(\boldsymbol{A})$	symmetric part of $\boldsymbol{A}$
$\mathrm{Skw}(\boldsymbol{A})$	skew part of $\boldsymbol{A}$
$\mathrm{tr}(\boldsymbol{A})$	trace of $\boldsymbol{A}$
$\det(\boldsymbol{A})$	determinant of $\boldsymbol{A}$
$\exp(\boldsymbol{A})$	exponential function of $\boldsymbol{A}$
$\|\boldsymbol{A}\| = \sqrt{\boldsymbol{A} \cdot \boldsymbol{A}}$	Frobenius norm of $\boldsymbol{A}$
$\tilde{(\cdot)}$	quantity with respect to the undistorted placement
$(\cdot)_t$	quantity with respect to the current placement
$\bar{(\cdot)}$	homogenised quantity
$(\cdot)^{\cdot}$	material time derivative
$\mathcal{B}$	material body
$\mathcal{R}$	set of real numbers
$\mathcal{R}^+$	set of positive real numbers
$\mathfrak{E}$	Euclidean space
Sym^+	set of symmetric and positive definite 2nd-order tensors
Inv^+	set of invertible 2nd-order tensors with positive definite
$SO(3)$	set of orthogonal 2nd-order tensors with positive determinants

Frequently used symbols

Symbol	Name	occurrence
J	determinant of the deformation gradient	(3.54)
K	bulk modulus	(3.54)
m	strain rate sensitivity parameter	(3.40)
n	stress exponent	(3.52)
v	volume in the current placement	(4.4)
V	volume in the reference placement	(4.1)
λ	eigenvalue of the elasticity tensor	(3.29)
γ_α	shear rate in slip system α	(3.39)
γ_0	reference shear rate	(3.39)
κ	Boltzmann constant	(3.39)
τ_α	resolved shear stress	(3.39)
τ_α^C	critical resolved shear stress	(3.40)
μ	shear modulus	section 3.2.4
ρ	dislocation density	(3.47)
$\tilde{\boldsymbol{d}}_\alpha$	slip direction α	section 3.2.2
$\{\boldsymbol{g}_i\}$	orthonormal basis of crystal lattice	section 3.2.1
$\tilde{\boldsymbol{n}}_\alpha$	normal of slip plane α	section 3.2.2
$\boldsymbol{u}$	displacement vector	(3.4)
$\boldsymbol{B}$	left Cauchy-Green tensor	(3.7)
$\boldsymbol{C}$	right Cauchy-Green tensor	(3.7)
$\boldsymbol{D}$	symmetric part of velocity gradient tensor	(3.14)
$\boldsymbol{E}^A$	Almansi's strain tensor	(3.8)
$\boldsymbol{E}^G$	Green's strain tensor	(3.8)
$\boldsymbol{E}^H$	Hencky strain tensor in the reference placement	(3.10)
$\boldsymbol{E}^h$	Hencky strain tensor in the current placement	(3.10)
$\boldsymbol{F}$	deformation gradient	(3.5)
$\tilde{\boldsymbol{F}}$	elastic part of the deformation gradient	(3.32)
$\boldsymbol{F}_p$	plastic part of the deformation gradient	(3.33)

Symbol	Name	occurrence
$\boldsymbol{H}$	displacement gradient	(3.11)
$\boldsymbol{I}$	2nd-order identity tensor	(3.8)
$\boldsymbol{L}$	velocity gradient	(3.13)
$\boldsymbol{M}_\alpha$	Schmid tensor	(3.42)
$\boldsymbol{P}$	plastic transformation tensor	(3.23)
$\boldsymbol{Q}$	crystal orientation	(3.56)
$\boldsymbol{R}$	proper orthogonal part of the deformation gradient	(3.6)
$\boldsymbol{\sigma}$	Cauchy stress tensor	(3.19)
$\boldsymbol{T}^{1PK}$	1st Piola-Kirchhoff stress tensor	(4.2)
$\boldsymbol{T}^{2PK}$	2nd Piola-Kirchhoff stress tensor	(3.18)
$\boldsymbol{T}^{K}$	Kirchhoff stress tensor	(3.19)
$\boldsymbol{T}$	Mandel stress tensor	(3.43)
$\boldsymbol{U}$	right stretch tensor of the deformation gradient	(3.6)
$\boldsymbol{V}$	left stretch tensor of the deformation gradient	(3.6)
$\boldsymbol{W}$	skew part of the velocity gradient tensor	(3.14)
$\mathbb{C}$	elasticity tensor	(3.18)
$\mathbb{I}$	4th-order identity tensor	(3.29)
$\mathbb{P}$	cubic projector	(3.30)
$\boldsymbol{J}$	Jacobian matrix in Newton method	(A.5)
2D	two-dimensional	chapter 1
3D	three-dimensional	chapter 1
bcc	body-centered-cubic	chapter 1
fcc	face-centered-cubic	chapter 1
FE	finite element	chapter 1
FEM	finite element method	section 4.3
hcp	hexagonal close-packed lattice	section 3.2.2
HBC	homogeneous boundary conditions	chapter 4
MMC	metal matrix composite	section 5.1.2
ODF	orientation distribution function	section 2.2.1
OOF	Object-Oriented Finite Element Analysis of Real Material Microstructures Working Group	section 6.2

Symbol	Name	occurrence
PBC	periodic boundary conditions	chapter 4
PISM	principle of invariance under superimposed rigid body motions	section 3.2.1
PMO	principle of material objectivity	section 3.2.1
ROM	rule of mixture	section 5.1.2
RVE	representative volume element	chapter 4

Chapter 2

Iron-Copper Polycrystals: Experiments

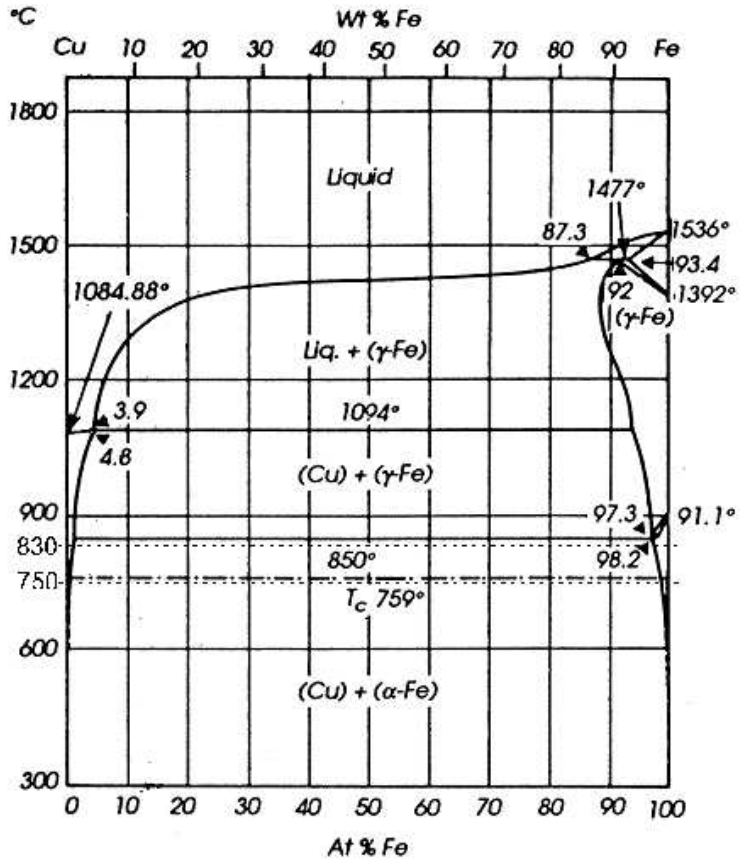

Figure 2.1: Phase solubility diagram of copper and iron systems (Kubaschewski, 1982).

The inelastic deformation of ductile two-phase polycrystalline composites is studied in order to obtain the influence of the micromechanical interaction of phases

on the macroscopic material behaviour. Both phases in such composites are ductile and have significantly different strength. There is no a priori crystallographic orientation-dependence between these two phases. The deformation behaviour of the single phase is relatively well known. The composite hardens with increasing deformation and has a different crystal structure for each phase. The mutual solubility of both phases is negligible.

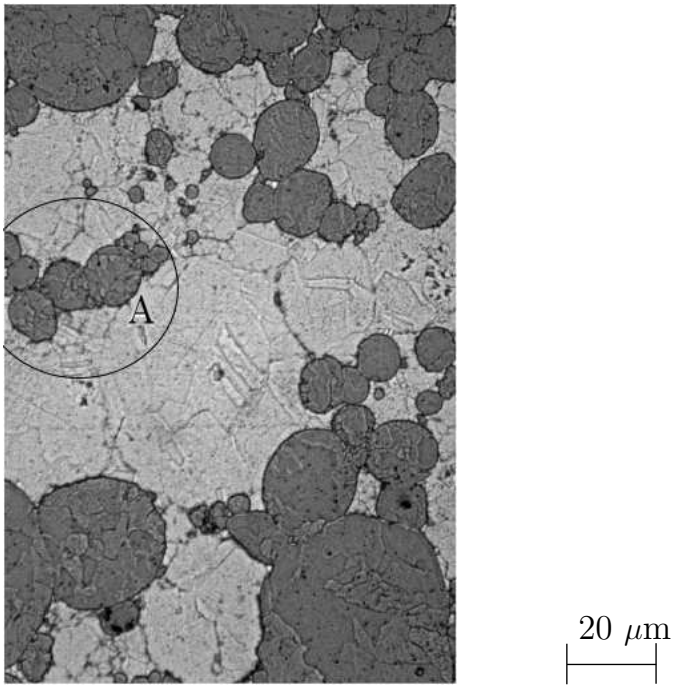

Figure 2.2: Microstructure of Fe50-Cu50 composite with polycrystalline particles where an iron particle (darker phase) is composed of several grains in the circle A. (Commentz, 2000)

Considering the above-mentioned criteria, iron-copper polycrystalline composites are chosen in the present work. The phase diagram of iron and copper (Figure 2.1) shows the solubility of the iron in the copper and vice versa at the maximum 830 °C (Kubaschewski, 1982).

2.1 Production of Iron-Copper Polycrystals

2.1.1 Iron and Copper Powders

The iron-copper polycrystals[1] were produced from mixtures of iron and copper powder by powder metallurgy. All powders have a purity higher than 99% and the major impurity is the oxide on the surface of the copper powders. Both the iron and the copper powders consist of spherical polycrystalline particles with a diameter less than 63 μm. Such particles, normally, are composed of several grains, e.g., the darker phase in circle A in Figure 2.2 (some particles may have just one grain). The mean value of the particle size is 20.5 μm for the iron phase and 18.3 μm for the copper phase. The carbon content of the iron powder is 0.015 wt%.

2.1.2 Production Process

The production of iron-copper composites follows three steps: the mixing, the precompression, and the final compression. The mixtures are identified by the volume fraction (vol.%) of the iron and the copper phase. Here we consider seven such mixtures, namely Fe100, Fe83-Cu17, Fe67-Cu33, Fe50-Cu50, Fe33-Cu67, Fe17-Cu83 and Cu100. The microstructures (Figure 2.3) of these two-phase composites can be sorted as the inclusion/matrix type (e.g., Fe17-Cu83) and an interpenetrating network of these two phases (Fe50-Cu50).

The iron and the copper powders are mixed in a whirling blender. The mixing time is one hour, which is optimal for a good mixture and for avoiding powder agglomerates. After the mixing of the powders, the precompression, which lasts two hours, is performed cold isostatically in a cylindrical and elastic rubber capsule at a pressure between 130-230 MPa. Through this process, the mixture (compact) has a density about 80% of the theoretical one. The porous compact receives its final density by hot-processing in a cylindrical die. This process with a pressure of 190 MPa is performed at 800 °C in the vacuum. In order to obtain a density of the mixture higher than 99% of the theoretical one, this process lasts between 0.5

[1]Such polycrystal samples and the corresponding experiments are produced and performed in the Technische Universität Hamburg-Harburg. Concerning the details of the composite production and the experimental processing of the tests, we refer to Commentz *et al.* (1999); Commentz (2000); Hartig and Mecking (2005).

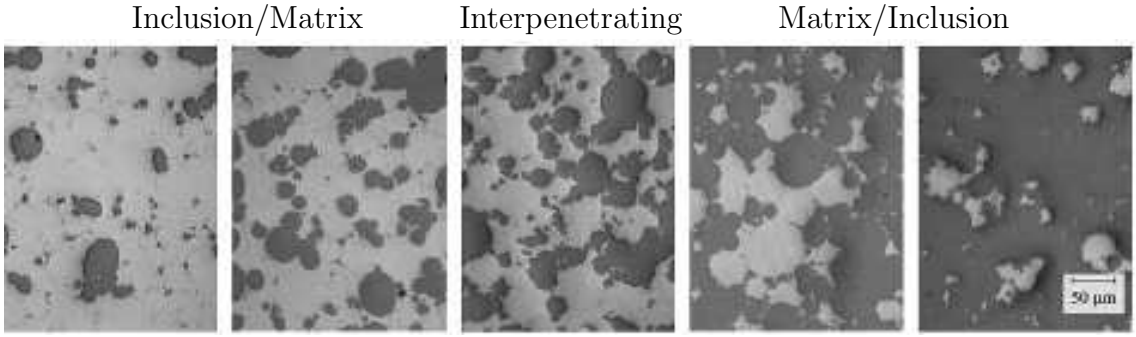

Figure 2.3: Microstructures of iron-copper polycrystals (compositions in vol.%) (Hartig and Mecking, 2005).

to 6 hour(s). The final iron-copper sample has dimensions of height × diameter = 17 × 25 (mm^2) and is used for the compression test. Samples are named after their composition.

2.2 Experiments

2.2.1 Mechanical Testing and Texture Measurement

A schematic overview of the extractions of samples is shown in Figure 2.4 for the compression test, where ND, TD and RD means the normal direction, the transverse direction, and the rolling direction, respectively. Firstly, the plates with quadratic surfaces are cut out from the cylindrical sample. Secondly, the surfaces of the plate are ground until the dimensions of the plate are 17×17×5 mm^3. Thirdly, the cylindrical sample (height=9 mm and diameter=6 mm) for the compression test is obtained from the ground plate, where the normal direction of this cut-out specimen corresponds to the rolling direction of the plate. After the compression test (90% logarithmic plastic strain), the sample (a in Figure 2.4) is ground and polished until its middle plane which is parallel to the top/bottom surface is laid open (b in Figure 2.4). The texture measurement is accomplished on this middle surface, i.e., the top surface in b of Figure 2.4.

The compression tests on the cylindrical samples are performed at room temperature (20 °C) with a constant strain rate $\dot{\varepsilon} = 10^{-4}$ s^{-1} in order to determine the stress-strain behaviour. Aimed to reduce the friction between the top/bottom surface of the sample and front surfaces of the punching tool, a lubricant (BN-spray)

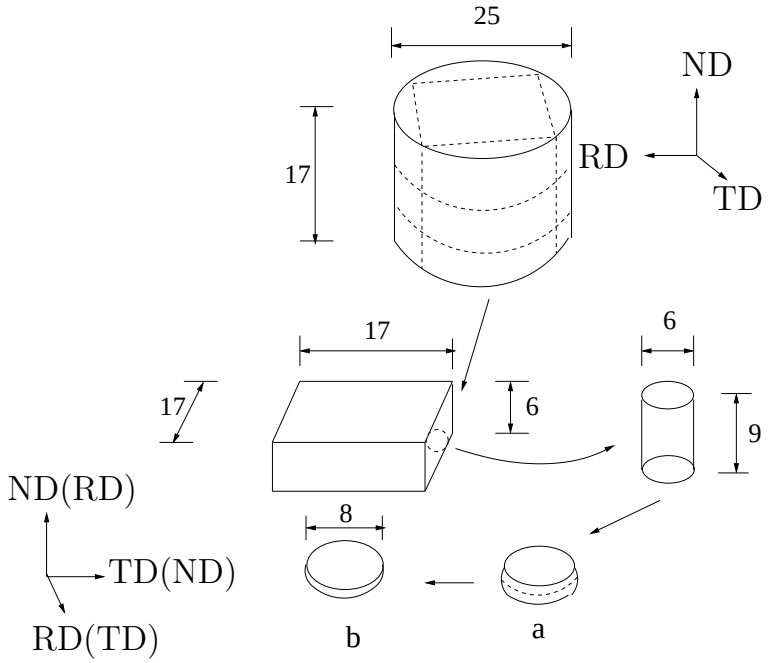

Figure 2.4: Sample after production processes and extracted sample for the compression test ("a": sample after compression; "b": sample ground from "a" for texture measurement) (Commentz, 2000).

is used. A correction for the stress calculation is also performed to compensate for the dynamical and the static friction between the sample and the punching tool. The coefficient of the friction is taken as $\mu = 0.235$.

Concerning the textures from experimental measurements, pole figures are firstly determined by the experiment. Subsequently, the orientation distribution function (ODF) is calculated from the above pole figures. A detailed overlook about the terminologies applied for the texture is given by Kocks *et al.* (1998).

At room temperature, all measurements are determined by a computer controlled four-circle goniometer by an X-ray (CoK_α ray) diffraction procedure. Pole figures are measured for three reflections, namely {200}, {211}, and {220} for the iron phase and {200}, {220}, and {311} for the copper phase, by scanning the hexagonal grid (Matthies and Wenk, 1992). The measured data are further processed in a 5×5 grid. The statistics of the measurement are improved by the translational movement of the sample in the rolling direction with an amplitude between 0.5 and 2 mm.

After the normalization and the correction of the coarse data from three reflections of each phase, the data are used as the input for the calculation of the ODF $f(\boldsymbol{Q})$

which quantitatively describes the density distribution of the orientation $\boldsymbol{Q}$ of all the crystal coordinates with respect to the sample coordinate. The $\boldsymbol{Q}$ in $f(\boldsymbol{Q})$ is presented by three Euler angles ϕ_1, Φ, and ϕ_2 following Bunge (1993). The ODF is separately calculated from the pole figures for each phase by using the WIMV-algorithm (Kallend *et al.*, 1991) in the popLA texture package (Popla, 8918). The iteration is performed 6 to 20 times until the error between the measured pole figure and the one back-calculated by the ODF is smaller than 1.5%. The final texture for the simple compression test is presented as the standard inverse pole figure. The typical fibre texture, <100>- and <111>-fibre, is shown for the α-iron. The copper phase is characterised by the <110>-fibre which develops in the <210> direction. Besides, a very weak <411>-fibre texture appears for the compressively deformed copper (see Figure B.2 for fibre directions).

2.2.2 Strain Distribution

The strain field[1] is performed on a tension sample from the Fe17-Cu83 composite[2]. The geometry of the sample for the tension test is presented in Figure 2.5. The measured cut-out is extracted from the middle plane (through the tension direction LD and the transverse direction TD in Figure 2.5b) of the unloaded sample and has a rectangular geometry with the dimensions of 640×480 μm^2 and 160×120 μm^2 for the undeformed case and at a large deformation, respectively. The grid of sampling points is 3×3. A monochrome photo is taken in BSE-contrast (back scattering electron) in order to make both phases in the cut-out visible. Additionally, photos are taken from the same sample region in the unloaded state and each further deformed step by SE-contrast-conditions (secondary electron).

The change of the displacement in the chosen cut-out is achieved by comparing the (digital) photos before and after a given load step. The rigid body translation and the rotation are subtracted from the measured displacement vector (WMA,

[1]The measurement and the calculation of the local strain field has been performed by V. Heitmann and Dr. A. Cornec (Institut für Werkstoffforschung, GKSS Forschungszentrum, Geesthacht.)

[2]Concerning the production of this Fe17-Cu83 composite, there is some difference from that described in section 2.1, where the size of Cu powder is less than7 80 μm (63 μm in section 2.1) and the hot isostatic pressure is applied to obtain the final density of the composite (hot pressure in section 2.1).

Institut für Werkstofforschung, GKSS Forschungszentrum, Geesthacht, Germany). Therefore, only the local displacement remains.

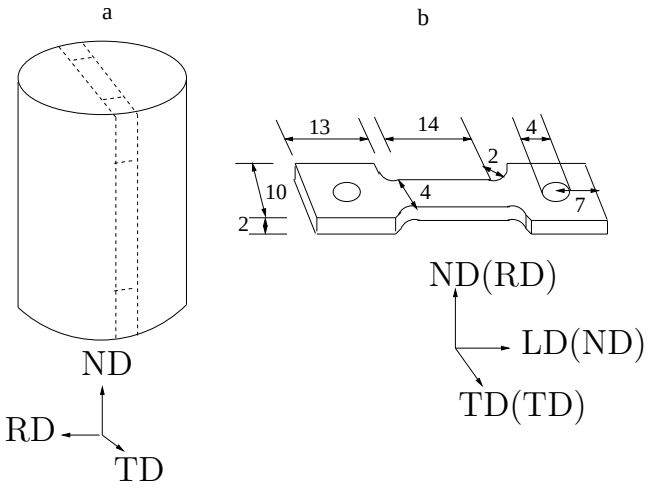

Figure 2.5: Extracted sample used for the measurement of the distribution of the local strain field in a tension test (the loading direction LD in b is also the tension direction) (Commentz, 2000).

Since the determination of the strain as the local derivative of the displacement field is sensitive to the unevenness in the displacement field, the numerically obtained displacement field is smoothed by another computer code (Software Surfer, GOLDEN SOFTWARE INC., Golden, Colorado, U.S.A.). During this process, only the small peaks are smoothed from the irregular surface of the displacement field by considering the environment so that the local gradient is not significantly changed. The effect of the smoothing is proved and optimised by directly comparing the output data.

The strain field is calculated componentwise by a computer code (WMA, Intstitut für Werkstoffforschung, GKSS Forschungszentrum, Geesthacht, Germany). The strain presented in this work is referred to the undeformed position.

Chapter 3

Continuum Mechanics

3.1 Kinematics

The object of mechanics is to investigate the motion of material bodies under the influence of forces. In continuum mechanics, such bodies are at least piecewise continuously differentiable with respect to the coordinates at each position, i.e., a differentiable manifold (Haupt, 2000). Kinematics is the subject of describing the aforementioned movements under their temporal and spatial aspects. In the present work classical mechanics are used to describe the placement of the material body. This means that such placement of material bodies are domains of the three-dimensional Euclidean space.

A material body $\mathcal{B}$ is assumed to be composed of material points X which are also called particles or material elements. A placement[1] of the body $\mathcal{B}$ is a mapping $\boldsymbol{\chi} : \mathcal{B} \rightarrow \mathfrak{E}$ in the Euclidean space. The position of a material point is given through the mapping

$$\boldsymbol{x} = \boldsymbol{\chi}(X). \tag{3.1}$$

A motion of the body can be considered as a time-dependent sequence of placements. It is advantageous to introduce a reference placement $\mathcal{B}_0$. We denote the positions of material points in the reference placement by vectors $\boldsymbol{X}$ at the time $t = 0$, i.e.,

[1] Some literature uses "configuration" instead of "placement", e.g., Haupt (2000); Lubarda (2002).

$$\boldsymbol{X} = \boldsymbol{\chi}(X, t = 0). \tag{3.2}$$

Positions of material points in the current placement $\mathcal{B}_t$ are given as $\boldsymbol{x}$ at time $t \in \mathcal{R}^+$. Through the inversion of equation (3.2), $\boldsymbol{x}$ can be written as

$$\boldsymbol{x} = \boldsymbol{\chi}(\boldsymbol{\chi}^{-1}(\boldsymbol{X}, t = 0), t). \tag{3.3}$$

In the following, we specify $\boldsymbol{X}$ and $\boldsymbol{x}$ with respect to an orthonormal basis $\{\boldsymbol{e}_i\}$ with the point of the origin O (see Figure 3.1).

The displacement vector $\boldsymbol{u}$ is the difference of the position vector of a material point in the current and in the reference placement

$$\boldsymbol{u}(\boldsymbol{X}, t) := \boldsymbol{\chi}(\boldsymbol{X}, t) - \boldsymbol{X}, \tag{3.4}$$

which is shown in Figure 3.1.

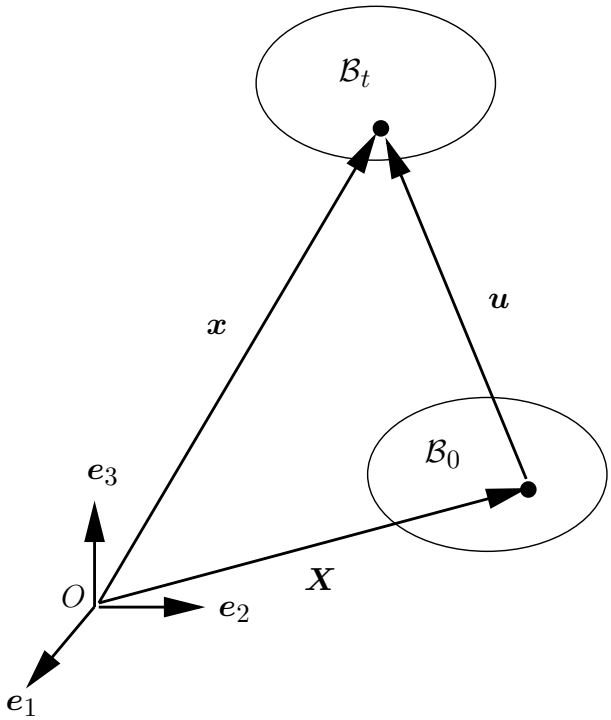

Figure 3.1: Sketch of the reference placement, the current placement, and the displacement of a material point in the Euclidean space with respect to the orthonormal basis $\{\boldsymbol{e}_i\}$.

The deformation gradient $\boldsymbol{F}$ is defined as

$$\boldsymbol{F} := \mathrm{Grad}\,(\boldsymbol{\chi}(\boldsymbol{X}, t)) = \frac{\partial \boldsymbol{\chi}(\boldsymbol{X}, t)}{\partial \boldsymbol{X}}, \tag{3.5}$$

which is usually used to describe the deformation behaviour of materials. The 2nd-order tensor $\boldsymbol{F}$ is dimensionless and invertible for every point at each time. It connects the reference and the current placement and is called a two-point tensor. The deformation gradient can be polarly decomposed as

$$\boldsymbol{F} = \boldsymbol{R}\,\boldsymbol{U} = \boldsymbol{V}\,\boldsymbol{R}. \tag{3.6}$$

$\boldsymbol{R}$ is a proper orthogonal tensor, $\boldsymbol{U}$ and $\boldsymbol{V}$ are the right and the left stretch tensors, which are symmetric and positive definite, i.e., $\boldsymbol{U}$, $\boldsymbol{V} \in Sym^{+}$.

The right Cauchy-Green tensor $\boldsymbol{C}$ and the left Cauchy-Green tensor $\boldsymbol{B}$ are defined as

$$\begin{aligned} \boldsymbol{C} &:= \boldsymbol{U}^2 = \boldsymbol{F}^{\mathsf{T}}\boldsymbol{F}, \\ \boldsymbol{B} &:= \boldsymbol{V}^2 = \boldsymbol{F}\boldsymbol{F}^{\mathsf{T}}. \end{aligned} \tag{3.7}$$

The Green's strain $\boldsymbol{E}^G$ and the Almansi's strain $\boldsymbol{E}^A$ are defined as

$$\begin{aligned} \boldsymbol{E}^G &= \frac{1}{2}(\boldsymbol{C} - \boldsymbol{I}), \\ \boldsymbol{E}^A &= \frac{1}{2}(\boldsymbol{I} - \boldsymbol{B}^{-1}), \end{aligned} \tag{3.8}$$

where $\boldsymbol{I}$ indicates the 2nd-order identity tensor. These two strain tensors can be transformed into each other by using $\boldsymbol{F}$,

$$\boldsymbol{E}^G = \boldsymbol{F}^{\mathsf{T}}\boldsymbol{E}^A\boldsymbol{F}. \tag{3.9}$$

If a quantity is transformed from the current placement into the reference placement, it is named as pull back. In equation (3.9), $\boldsymbol{E}^A$ is pulled back from the current placement to the reference placement. When the transformation is performed in the other direction, it is called push forward. The Hencky (logarithmic) strain tensor in the reference and the current placement are given as

$$\begin{aligned} \boldsymbol{E}^H &:= \ln \boldsymbol{U} = \frac{1}{2} \ln \boldsymbol{C}, \\ \boldsymbol{E}^h &:= \ln \boldsymbol{V} = \frac{1}{2} \ln \boldsymbol{B}, \end{aligned} \tag{3.10}$$

respectively.

The deformation behaviour of materials can also be described in terms of the displacement gradient $\boldsymbol{H}$ defined by

$$\boldsymbol{H} := \mathrm{Grad}\,(\boldsymbol{u}(\boldsymbol{X}, t)) = \frac{\partial \boldsymbol{\chi}}{\partial \boldsymbol{X}} - \frac{\partial \boldsymbol{X}}{\partial \boldsymbol{X}} = \boldsymbol{F} - \boldsymbol{I}. \tag{3.11}$$

All the above strain tensors can be expressed by $\boldsymbol{H}$ instead of $\boldsymbol{F}$, e.g.,

$$\boldsymbol{E}^G = \frac{1}{2}(\boldsymbol{H} + \boldsymbol{H}^\mathsf{T} + \boldsymbol{H}^\mathsf{T}\boldsymbol{H}). \tag{3.12}$$

The term $\boldsymbol{H}^\mathsf{T}\boldsymbol{H}$ in equation (3.12) shows that the strain tensor $\boldsymbol{E}^G$ is non-linear in $\boldsymbol{H}$ and thus non-linear in the displacement field $\boldsymbol{u}$.

The spatial velocity gradient $\boldsymbol{L}$ is defined as

$$\boldsymbol{L} := \frac{\partial \boldsymbol{v}}{\partial \boldsymbol{x}} = \dot{\boldsymbol{F}}\boldsymbol{F}^{-1} \tag{3.13}$$

with the velocity field $\boldsymbol{v}$. It is useful for the analysis of motions to decompose additively the tensor $\boldsymbol{L}$ as

$$\boldsymbol{L} = \boldsymbol{D} + \boldsymbol{W}, \tag{3.14}$$

where

$$\boldsymbol{D} = \frac{1}{2}(\boldsymbol{L} + \boldsymbol{L}^\mathsf{T}), \qquad \boldsymbol{W} = \frac{1}{2}(\boldsymbol{L} - \boldsymbol{L}^\mathsf{T}). \tag{3.15}$$

$\boldsymbol{D}$ is the symmetric part of $\boldsymbol{L}$ and is the rate of deformation tensor, and $\boldsymbol{W}$ is the skew spin tensor. $\boldsymbol{D}$ can be additively decomposed into the deviatoric part $\boldsymbol{D}'$ and the spheric (volumetric) part $\boldsymbol{D}^\circ$ with

$$\boldsymbol{D} = \boldsymbol{D}' + \boldsymbol{D}^{\circ} = \boldsymbol{D}' + \frac{1}{3}\mathrm{tr}(\boldsymbol{D})\boldsymbol{I}. \tag{3.16}$$

The deformation gradient $\boldsymbol{F}$ and the velocity gradient $\boldsymbol{L}$ are essential for the analysis of the motion of the deformable bodies. Since $\boldsymbol{F}$ describes the changes of the material elements (line, surface and volume elements) and $\boldsymbol{L}$ presents the rate at which these changes take place.

3.2 Elasto-viscoplasticity

For elastic materials, the current stress is determined by the current strain. In hyperelasticity, the elastic strain energy serves as a potential for the stresses. The rate-independence is assumed for the elasto-plasticity. A more realistic description of the material behaviour requires that the model is rate-dependent. A viscoplastic formulation is one of such possibilities to include the rate-dependence.

3.2.1 Elastic Law

In order to formulate an elastic law, we assume that the 2nd Piola-Kirchhoff stress tensor $\boldsymbol{T}^{2PK}$ is a function of the right Cauchy-Green tensor $\boldsymbol{C}$

$$\boldsymbol{T}^{2PK} = \boldsymbol{h}(\boldsymbol{C}). \tag{3.17}$$

The above reduced form fulfills the principle of the material objectivity (PMO) and the principle of invariance under superimposed rigid body motions (Bertram, 2005). Since metals possess a small elastic range, it is possible to find a physical linear relation between $\boldsymbol{T}^{2PK}$ and $\boldsymbol{C}$

$$\boldsymbol{T}^{2PK} = \mathbb{C}\left[\frac{1}{2}(\boldsymbol{C} - \boldsymbol{I})\right] = \mathbb{C}[\boldsymbol{E}^{G}]. \tag{3.18}$$

In equation (3.18), $\mathbb{C}$ is the 4th-order symmetric elasticity tensor. The Kirchhoff stress $\boldsymbol{T}^{K}$ is defined by the Cauchy stress $\boldsymbol{\sigma}$

$$\boldsymbol{T}^{K} = \det(\boldsymbol{F})\boldsymbol{\sigma}. \tag{3.19}$$

The relation between the Kirchhoff stress tensor $\boldsymbol{T}^K$ and $\boldsymbol{T}^{2PK}$ is

$$\boldsymbol{T}^{2PK} = \boldsymbol{F}^{-1}\boldsymbol{T}^K\boldsymbol{F}^{-\mathsf{T}}. \tag{3.20}$$

Voigt (1910) classified crystals into 32 classes based on the number of the rotations or reflections of the symmetry. Physically possible 2- and 3-dimensional symmetry groups are reported by Zheng and Boehler (1994). Forte and Vianello (1996) and Ting (1996) have shown that only 8 different symmetry classes can be distinguished in the context of the 4th-order linear operators. For simplicity, we present the tensor $\mathbb{C}$ by six by six matrices, and the components $C_{\alpha\beta}$ refer to the orthonormal basis $\boldsymbol{B}_\alpha$ of the symmetric 2nd-order tensors, namely, $C_{\alpha\beta} = \boldsymbol{B}_\alpha \cdot \mathbb{C}[\boldsymbol{B}_\beta]$, with

$$\begin{aligned}
\boldsymbol{B}_1 &= \boldsymbol{e}_1 \otimes \boldsymbol{e}_1, \\
\boldsymbol{B}_2 &= \boldsymbol{e}_2 \otimes \boldsymbol{e}_2, \\
\boldsymbol{B}_3 &= \boldsymbol{e}_3 \otimes \boldsymbol{e}_3, \\
\boldsymbol{B}_4 &= \frac{\sqrt{2}}{2}(\boldsymbol{e}_2 \otimes \boldsymbol{e}_3 + \boldsymbol{e}_3 \otimes \boldsymbol{e}_2), \\
\boldsymbol{B}_5 &= \frac{\sqrt{2}}{2}(\boldsymbol{e}_1 \otimes \boldsymbol{e}_3 + \boldsymbol{e}_3 \otimes \boldsymbol{e}_1), \\
\boldsymbol{B}_6 &= \frac{\sqrt{2}}{2}(\boldsymbol{e}_1 \otimes \boldsymbol{e}_2 + \boldsymbol{e}_2 \otimes \boldsymbol{e}_1).
\end{aligned} \tag{3.21}$$

The above presentation of $\mathbb{C}$ is the modified Voigt notation (see, e.g., Cowin (1989)). In the case of cubic symmetry, there are three independent components C_{1111}, C_{1122} and C_{2323} in $\mathbb{C}$

$$\mathbb{C} = \begin{bmatrix} C_{1111} & C_{1122} & C_{1122} & 0 & 0 & 0 \\ C_{1122} & C_{1111} & C_{1122} & 0 & 0 & 0 \\ C_{1122} & C_{1122} & C_{1111} & 0 & 0 & 0 \\ 0 & 0 & 0 & 2C_{2323} & 0 & 0 \\ 0 & 0 & 0 & 0 & 2C_{2323} & 0 \\ 0 & 0 & 0 & 0 & 0 & 2C_{2323} \end{bmatrix} \boldsymbol{B}_\alpha \otimes \boldsymbol{B}_\beta. \tag{3.22}$$

Following the theory of materials with isomorphic elastic ranges (Bertram, 1992, 1999), we introduce the plastic transformation $\boldsymbol{P} \in Inv^+$. An elastic reference law can be found, which is constant and given as

$$\boldsymbol{T}^{2PK} = \boldsymbol{P}\ \tilde{\boldsymbol{h}}(\boldsymbol{P}^\mathsf{T}\boldsymbol{C}\boldsymbol{P})\boldsymbol{P}^\mathsf{T} \tag{3.23}$$

instead of the elastic law in equation (3.17). The right hand side of equation (3.23) does not change as a function, but only through the time-dependent variables of $\boldsymbol{P}$ and $\boldsymbol{C}$. Since the elastic range is always small for metals, a physically linear relation

$$\boldsymbol{T}^{2PK} = \frac{1}{\det(\boldsymbol{P})}\boldsymbol{P}\ \tilde{\mathbb{C}}\left[\frac{1}{2}(\boldsymbol{P}^\mathsf{T}\boldsymbol{C}\boldsymbol{P} - \boldsymbol{I})\right]\boldsymbol{P}^\mathsf{T} \tag{3.24}$$

is available based on the isomorphy condition. The elasticity tensor $\tilde{\mathbb{C}}$ describes a constant stiffness tetrade during the deformation process. The tilde for $\tilde{\mathbb{C}}$ means that $\tilde{\mathbb{C}}$ is formulated with respect to the undistorted state $\tilde{\mathcal{B}}$. This state is characterised by the fact that the corresponding symmetry transformations are elements of $SO(3)$ (Truesdell and Noll, 1965). In the following, this concept is also applied to other quantities. A detailed description of the isomorphic elasticity can be referenced to Truesdell and Noll (1965); Bertram (2005). Numerical applications of this model are given in Bertram and Kraska (1995a,b); Bertram *et al.* (1997); Böhlke *et al.* (1997).

Let $\boldsymbol{g}_i$ be the basis vectors of the crystal lattice in the reference placement $\mathcal{B}_0$ and $\boldsymbol{g}_i^E$ be those in the current placement $\mathcal{B}_t$. Under the help of the plastic transformation $\boldsymbol{P}$ and the deformation gradient $\boldsymbol{F}$, $\boldsymbol{g}_i$ and $\boldsymbol{g}_i^E$ can be determined by the basis vectors $\tilde{\boldsymbol{g}}_i$ in the undistorted placement, i.e.,

$$\boldsymbol{g}_i = \boldsymbol{P}\tilde{\boldsymbol{g}}_i \tag{3.25}$$

and

$$\boldsymbol{g}_i^E = \boldsymbol{F}\boldsymbol{P}\tilde{\boldsymbol{g}}_i, \tag{3.26}$$

respectively. Basis vectors of the elasticity tensors $\mathbb{C}$ and $\mathbb{C}^E$ are specified by $\boldsymbol{g}_i$ and $\boldsymbol{g}_i^E$. The material and the spatial elasticity tensors are given as

$$\mathbb{C} = \boldsymbol{P} \star \tilde{\mathbb{C}} = \tilde{C}_{ijkl}(\boldsymbol{P}\tilde{\boldsymbol{g}}_i) \otimes (\boldsymbol{P}\tilde{\boldsymbol{g}}_j) \otimes (\boldsymbol{P}\tilde{\boldsymbol{g}}_k) \otimes (\boldsymbol{P}\tilde{\boldsymbol{g}}_l) \tag{3.27}$$

and

$$\mathbb{C}_E = \boldsymbol{F}\boldsymbol{P} \star \tilde{\mathbb{C}} = \tilde{C}_{ijkl}(\boldsymbol{F}\boldsymbol{P}\tilde{\boldsymbol{g}}_i) \otimes (\boldsymbol{F}\boldsymbol{P}\tilde{\boldsymbol{g}}_j) \otimes (\boldsymbol{F}\boldsymbol{P}\tilde{\boldsymbol{g}}_k) \otimes (\boldsymbol{F}\boldsymbol{P}\tilde{\boldsymbol{g}}_l), \tag{3.28}$$

respectively. In equations (3.27) and (3.28), the components of the elasticity tensor $\mathbb{C}$ are not constant in the reference placement. The operator $\star$ indicates the Rayleigh product, and $\tilde{\mathbb{C}}$ is a constant tensor. The elasticity tensor $\tilde{\mathbb{C}}$ can also be presented by projection operators (Rychlewski and Zhang, 1989; Bertram and Olschewski, 1991) and, in the case of the cubic symmetry, has the form of

$$\tilde{\mathbb{C}} = \sum_{i=1}^{3} \lambda_i \mathbb{P}_i^C. \tag{3.29}$$

λ_i denote the distinct eigenvalues of $\tilde{\mathbb{C}}$ and can be written in terms of the components of $\tilde{\mathbb{C}}$ with respect to the orthonormal lattice vectors $\{\tilde{\boldsymbol{g}}_i\}$, i.e., $\lambda_1 = \tilde{C}_{1111} + 2\tilde{C}_{1122}$, $\lambda_2 = \tilde{C}_{1111} - \tilde{C}_{1122}$ and $\lambda_3 = 2\tilde{C}_{1212}$. The three projectors $\mathbb{P}_i^C$ are

$$\mathbb{P}_1^C = \frac{1}{3}\boldsymbol{I} \otimes \boldsymbol{I}, \qquad \mathbb{P}_2^C = \mathbb{D} - \mathbb{P}_1^C, \qquad \mathbb{P}_3^C = \mathbb{I}^S - \mathbb{P}_2^C - \mathbb{P}_1^C \tag{3.30}$$

$$\mathbb{D} = \sum_{i=1}^{3} \tilde{\boldsymbol{g}}_i \otimes \tilde{\boldsymbol{g}}_i \otimes \tilde{\boldsymbol{g}}_i \otimes \tilde{\boldsymbol{g}}_i. \tag{3.31}$$

with $\mathbb{I}^S$ being the 4th-order identity tensor for symmetric 2nd-order tensors. The anisotropic part $\mathbb{D}$ is determined by the lattice vectors $\tilde{\boldsymbol{g}}_i$. These three projectors satisfy the following conditions: idempotent $\mathbb{P}_i^C \mathbb{P}_i^C = \mathbb{P}_i^C$, biorthogonal $\mathbb{P}_i^C \mathbb{P}_j^C = \mathbb{O}$ with $i \neq j$, and the complete $\sum_{i=1}^{3} \mathbb{P}_i^C = \mathbb{I}$.

In the theory of finite plasticity, the undistorted placement can be obtained at each instant by a local unloading process. For a given deformation $\boldsymbol{F}(t)$, let $\tilde{\boldsymbol{F}}^{-1}$ be the consecutive deformation of the elastic unloading, then

$$\boldsymbol{F}_p := \tilde{\boldsymbol{F}}^{-1} \boldsymbol{F}(t) \tag{3.32}$$

is the remaining stress-free deformation. The above mentioned unloading process is not unique, since $\boldsymbol{F} = \tilde{\boldsymbol{F}} \boldsymbol{Q}^{\mathsf{T}} \boldsymbol{Q} \boldsymbol{F}_p$ is also valid for each orthogonal tensor $\boldsymbol{Q}$.

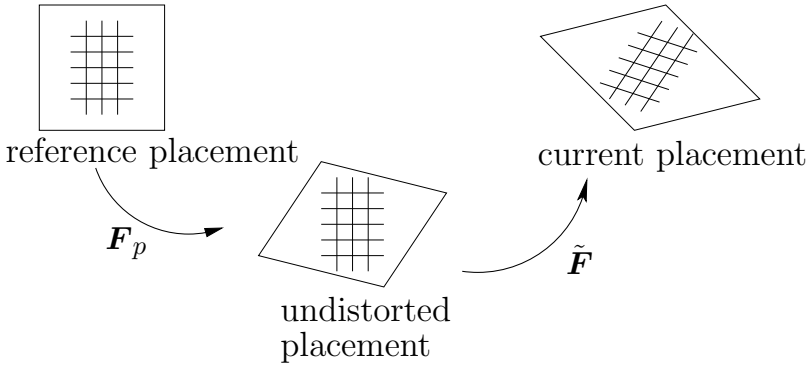

Figure 3.2: The reference, the undistorted and the current placements.

Following Lee (1969), the deformation gradient $\boldsymbol{F}$ is multiplicatively decomposed into the elastic part $\tilde{\boldsymbol{F}}$ and the plastic part $\boldsymbol{F}_p$ (see Figure 3.2)

$$\boldsymbol{F} = \tilde{\boldsymbol{F}} \boldsymbol{F}_p. \tag{3.33}$$

Asaro and Needleman (1985), Nemat-Nasser *et al.* (1998), and Lee *et al.* (1999) applied this concept of the decomposition of $\boldsymbol{F}$. $\tilde{\boldsymbol{F}}$ indicates the elastic distortion, the dilatation and the rotations which also account for any rigid body rotations. $\boldsymbol{F}_p$ indicates the crystallographic slipping along the slip system $(\boldsymbol{d}, \boldsymbol{n})$, in which $\boldsymbol{d}$ is the unit slip direction and $\boldsymbol{n}$ is the unit normal vector to the slip plane in the reference placement. $\boldsymbol{F}_p$ also gives the plastic incompressibility

$$\det(\boldsymbol{F}_p) = 1. \tag{3.34}$$

From the product of the deformation gradient $\boldsymbol{F}$ and the plastic transformation $\boldsymbol{P}$ in equations (3.26) and (3.28), and applying equation (3.33), we have

$$\boldsymbol{F}_p = \boldsymbol{P}^{-1}. \tag{3.35}$$

The multiplicative decomposition is not needed if equation (3.33) is deduced from the isomorphy concept. In this case, the elastic law in equation (3.24) is

$$\det(\boldsymbol{P})\boldsymbol{P}^{-1}\boldsymbol{T}^{2PK}\boldsymbol{P}^{-\mathsf{T}} = \tilde{\mathbb{C}}\left[\frac{1}{2}\left(\tilde{\boldsymbol{F}}^{\mathsf{T}}\tilde{\boldsymbol{F}} - \boldsymbol{I}\right)\right]. \tag{3.36}$$

We have the relation

$$\tilde{\boldsymbol{T}}^{2PK} = \det(\boldsymbol{P})\boldsymbol{P}^{-1}\boldsymbol{T}^{2PK}\boldsymbol{P}^{-\mathsf{T}}. \tag{3.37}$$

for the 2nd Piola-Kirchhoff stress between the undistorted placement and the reference placement. Applying $\tilde{\boldsymbol{C}} = \tilde{\boldsymbol{F}}^{\mathsf{T}}\tilde{\boldsymbol{F}}$, it follows that

$$\begin{aligned} \tilde{\boldsymbol{T}}^{2PK} &= \tilde{\mathbb{C}}\left[\frac{1}{2}(\tilde{\boldsymbol{C}} - \boldsymbol{I})\right] \\ &= \tilde{\mathbb{C}}[\tilde{\boldsymbol{E}}^{G}] \end{aligned} \tag{3.38}$$

for the elastic law. Analogously, the Kirchhoff and the Cauchy stress tensors can also be given in terms of $\tilde{\boldsymbol{F}}$.

3.2.2 Crystal Lattice and Slip Systems

Metals have crystalline structures. The plastic flow in metals is confined to certain crystallographic planes (slip planes) in certain crystallographic directions (slip directions) on the microscopic level. Crystalline structures of metals consist of the crystal lattices, the periodic nature of which allows us to fully describe these structures by the smallest crystal unit known as unit cell. The most common

lattices for metals are the face-centred-cubic (fcc) lattice, body-centred-cubic (fcc) lattice and the hexagonal (or close-packed hexagonal) lattice (hcp). Figure 3.3 shows the fcc and bcc unit cells. Table 3.1 lists some typical metals for fcc, bcc and hcp.

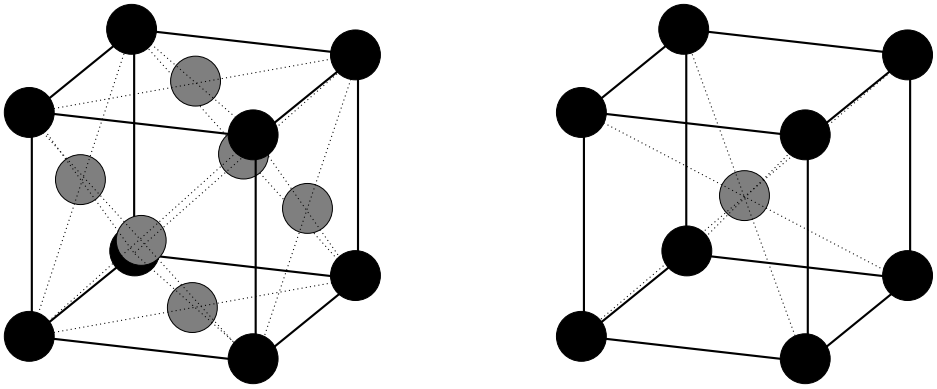

fcc bcc

Figure 3.3: Unit cell of fcc and bcc.

Lattices	Metals
fcc	Cu, Al, Ni, Au, γ-Fe (Austenite)
bcc	α-Fe (ferrite), Nb, Mo, W
hcp	Mg, Zn

Table 3.1: List of some metals sorted by crystal lattices.

In crystal plasticity, dislocation glide is essential for the permanent deformation of materials. It is necessary to specify the crystal structure to describe the motion of a single crystal deformed by the plastic slip.

Miller indices are used to distinguish a certain plane of the basic lattice and a direction lying on this plane. Detailed information about Miller indices may be found in, e.g., Gambin (2001). Taking into account the symmetry of crystallographic planes, and directions, and with the aid of the Miller indices, we present slip planes and directions in {hkl}<uvw> form, where {} presents multiple slip planes and <> gives multiple slip directions. For fcc materials and at room temperature, there are twelve slip systems {111}<101>, i.e., 4 glide planes $\times$ 3 glide directions. Table 3.2 lists the 48 slip systems for bcc[1] materials.

[1]At high temperature more slip systems than those given in Table 3.2 are possible (Gambin, 2001). However, we presently restrict our applications to room temperature.

Slip planes	Slip directions	Slip systems
{110}	<111>	$6 \times 2 = 12$
{112}	<111>	$12 \times 1 = 12$
{123}	<111>	$24 \times 1 = 24$

Table 3.2: List of 48 bcc crystallographic slip systems.

A particular slip system α can be specified by $\tilde{\boldsymbol{d}}_\alpha$ and $\tilde{\boldsymbol{n}}_\alpha$, which indicate the slip direction and the normal of the slip plane in the undistorted placement, respectively.

The resolved shear stress component along the slip direction on the slip plane (the resolved shear stress) initiates the plastic deformation (Schmid, 1924). The activation of a slip system α is related to the shear strain with the shear rate $\dot{\gamma}_\alpha$. There are different ways to specify the shear rate $\dot{\gamma}_\alpha$. Harder (1997) applied

$$\dot{\gamma}_\alpha = \dot{\gamma}_0 \ \mathrm{sgn}\left(\tau_\alpha - \tau_\alpha^B\right) \left(\frac{\tau_\alpha - \tau_\alpha^B}{\mu}\right)^2 \exp\left(\frac{\triangle F}{\kappa T} \frac{\left|\tau_\alpha - \tau_\alpha^B\right|}{\tau_\alpha^D}\right) \tag{3.39}$$

by taking the shear modulus μ, the absolute temperature T and the Boltzmann constant κ into consideration. $\dot{\gamma}_0$, τ_α, and τ_α^D indicate the reference shear rate, the resolved shear stress, and the drag stress in the slip system, correspondingly. $\triangle F$ and τ_α^B in (3.39) are activation entropies, and the scalar back-stress in each slip system, respectively. Méric *et al.* (1994) and Forest (1996) gave an ansatz for the viscoplastic approach

$$\dot{\gamma}_\alpha = \dot{\gamma}_0 \ \mathrm{sgn}\left(\tau_\alpha - \tau_\alpha^B\right) \left\langle \frac{\left|\tau_\alpha - \tau_\alpha^B\right| - \tau_\alpha^C}{\tau_\alpha^D} \right\rangle^m , \tag{3.40}$$

where τ_α^C and m are the critical resolved shear stress, and the strain-rate sensitivity parameter, respectively. The bracket $\langle x \rangle$ is defined by $(x - |x|)/2$. In equation (3.40), a slip system is activated when the resolved stress τ_α is larger than a critical value. We apply the ansatz

$$\dot{\gamma}_\alpha = \dot{\gamma}_0 \ \mathrm{sgn}\left(\tau_\alpha\right) \left|\frac{\tau_\alpha}{\tau_\alpha^C}\right|^m \tag{3.41}$$

(Hutchinson, 1976). $\dot{\gamma}_0$ is taken as constant for all the slip systems. Since the parameter m is generally larger than 80 (Bronkhorst *et al.*, 1992) at room temperature, the shear rate will increase when $\tau_\alpha \approx \tau_\alpha^C$.

3.2.3 Flow Rule

An evolution equation of $\boldsymbol{P}$ is needed to describe the flow behaviour. The ansatz for the flow rule applied in this work has the form

$$\begin{aligned} \boldsymbol{P}^{-1}\dot{\boldsymbol{P}} &= -\dot{\boldsymbol{F}}_p\boldsymbol{F}_p^{-1} = -\tilde{\boldsymbol{k}}(\tilde{\boldsymbol{T}}', \tau_\alpha^C) \\ &= -\sum_{\alpha=1}^{n} \dot{\gamma}_\alpha(\tilde{\boldsymbol{T}}', \tau_\alpha^C)\tilde{\boldsymbol{M}}_\alpha \end{aligned} \tag{3.42}$$

in the undistorted placement (Rice, 1971; Peirce *et al.*, 1982), where $\tilde{\boldsymbol{k}}$ is a constant function. n and $\tilde{\boldsymbol{M}}_\alpha$ are the number of slip systems and the Schmid tensor with $\tilde{\boldsymbol{M}}_\alpha = \tilde{\boldsymbol{d}}_\alpha \otimes \tilde{\boldsymbol{n}}_\alpha$, respectively. The Mandel tensor $\tilde{\boldsymbol{T}}$ is related to the Kirchhoff stress tensor $\boldsymbol{T}^K$ and given as

$$\tilde{\boldsymbol{T}} = \tilde{\boldsymbol{F}}^{\mathsf{T}}\boldsymbol{T}^K\tilde{\boldsymbol{F}}^{-\mathsf{T}}. \tag{3.43}$$

At room temperature, the slip systems of the fcc material harden approximately in an isotropic manner (Kocks and Mecking, 2003) such that only one critical resolved shear stress $\boldsymbol{\tau}^C$ remains in equation (3.41), i.e.,

$$\dot{\gamma}_\alpha = \dot{\gamma}_0 \ \mathrm{sgn}\,(\tau_\alpha)\left|\frac{\tau_\alpha}{\tau^C}\right|^m. \tag{3.44}$$

For simplicity and limited by the experimental data, this isotropic hardening concept is also used for the iron phase in this work. The same assumption for bcc is also adopted by Hartig and Mecking (2005). The resolved shear stress τ_α is given as

$$\tau_\alpha = \tilde{\boldsymbol{T}}' \cdot \tilde{\boldsymbol{M}}_\alpha. \tag{3.45}$$

The flow rule can also be equivalently written in terms of $\tilde{\boldsymbol{F}}$, i.e.,

$$\dot{\tilde{\boldsymbol{F}}}\tilde{\boldsymbol{F}}^{-1} = \boldsymbol{L} - \tilde{\boldsymbol{F}}\tilde{\boldsymbol{k}}(\tilde{\boldsymbol{T}}', \tau^C)\tilde{\boldsymbol{F}}^{-1}. \tag{3.46}$$

3.2.4 Hardening

The hardening rule is necessary to describe the evolution of the critical resolved shear stresses of all slip systems. When materials are under monotonous deformations (simple tension and compression) at room temperature, the plastic deformation is characterised by the accumulation of dislocations in the crystal lattice. The increase in the strength of the material that accompanies this accumulation is called work hardening. The Kocks-Mecking hardening rule (Voce rule) puts emphasis on the mechanisms of the dislocation movement, the accumulation, and the annealing. This rule is suitable to describe the hardening behaviour of the Fe-Cu composites in this work.

Kocks and Mecking (2003) summarised the work hardening in five stages according to the strain hardening rate ($\theta := \frac{\mathrm{d}\tau^C}{\mathrm{d}\gamma}$). These stages are:

- Stage I is the easy-glide stage and depends strongly on the orientation of the crystal. The slip occurs only on one crystallographic slip system in this stage. This mode of slip does not exist for polycrystals for which multiple slip systems are necessary from the beginning in order to maintain the material continuity at the grain boundaries.

- Stage II gives the steepest rate of strain hardening in the order of $\mu/200$ (μ: shear modulus) and depends on the orientation for both the single and the polycrystals.

- Stage III strongly depends on the temperature and the strain rate in both single crystals and polycrystals. The thermally activated processes (dynamic recovery), the dislocation annihilation and the rearrangement in stage III counteract the athermal dislocation storage by stage II processes.

- Stage IV is characterised by a very low hardening rate and the hardening rate of stage V drops to zero.

The aforementioned five stages in the work-hardening are better understood as regions in which one or another of the various processes dominates. The hardening mechanism concentrates majorly on stage II to III for materials in this work.

Based on observations in the dislocation theory of plasticity, the relation between the critical resolved shear stress τ^C and the dislocation density ρ can be given as

$$\tau^C = \alpha \ \mu \ b\sqrt{\rho} \tag{3.47}$$

with the magnitude of the Burgers vector b and a scalar constant α. α depends only weakly on the temperature and the geometrical arrangement of the dislocations. The flow stress σ and the critical resolved shear stress τ^C are related by the Taylor factor M which is defined as the ratio of the flow stress and the critical resolved shear stress ($M = \sigma/\tau^C$). The work-hardening rate is defined as

$$\Theta := \frac{\mathrm{d}\sigma}{\mathrm{d}\varepsilon}, \tag{3.48}$$

with the accumulated plastic strain ε. Θ is a direct measurement of the accumulation rate of the dislocations. Kocks and Mecking (2003) gave a detailed analysis for the fundamental interdependencies among the stress σ, the work hardening rate Θ, the temperature T, and the plastic strain rate $\dot{\varepsilon}$.

The Voce rule can be written as

$$\Theta = \Theta_0^* \left(1 - \frac{\sigma}{\sigma_v}\right) \tag{3.49}$$

with $\Theta_0^* = M^2\alpha\mu/(2\beta)$. In the context of finite deformations, the evolution of the density of the dislocation can be given as

$$\dot{\rho}(\tau_\alpha, \rho) = \left(\frac{\sqrt{\rho}}{\beta b} - \kappa \left|\frac{\dot{\gamma}(\tau_\alpha, \rho)}{\dot{\gamma}_0^*}\right|^{-\frac{1}{n}} \rho\right) \dot{\gamma}(\tau_\alpha, \rho) \tag{3.50}$$

where

$$\dot{\gamma}(\tau_\alpha, \rho) = \sum_{\alpha=1}^{N} \left|\dot{\gamma}_\alpha(\tau_\alpha, \tau^C(\rho))\right|. \tag{3.51}$$

$\dot{\gamma}_0^*$ is a material constant. β is a proportionality constant. In equation (3.50), the first term describes the statistical storage of the dislocations, i.e., the aforementioned stage II. The second term shows dynamic recovery processes which are assumed to be thermally activated and to increase in proportion to the density of stored dislocations. A detailed deduction for the work hardening is given in Kocks (1976) and Kocks and Mecking (2003). The evolution equation in terms of the critical resolved shear stress is

$$\begin{aligned} \dot{\tau}^C(\tau_\alpha, \tau^C) &= \Theta_0 \left(1 - \frac{\tau^C}{\tau_c^v(\tau_\alpha, \tau^C)}\right) \dot{\gamma}(\tau_\alpha, \tau^C), \\ \tau_c^v(\tau_\alpha, \tau^C) &= \tau_{c\,0}^v \left|\frac{\dot{\gamma}(\tau_\alpha, \tau^C)}{\dot{\gamma}_0^*}\right|^{1/n}, \\ \dot{\gamma} &= \sum_{\alpha=1}^{N} |\dot{\gamma}_\alpha| \end{aligned} \tag{3.52}$$

with the critical resolved shear stress τ^C and the number of considered slip systems N. In equation (3.52), $\dot{\gamma}$ presents the shear rate which is the sum over all systems. n is the stress exponent. $\Theta_0 = \alpha\mu/(2\beta)$, $\tau_{c\,0}^v = \alpha\mu/(\kappa\beta)$ and $\dot{\gamma}_0^*$ are input material parameters identified from experiments. In equation (3.52), Θ_0 is a characteristic strain hardening and τ_c^v is a scaling stress.

3.3 Viscoplasticity

3.3.1 Elastic Law

For the rigid viscoplastic material model, it is assumed that the distortion of the crystal lattice is purely viscoplastic, and the dilatation is purely elastic. Purely viscoplasticity means that the complete deformation or strain-rate is due to inelastic processes. In addition, the above two deformation modes are taken as decoupled. Although there are elastic stresses related to the volume changes in the model, it is called rigid-viscoplastic model. To formulate the elastic law, the Kirchhoff stress tensor $\boldsymbol{T}^K$ is additively decomposed into the spherical ($\boldsymbol{T}^{K\circ}$) and the deviatoric ($\boldsymbol{T}^{K\prime}$) part

$$\boldsymbol{T}^K = \boldsymbol{T}^{K\circ} + \boldsymbol{T}^{K\prime}. \tag{3.53}$$

$\boldsymbol{T}^{K\circ}$ is associated with the volume changes and indicates the equilibrium part of the stress tensor $\boldsymbol{T}^K$ (Šilhavý, 1997). The distortions in $\boldsymbol{T}^{K\prime}$ presents the dynamic part of the stress tensor $\boldsymbol{T}^K$ (Šilhavý, 1997).

Based on the aforementioned assumptions, the strain energy density depends only on the determinant $J = \det(\boldsymbol{F})$ of the deformation gradient. The strain energy density denoted as $W(J)$ is given as

$$W(J) = \frac{K}{4}\left(J^2 - 2\ln J - 1\right) \tag{3.54}$$

with K being the bulk modulus (Ogden, 1972; Simo and Miehe, 1992; Böhlke *et al.*, 2005). The above equation describes a convex curve. In equation (3.54), the strain energy density $W(J)$ goes to infinity, if J goes to infinity or to zero. As a result, the equilibrium stress is given by

$$\begin{aligned} \boldsymbol{T}^{K\circ} &= J\frac{\partial W(J)}{\partial J}\boldsymbol{I} \\ &= \frac{K}{2}\left(J^2 - 1\right)\boldsymbol{I}. \end{aligned} \tag{3.55}$$

3.3.2 Flow Rule

The inelastic deformation in the slip systems results in the viscoplastic distortions. The slip is assumed to be driven by the resolved shear stress in the corresponding slip system. It depends on the dynamical part (being equal to the deviatoric part) of the stress tensor. For the viscoplastic single crystal, the distortions can be modelled by

$$\begin{aligned} \boldsymbol{0} &= \boldsymbol{D}' - \boldsymbol{Q}\,\mathrm{sym}(\tilde{\boldsymbol{k}}(\boldsymbol{Q}^{\mathsf{T}}\boldsymbol{T}^{K\prime}\boldsymbol{Q}, \tau_\alpha^C))\boldsymbol{Q}^{\mathsf{T}}, \\ \dot{\boldsymbol{Q}}\boldsymbol{Q}^{-1} &= \boldsymbol{W} - \boldsymbol{Q}\,\mathrm{skw}(\tilde{\boldsymbol{k}}(\boldsymbol{Q}^{\mathsf{T}}\boldsymbol{T}^{K\prime}\boldsymbol{Q}, \tau_\alpha^C))\boldsymbol{Q}^{\mathsf{T}} \end{aligned} \tag{3.56}$$

(Hutchinson, 1976). $\boldsymbol{D}'$ and $\boldsymbol{W}$ are the traceless symmetric and the skew (antisymmetric) parts of the velocity gradient $\boldsymbol{L}$. The critical resolved shear stress

τ_α^C in each slip system is considered as an internal variable. The orientation of a single crystal is specified by an orthogonal tensor $\boldsymbol{Q}$. $\boldsymbol{Q}$ is specially chosen such that, for a given point, it maps the lattice vectors $\boldsymbol{g}_i^0$ at time $t = 0$ onto the lattice vectors $\boldsymbol{g}_i$ at time $t \geq 0$, i.e.,

$$\boldsymbol{g}_i(t) = \boldsymbol{Q}(t)\boldsymbol{g}_i^0. \tag{3.57}$$

If the initial lattice vector $\boldsymbol{g}_i^0$ coincides with the reference basis $\{\boldsymbol{e}_i\}$, the orthogonal tensor $\boldsymbol{Q}$ can be written as $\boldsymbol{Q} = \boldsymbol{g}_i(t) \otimes \boldsymbol{e}_i$.

Equation (3.56a) is an implicit equation for the stress deviator part $\boldsymbol{T}^{K\prime}$ when the deviator part of the strain rate, $\boldsymbol{D}'$, is given. Equation (3.56b) determines the spin $\dot{\boldsymbol{Q}}\boldsymbol{Q}^{-1}$ of the crystal lattice for given $\boldsymbol{T}^{K\prime}$, $\boldsymbol{W}$, and $\boldsymbol{Q}$. The equation (3.56) can also be deduced from the elasto-viscoplastic flow rule (3.46) by taking

$$\tilde{\boldsymbol{F}} = \tilde{\boldsymbol{R}}\tilde{\boldsymbol{U}} = \boldsymbol{Q}\tilde{\boldsymbol{U}}. \tag{3.58}$$

The function $\tilde{\boldsymbol{k}}(\boldsymbol{Q}^\mathsf{T}\boldsymbol{T}^{K\prime}\boldsymbol{Q}, \tau_\alpha^C)$ is assumed to be given by

$$\tilde{\boldsymbol{k}}(\boldsymbol{Q}^\mathsf{T}\boldsymbol{T}^{K\prime}\boldsymbol{Q}, \tau_\alpha^C) = \sum_{\alpha=1}^{N} \dot{\gamma}_\alpha(\tau_\alpha, \tau_\alpha^C)\tilde{\boldsymbol{M}}_\alpha \tag{3.59}$$

with

$$\begin{aligned} \dot{\gamma}_\alpha &= \dot{\gamma}_0 \ \mathrm{sgn}\,(\tau_\alpha) \left|\frac{\tau_\alpha}{\tau_\alpha^C}\right|^m, \\ \tau_\alpha &= (\boldsymbol{Q}^\mathsf{T}\boldsymbol{T}^{K\prime}\boldsymbol{Q}) \cdot \tilde{\boldsymbol{M}}_\alpha. \end{aligned} \tag{3.60}$$

τ_α is the resolved shear stress in the slip system α. m is the strain rate sensitivity parameter which is temperature related. In the limit as $m \to \infty$, a rate-independent behaviour is described. Note that equation (3.60) implies that the rate of the deformation is positively homogeneous of degree m in the stress tensor, whereas the stress is homogeneous of degree $1/m$ in the rate of deformation (Böhlke *et al.*, 2005).

The Kocks-Mecking hardening rule in section (3.2.4) is also applied in the viscoplastic material model.

The elastic law in the elasto-viscoplastic model directly gives the relation between the stress tensor and the strain tensor, where an elasticity tensor $\mathbb{C}$ (or $\tilde{\mathbb{C}}$) is necessary (see equations (3.18) or (3.38)). The elastic part of deformation gradient $\tilde{\boldsymbol{F}}$ can be calculated from the flow rule for the elasto-viscoplasticity model. The equilibrium stress in the rigid viscoplastic model is purely spherical, which is much simpler than the elasto-viscoplastic case. The deviatoric part of the stress tensor is determined by the symmetric part of the flow rule. No elasticity tensor appears in the rigid viscoplastic model. Only the orthogonal part of $\tilde{\boldsymbol{F}}$, i.e. $\boldsymbol{Q}$ in equation (3.58), can be determined by the flow rule in the rigid viscoplasticity model. In comparison to the elasto-viscoplastic model, the rigid viscoplastic model has a lower numerical effort.

Chapter 4

Homogenisation Techniques

The homogenisation theory establishes the macromechanical material behaviour based on constitutive equations of single crystals and takes into account the information of the microstructures. To describe the transition from the micro to the macro variables, we introduce a representative volume element (RVE). An RVE is a volume which contains a statistically representative volume fraction of the microstructure. Macro fields are determined through homogenising corresponding micro fields by appropriate averages over the RVE. In this chapter, the overall macroscopic quantities will be denoted by a superposed bar. For example, $\bar{\boldsymbol{F}}$ presents the deformation gradient on the macroscale, while $\boldsymbol{F}$ is the corresponding one on the local level. The volume average of the deformation gradient is

$$\bar{\boldsymbol{F}}(\boldsymbol{X},t) \;=\; \frac{1}{V}\int_{\mathcal{B}_0} \boldsymbol{F}(\boldsymbol{X},t)\,\mathrm{d}V, \tag{4.1}$$

with V the volume of the RVE. Equation (4.1) is a volumetric mean taken over the volume of the RVE in the reference placement. Based on the postulate of the equivalence of work on the micro and the macroscale (Hill, 1963), the local and the global 1st Piolar-Kirchhoff stresses are related by

$$\bar{\boldsymbol{T}}^{1PK}\cdot\dot{\bar{\boldsymbol{F}}} = \frac{1}{V}\int_{\partial\mathcal{B}_0} \boldsymbol{T}^{1PK}\cdot\dot{\boldsymbol{F}}\,\mathrm{d}V. \tag{4.2}$$

This postulate is the link of micro and macro quantities. By restricting the consideration to the quasi-static case and the homogeneous boundary condition or the periodic boundary condition, one achieves the average stresses

$$\bar{\boldsymbol{T}}^{1PK} = \frac{1}{V}\int_{\mathcal{B}_0} \boldsymbol{T}^{1PK}\,\mathrm{d}V. \tag{4.3}$$

Analogously, the macroscopic Cauchy stress can be calculated as

$$\bar{\boldsymbol{\sigma}} = \frac{1}{v}\int_{\mathcal{B}} \boldsymbol{\sigma}\,\mathrm{d}v \tag{4.4}$$

in the current placement, where v is the volume of the RVE in the current placement. However, the $\bar{\boldsymbol{T}}^{2PK}$ is not equal to the volume average of the microscopic 2nd-Piolar Kirchhoff stress

$$\bar{\boldsymbol{T}}^{2PK} \neq \frac{1}{V}\int_{\mathcal{B}_0} \boldsymbol{T}^{2PK}\,\mathrm{d}V, \tag{4.5}$$

since

$$\bar{\boldsymbol{T}}^{2PK} := \bar{\boldsymbol{F}}^{-1}\bar{\boldsymbol{T}}^{1PK} \neq \overline{\boldsymbol{F}^{-1}\boldsymbol{T}^{1PK}}. \tag{4.6}$$

The macroscopic measurement of Green's strain is defined by

$$\bar{\boldsymbol{E}}^{G} = \frac{1}{2}(\bar{\boldsymbol{F}}^{\mathsf{T}}\bar{\boldsymbol{F}} - \boldsymbol{I}). \tag{4.7}$$

Due to

$$\overline{\boldsymbol{F}^{\mathsf{T}}\boldsymbol{F}} \neq \bar{\boldsymbol{F}}^{\mathsf{T}}\bar{\boldsymbol{F}}, \tag{4.8}$$

$\bar{\boldsymbol{E}}$ is not a volume average of the microscopic Lagrangian strain $\boldsymbol{E}$

$$\bar{\boldsymbol{E}} \neq \frac{1}{V}\int_{\mathcal{B}_0} \boldsymbol{E}\,\mathrm{d}V. \tag{4.9}$$

4.1 Taylor and Sachs Models

The rigid plastic model for polycrystals (Taylor, 1938) successfully describes the stress-strain relation and the texture development of polycrystals with a high-stacking-fault energy under the uniaxial loading in terms of the single crystal

constitutive behaviour. The Taylor model assumes that the deformation field of the RVE is homogeneous and equals that of the macro one, i.e.,

$$\bar{\boldsymbol{F}} = \boldsymbol{F}. \tag{4.10}$$

This deformation field is compatible in the Taylor model on the micro level. The equilibrium is fulfilled inside each grain but not on the grain boundaries, since all the single grains are forced to deform in the same way as the aggregate. The macroscopic stress tensor is the average over the microscopic stress tensor of each element. The stress tensor is

$$\bar{\boldsymbol{\sigma}} = \frac{1}{v} \sum_{i}^{N} v_i \boldsymbol{\sigma}_i \tag{4.11}$$

with the total grain number N. v and v_i present the volume of the RVE and the volume of each grain in the current placement with $v = \sum_{i=1}^{N} v_i$.

The Taylor model fails to describe details observed in experiments due to its strict constraints. Honneff and Mecking (1978); Mecking (1981) modified these extreme assumptions in the form of the relaxed Taylor model in which some components of the strain tensor are considered as being unconstrained. Nevertheless, the Taylor model can predict basic features of polycrystalline deformations, e.g., the texture and the stress-strain curves.

In the sense of the Sachs model, one assumes a constant stress field. Sachs (1928) assumed a model with a homogeneous stress field for each grain. In this model, the micro stress is identical to the macroscopic stress

$$\bar{\boldsymbol{\sigma}} = \boldsymbol{\sigma}. \tag{4.12}$$

The deformation field is inhomogeneous and the macroscopic deformation gradient equals to

$$\bar{\boldsymbol{F}} = \frac{1}{V} \sum_{i}^{N} V_i \boldsymbol{F}_i, \tag{4.13}$$

where V_i is the element volume in the reference placement with $V = \sum_{i=1}^{N} V_i$. The equilibrium is trivially satisfied in this case but not the compatibility. Leffers (1968) described a relaxed Sachs model. This model permits the application of the additional stresses together with the basic stress system, where additional stresses will provoke multiple glide.

In single crystals, multislips are possible in the Taylor model while Sach's model, normally, has only single slip. The slip system, which is in the favourable position with regard to the loading direction, will be activated. Only when no slip system has such favourable position, can multislips occur in the Sachs model. Voigt (1910) approximated the elastic constants of polycrystals from those of single crystals by assuming a homogeneous deformation field. Reuss (1929) assumed an homogeneous stress field to deduce the elastic properties of polycrystals.

4.2 Self-consistent Models

In Hershey and Dahlgren (1954) and Kröner (1958) a self-consistent method was used in elasticity to determine average elastic polycrystalline constants in terms of the single crystal constants. In this method, a single crystal is taken to be embedded in an infinite medium with the average polycrystalline moduli (homogeneous equivalent medium). Eshelby (1957) proposed a model which took the interaction into account and allowed a stress-free plastic deformation of inclusions by considering a grain to be embedded in the matrix. Kröner (1958) used the solution of Eshelby (1957) to determine the elastic constants of polycrystals with isotropic distribution of the crystal orientation and the spherical grain shape. Kröner (1961) formulated the plastic deformation of polycrystals, where the orientations of grains were random.

Hill (1965) proposed an elasto-plastic model for polycrystals, in which both the single crystal and the matrix were considered as being elastic-plastic. To describe elastic-plastic properties of aggregates, the concept of the constraint tensor was introduced to the single crystal grain. The model in Budianski and Wu (1962) applied the elastic constraint to the single-crystal grain by surrounding aggregates while Hill's model defined the constraint by the plastically deformed aggregate. Hutchinson (1970) compared the stress-strain curves predicted by the

Kröner (1961), the Budianski and Wu (1962) and the Hill (1965) model for fcc polycrystals under tensile loading. He indicated that Hill's model was more realistic than others during the progression of the plastic deformation. Based on a creep power law, a study of the macroscopic relations between stress and strain rates for fcc polycrystals was given in Hutchinson (1976) by using the upper bound technique and the Hill (1965) self-consistent theory. In the rigid plastic case, results predicted by these two methods were similar for a wide range of the strain rates. Berveiller and Zaoui (1979) used a plastic accommodation model to predict the stress-strain behaviour of the polycrystal specimen in uniaxial tension. Another self-consistent approach was formulated for large deformations of polycrystals by Molinari *et al.* (1987). This rigid viscoplastic model is also applied to calculate the texture in tension, compression, and torsion, in which better results are shown than the predictions by the Taylor model. In Molinari *et al.* (1987) and Canova *et al.* (1992), the grain to grain interaction is taken into account. Harren *et al.* (1989); Weng (1981, 1982); Tóth and Molinari (1994) studied the rate-dependent polycrystalline response by applying self-consistent models. Another model (Nebozhyn *et al.*, 2001), variational self-consistent, was applied to compute the effective behaviour of the viscoplastic polycrystals by using the nonlinear homogenisation method of deBotton and Ponte Castaneda (1995). The effective stress vs. the strain-rate sensitivity curves were compared among the Taylor model, the Sachs model, the variational and other self-consistent models. Results have shown that incremental (Hill, 1965; Hutchinson, 1976) estimations tend to the Taylor model and tangent (Molinari *et al.*, 1987; Lebensohn and Tomè, 1993) are near to the Sachs bound, while the variational estimations remained distinct from the aforementioned models for all values of the strain-rate sensititvity parameter. This variational self-consistent model is especially suitable for ionic polycrystals, for which the effect of the grain shape is more significant than for the fcc case. Böhlke (2004) determined the Voigt bound of the stress potential of fcc polycrystals for all types of strain rate states. It has been shown that the isotropic Voigt bound of the stress potential depends strongly on the determinant of the strain rate deviator. This implies that the viscoplastic flow is not proportional to the stress deviator.

4.3 Finite Element-based Representative Volume Elements

The common disadvantage of the aforementioned (Taylor, Sachs and self-consistent) methods is that, for a given grain, the influence from neighbouring ones in the structure is neglected. Only in some special cases of the self-consistent model, is this effect taken into account. These approximate analytical approaches seem to be most accurate in limited cases: metals with high-symmetry and low-anisotropy single crystal grains (e.g., fcc and bcc). Under such conditions, the local fluctuations within each phase possibly do not play a significant role in determining the overall response (Dawson *et al.*, 1994). The overall mechanical behaviour of polycrystals strongly depends on the internal structure under large plastic deformations, in particular for the two- or the multi-phase materials. A good representation of the real microstructure including the grain geometry and the phase boundary is essential for the analysis of the overall behaviour of highly heterogeneous materials. In this case, microstructures assumed as spheres or ellipsoids embedded in an infinite medium, which is often used in self-consistent models, are insufficient to simulate the plastic deformation of polycrystals. Nygards and Gudmundson (2002b); Li *et al.* (2006) utilised Voronoi tessellations to present microstructures in their finite element simulations. Soppa *et al.* (2001, 2003) applied cut-outs of real microstructures to predict the mechanical behaviours of two-phase composites.

By postulating that the mechanical behaviour of all phases can be adequately predicted by the continuum constitutive relations, the aggregate deformation history is determined by solving equations of momentum and energy balances and the compatibility in conjunction with the phase constitutive relations, suitable initial conditions, and boundary conditions (Dawson *et al.*, 1994). For the complete boundary value problem solutions, the finite element method is a suitable numerical procedure for realistic microstructure models, while the equation system is too complex to be successful for the analytical solutions. If the initial boundary value problem on the microscale is solved by the finite element method, both the equilibrium and the compatibility are fulfilled in a weak sense. The finite element method based on the representative volume element should predict better results, if the properties of each phase of the material (or composite) are highly hetero-

geneous. This method accounts for the influences of neighbouring grains and can capture the effect of the geometrical shape and distribution of microstructural reinforcements on the overall material behaviour.

FE simulations with homogeneous boundary condition make the material structure stiffer and overestimate the material strength due to the restriction that the displacement of nodes on the boundary is independent of the inhomogeneous solutions inside the structure. Because of its simplicity and being directly used in standard-FE-software, it is also used, e.g., Takahashi *et al.* (1996); Kabir *et al.* (2006). The periodic boundary conditions allow for (periodic) fluctuations on the boundaries, and this improves the simulated results which are much nearer to the reality (e.g., Xia *et al.* (2003); Yang and Qin (2004)). But the PBC is more complex and, usually, needs extra codes and constraint equations to calculate the displacement on the boundary. Thus, more computational effort is necessary.

Finite element approaches can predict the material behaviour on a rather different scale covering from nano- to macro-level. Harder (1997) studied the local stress field. Kraska (1998) and Miehe *et al.* (1999) reported the macro-response according to certain textures. Bertram *et al.* (1997); Bertram (1999); Böhlke *et al.* (1997) studied the changes of the elastic properties due to an evolving crystallographic texture. Miehe and Schotte (2004) combined the polycrystal model with the finite element model to simulate the earing of deep-drawing of sheets, where the Taylor assumption was applied to the homogenization of Gauss points of the finite element model. Two different texture-dependent material models, i.e. an elastic-viscoplastic model based on the discrete orientations and a rigid-viscoplastic model, are discussed and applied to the simulation of deep drawing operations of aluminium in Böhlke *et al.* (2006b). In this work, they also took the Taylor assumption as the homogenization method for the Gauss points in FE simulations.

Mishnaevsky and Schmauder (1999) summarised the recent advances in the numerical modelling of strength, deformation, damage, and fracture of the heterogeneous material.

Chapter 5

Parameter Identification Based on the Taylor Model

5.1 Parameter Identification

5.1.1 Boundary Condition

We use the Taylor model to identify the input material parameters for the given polycrystals mentioned in chapter 1. The material parameters are estimated by simulating a uniaxial compression, i.e. simple compression, test and comparing the results with the corresponding experimental data (Commentz *et al.*, 1999).

The velocity gradient $\boldsymbol{L}$ (3.13) in the form of

$$\boldsymbol{L} = \dot{\gamma}_0 \frac{\boldsymbol{L}_1}{\|\boldsymbol{L}_1\|} \tag{5.1}$$

is kept constant which means that the material is loaded under a constant strain rate and spin. Since the material is assumed to be volume preserving, $\boldsymbol{L}_1$ in (5.1) is given as

$$\boldsymbol{L}_1 \hat{=} \begin{bmatrix} \frac{1}{2} & 0 & 0 \\ 0 & \frac{1}{2} & 0 \\ 0 & 0 & -1 \end{bmatrix}$$

with the unit of s^{-1}. Macroscopically, the plastic strain ($\bar{\varepsilon}_p$ in the loading direction) and the height (h) of the specimen after the loading are presented as

$$\begin{aligned} \bar{\varepsilon}_p &= -\ln \frac{h}{h_0} \\ h &= h_0 - \Delta h \end{aligned} \tag{5.2}$$

where h_0 and Δh denote the initial height and the displacement of the specimen.

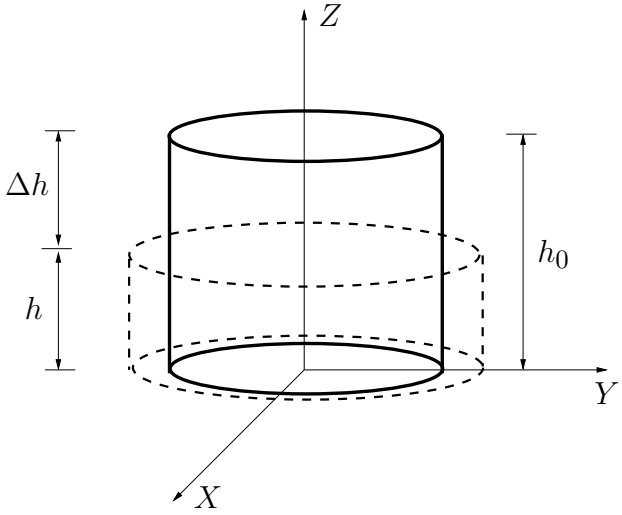

Figure 5.1: A sketch of the specimen before (solid lines) and after (dashed lines) a uniaxial compression load.

The corresponding variables in equation (5.2) are shown in Figure 5.1. The Cauchy stress in the loading direction (σ_{zz} in (3.19)) matches the true stress in the experiment. The macroscopic strain ε is numerically calculated as

$$\begin{aligned} \boldsymbol{F}(t) &= \exp(\boldsymbol{L}t)\boldsymbol{F}_0 \\ \boldsymbol{u}(\boldsymbol{X},t) &= \boldsymbol{H}(t)\boldsymbol{X} \\ &= (\boldsymbol{F}-\boldsymbol{I})\boldsymbol{X} \\ \varepsilon &= -\ln \frac{x_z}{X_z} \end{aligned} \tag{5.3}$$

with the reference displacement gradient $\boldsymbol{H}$ (see equations (3.5) and (3.11)). x_z

and X_z ($X_z \neq 0$) present the loading direction component of the position tensor in the current and the reference placement, respectively. If a special orthogonal basis is chosen as in Figure 5.1, the reference displacement gradient equals to the spatial displacement in the simple compression case. Initially, $\boldsymbol{F}_0$ is given as

$$\boldsymbol{F}_0 \hat{=} \begin{bmatrix} 1 & 0 & 0 \\ 0 & 1 & 0 \\ 0 & 0 & 1 \end{bmatrix}.$$

The elastic part of the deformation gradient $\tilde{\boldsymbol{F}}$ is equal to the crystal orientation $\boldsymbol{Q}$ (see (3.58)) at the beginning of the loading with

$$\tilde{\boldsymbol{F}}(0) = \boldsymbol{Q}, \tag{5.4}$$

since no residual stress is considered in the material which means that the right stretch tensor $\tilde{\boldsymbol{U}}$ is the unit tensor.

5.1.2 Material Parameters

Three independent components of the elasticity tensor $\tilde{\mathbb{C}}$ (3.22) in the cubic symmetry case are presented in Table 5.1 (Commentz *et al.*, 1999).

Material	$\tilde{C}_{1111}$(GPa)	$\tilde{C}_{1122}$(GPa)	$\tilde{C}_{2323}$(GPa)
Cu	166.1	119.9	75.6
Fe	230.1	134.6	116.6

Table 5.1: Three independent components of the elasticity tensor $\tilde{\mathbb{C}}$ in cubic symmetry case for Cu and Fe.

Twelve glide systems[1] $\{111\}\langle 110\rangle$ are considered for the fcc and twelve glide systems $\{110\}\langle 111\rangle$ are for the bcc crystals, respectively. According to Gottstein (2001), the shear stress in the glide plane, called Peierls stress, is proportional to the shear modulus, and (exponentially proportional) to the Burgers vector (glide direction), but exponentially antiproportional to the distance of the glide planes. Among the $\{110\}\langle 111\rangle$, $\{112\}\langle 111\rangle$, and $\{123\}\langle 111\rangle$ glide systems in the bcc, the $\{110\}\langle 111\rangle$ glide systems are firstly activated, because the Peierls stress

[1]Details concerning glide planes and glide directions for both the fcc (Cu) and the bcc (Fe) are shown in the tables B.1 and B.2 in appendix B.

is the smallest one for them. Furthermore, the dislocation motion at the beginning of the yielding strongly affects the texture development. The simplicity for the simulation is another reason for just considering twelve glide systems for bcc crystals.

Material	$\dot{\gamma}_0(s^{-1})$	m	$\dot{\gamma}_0^*(10^7 s^{-1})$	n
all	0.001	80	1.0	46.3

Table 5.2: Constant material parameters for Fe/Cu and their composites.

Table 5.2 lists values of the constant parameters[1] applied in the simulation. Other values of $\dot{\gamma}_0^*$ are also possible, but it should be kept in the same magnitude which is expected from the dislocation theory. Firstly, n is determined for the pure Cu by the experimental curves in Kocks and Mecking (2003). Limited by experimental data and for simplicity, this parameter (n) is also applied for the pure Fe and iron-copper composites. It is found that the stress exponent n does not influence the texture development much (Canova *et al.*, 1988). Isotropic hardening is assumed for the simulation.

Material	${\tau_c^v}_0$(MPa)	${\tau_c}^0$(MPa)	Θ_0
Cu	258	70	330
Fe	436	187	750

Table 5.3: Hardening material parameters for the pure Cu and the pure Fe determined by the trial-and-error method.

Table 5.3 presents the material parameters which are determined by the trial-and-error method for the pure Fe and the pure Cu. Figure 5.2 shows the comparison of the stress-strain curves between the Taylor simulation and the experiment.

For the numerical solution in Figure 5.2, the Cauchy stress is the average of 1000 initially arbitrarily oriented crystals with identical volume fraction. The stress of the Fe-Cu composite is also determined by 1000 initially arbitrarily oriented crystals, in which the Fe phase includes 500 crystals. Since the volume fraction of each phase is an essential factor which influences the strength of the composite, the rule of mixture (ROM)

[1]The meaning of the corresponding material parameters is referred to section 3.2.2 and 3.2.4.

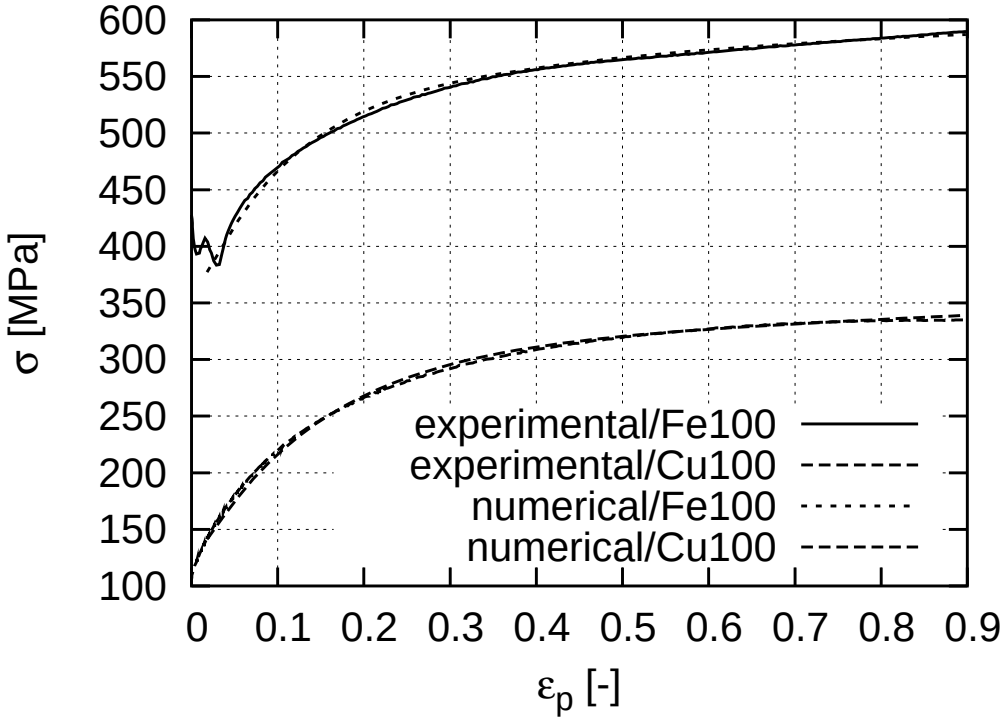

Figure 5.2: Numerical and experimental stress-strain curves of the pure Fe and the pure Cu under the compressive load until 90% plastic strain.

$$\boldsymbol{\sigma} = \boldsymbol{\sigma}^d_{Fe}\ v_{Fe} + \boldsymbol{\sigma}^d_{Cu}\ v_{Cu}, \tag{5.5}$$

is used to calculate the stress of the composite. v_{Fe} and v_{Cu} in equation (5.5) indicate the volume fraction of the Fe and the Cu phase in the current placement, correspondingly. The stress $\boldsymbol{\sigma}^d_{Fe}$ is the Cauchy stress for the Fe phase, where the upper index "d" means that the stress is obtained by applying the input parameters of the pure iron in Table 5.3. Analogously, $\boldsymbol{\sigma}^d_{Cu}$ has the same meaning for the Cu phase.

In Figure 5.3 and 5.4, "direct matching" means that the stress of the composite is calculated by using the parameters of the pure Fe and the pure Cu in Table 5.3. The flow stress predicted by the Taylor simulation for the Fe17-Cu83 composite is lower than that of the experiment (see Figure 5.3), but it is higher than the experimental one for the Fe83-Cu17 composite (see Figure 5.4). The aforementioned deviations of the numerical stress-strain curves from the experimental ones mean that the rule of mixture cannot predict well the stress of the Fe-Cu composites by

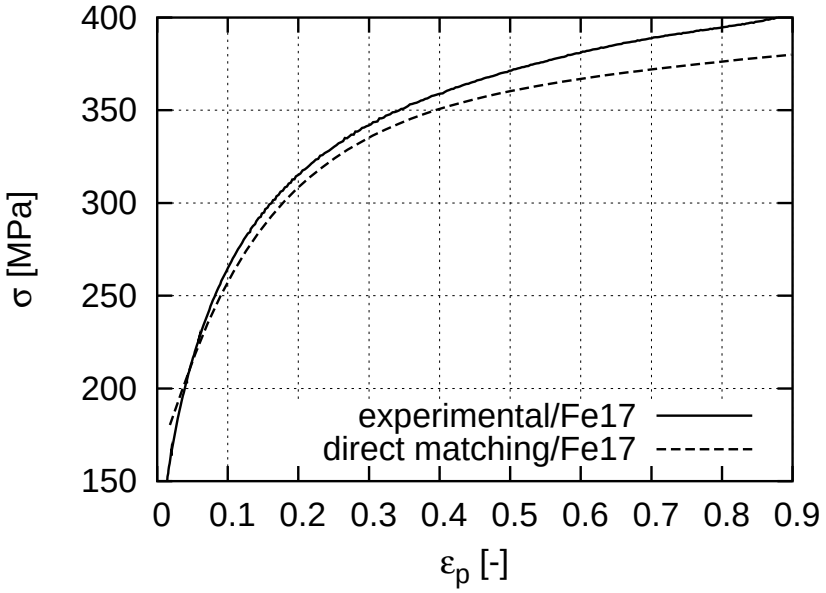

Figure 5.3: Numerical and experimental stress-strain curves of the Fe17-Cu83 composite under the compressive load until 90% plastic strain where input parameters for the Fe/Cu phase are identical to those of the pure Fe/Cu.

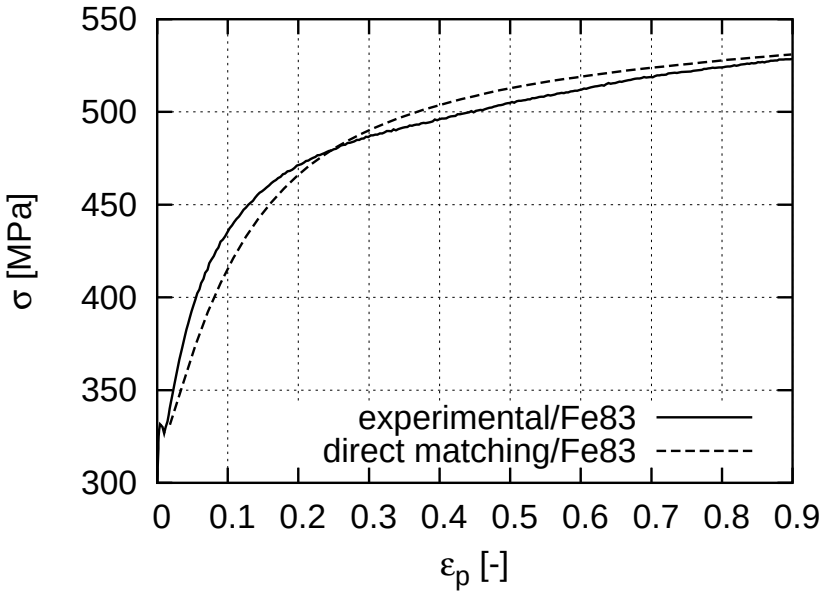

Figure 5.4: Numerical and experimental stress-strain curves of the Fe83-Cu17 composite under the compressive load until 90% plastic strain where input parameters for the Fe/Cu phase are identical to those of the pure Fe/Cu.

using the material parameters of the pure Fe and the pure Cu.

Raabe *et al.* (1995) also presented the same phenomenon where the (macroscopic) tensile strength of the Cu-20 mass% Nb was much greater than that expected from the rule of mixture. The deformation of the two-phase polycrystals is strongly influenced by the incompatibility of the deformation of the fcc and the bcc phases. The softer phase has to undergo a higher local deformation than the harder phase (see e.g. Raabe *et al.*, 1995; Commentz *et al.*, 1999) and this modifies the local stress distribution. These facts indicate that the modification of the rule of mixture is necessary.

In order to capture the extra high strength in the composites in which the volume fraction of the harder phase is approximately 20%, Hangen and Raabe (1995) described the yield strength of the metal matrix composite (MMC) in terms of a modified linear rule of mixtures. The yield strength of the composite, $\sigma_{RP0.2}$[1], is considered as the sum of the volumetric weighted average of the yield strength of each phase (conventional rule of mixtures), presented as σ_{ROM}, and a Hall-Petch type contribution attributed to the impact of the Cu-Nb phase boundaries, presented as σ_{MMC}. At a certain macroscopic strain, the term σ_{MMC} includes influences from the distance of the phase boundaries, the pile-up of the dislocations on the phase boundaries, the Burgers vector, the filament thickness and the spacing, etc. Ratke *et al.* (1984) presented that the Fe-Cu composites manifested a pronounced interphase hardening mechanism by studying the age hardening in ultrafine composite wires under thermal treatment. The yield stress of such composite wires is quantitatively treated as a linear approximation from the yield stress of the Fe and the Cu phase (σ_{Cu} and σ_{Fe}). The yield stress in each phase (σ_{Cu}, σ_{Fe}) is affected by five different factors, namely:

1. the yield stress of the pure Cu and pure Fe,
2. the additional yield stress due to the solid solution hardening,
3. the part due to the age-hardening by particles,
4. the influence of the grain boundaries,

[1]Because of the simple tension test, only yield stresses in the loading direction are considered.

5. the additional increase due to the phase boundaries.

To modify the rule of mixture, methods in both Hangen and Raabe (1995) and Ratke *et al.* (1984) are, firstly, suitable for the special composite mentioned in the corresponding literature and, secondly, they require the corresponding experimental measurements as input material parameters. Concerning this work, the hardening rule in section 3.2.4 is still preferred because of its simplicity and applicability for the mentioned Fe-Cu composites. Aiming to match the experimental data, however confined by the limited measurements obtained from experiments, a modification of the material parameters of the pure iron and the pure copper is performed to find suitable input parameters for each Fe-Cu composite. Material parameters of the pure Fe and Cu provide the first guess for the new ones of the composites. Due to the fact that the strength of the copper phase (in Fe-Cu composites) is enhanced by the presence of the iron phase (Commentz *et al.*, 1999), the stress of the Cu phase is considered as higher than that of the pure copper and, simultaneously, lower than that of the given composite during the trial process (of searching for the suitable material parameters). Analogously, the Fe phase has a strength which is lower than that of the pure iron and higher than that of the composite. The above consideration also fits for the experimental observation that the harder phase takes more strength than the softer one in such two-phase polycrystals.

The calculation of the composite stress is based on equation (5.5), but the stress of each phase is obtained from the modified material parameters. The new form for such calculation can be written as

$$\boldsymbol{\sigma} = \boldsymbol{\sigma}_{Fe}\ v_{Fe} + \boldsymbol{\sigma}_{Cu}\ v_{Cu}, \tag{5.6}$$

where $\boldsymbol{\sigma}_{Fe}$ and $\boldsymbol{\sigma}_{Cu}$ mean that stresses of both the Fe and the Cu phase are determined by the new input parameters which are given in Table 5.4. Figures 5.5 to 5.9 present the comparison between numerically and experimentally determined stress-strain curves.

Material	$\tau_c^v{}_0$(MPa)	$\tau_c{}^0$(MPa)	Θ_0
Fe(vol.%)/Cu (vol.%)	Fe/Cu	Fe/Cu	Fe/Cu
Fe17-Cu83	405/280	180/70	780/330
Fe33-Cu67	360/280	180/80	800/466
Fe50-Cu50	403/276	186/80	830/490
Fe67-Cu33	415/275	186/80	860/430
Fe83-Cu17	415.5/280	186/80	892/450

Table 5.4: Hardening material parameters for Fe-Cu composites determined by the trial-and-error.

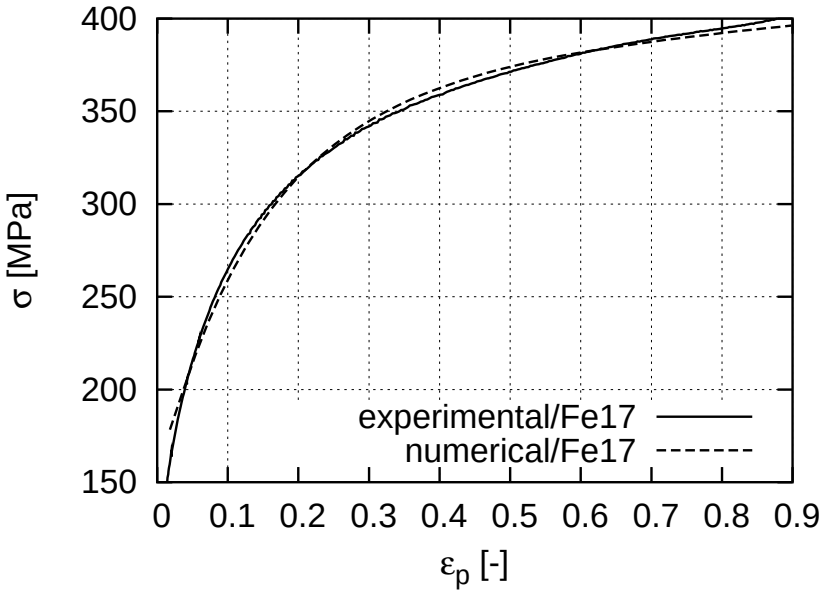

Figure 5.5: Numerical and experimental stress-strain curves of the Fe17-Cu83 composite under compressive load until 90% plastic strain.

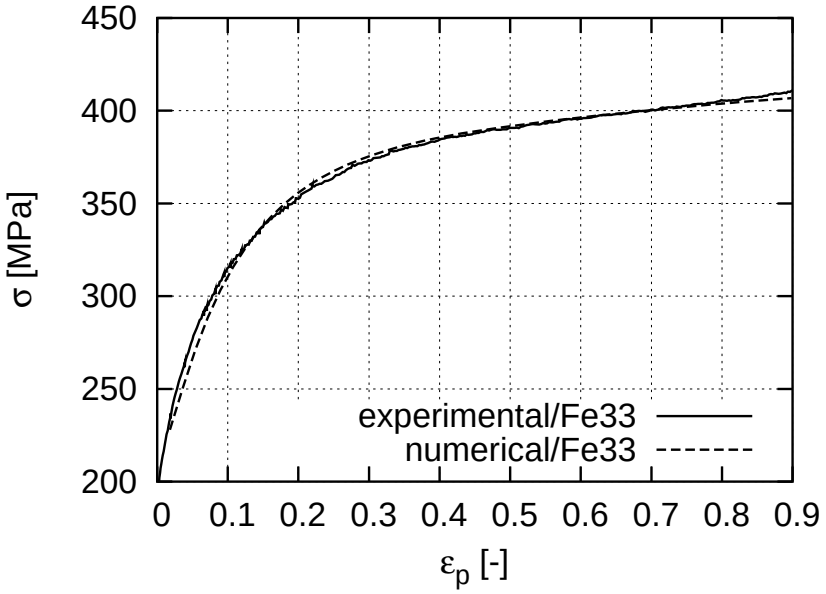

Figure 5.6: Numerical and experimental stress-strain curves of the Fe33-Cu67 composite under compressive load until 90% plastic strain.

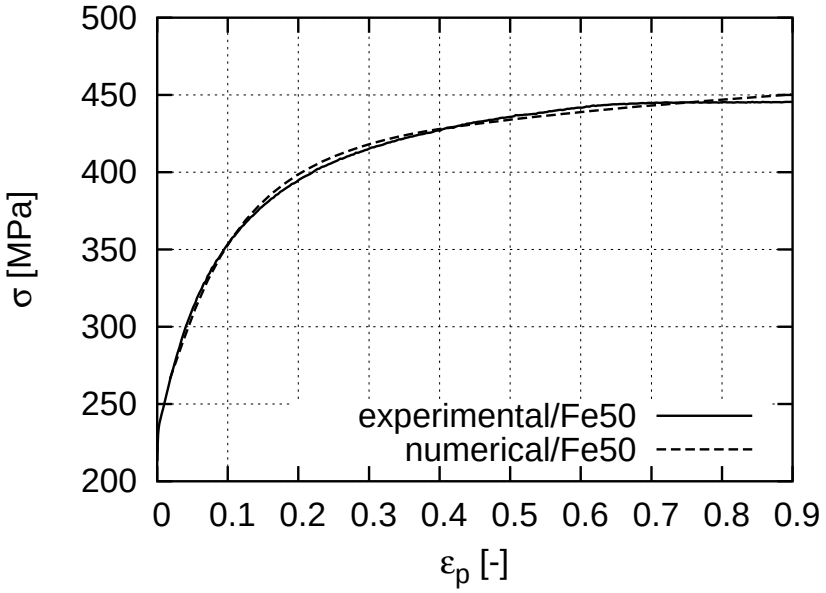

Figure 5.7: Numerical and experimental stress-strain curves of the Fe50-Cu50 composite under compressive load until 90% plastic strain.

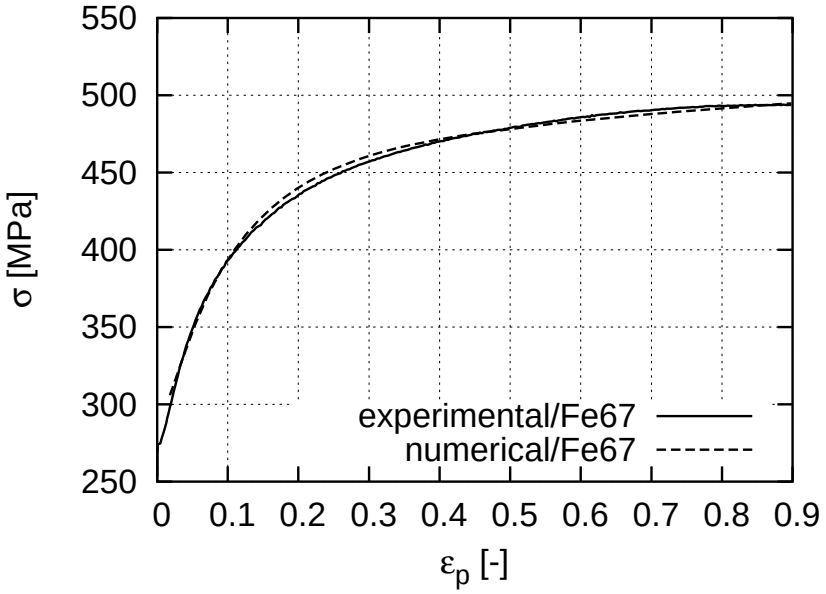

Figure 5.8: Numerical and experimental stress-strain curves of the Fe67-Cu33 composite under compressive load until 90% plastic strain.

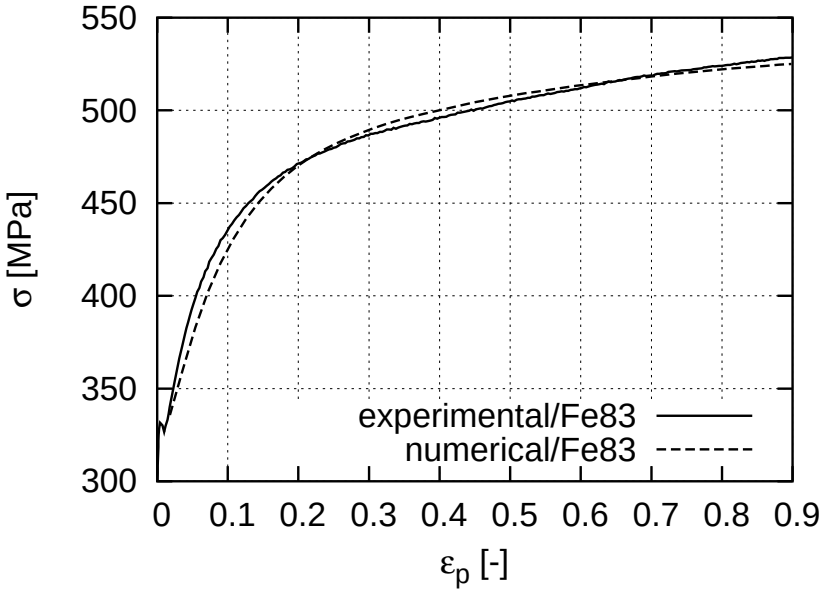

Figure 5.9: Numerical and experimental stress-strain curves of the Fe83-Cu17 composite under compressive load until 90% plastic strain.

Chapter 6

Axisymmetric Finite Element Simulations

6.1 Introduction

The finite element model is very applicable for the complex structure, the inhomogeneity, and the anisotropy. To predict the mechanical behaviour in detail for the two-phase polycrystals with a high local heterogeneity as the iron-copper polycrystals, the finite element simulation is the suitable homogenisation technique. Polycrystal plasticity is appropriate for the aforementioned materials under large plastic deformations. This theory can describe the main micromechanisms that are responsible for the observed macroscopic phenomenon of the plastic deformation. It can also describe such items as internal stresses, the texture development due to large plastic deformations, and the effect of the grain size and shape. Since polycrystals consist of an enormous number of grains, their properties are influenced not only by characters of the individual grains but also by the interaction between them and, particularly, the interaction between phases for two-phase polycrystals.

The structure in the material has a strong effect on the plastic deformation pattern. Furthermore, simulations, in which structures present the real microstructures more precisely, can predict better results. Therefore, 2D real microstructures are applied as cross-sections of axisymmetric models presented in this chapter. We incorporate a realistic morphology, the internal interphase and the grain orientation in the model to simulate complex mechanisms of Fe-Cu polycrystals under the

large plastic deformation. The axisymmetric simulation[1] with the assumption of a finite length in the third direction (hoop direction) should give better predictions than 2D ones with the assumption of the infinite length in the third direction. LLorca and Segurado (2004) compared the results of the axisymmetric simulation with that of the 3D one to analyse the effect of the reinforcement volume fraction and the matrix damage parameters on the composite behaviour.

6.2 Morphology Identification from Real Microstructures

Based on their results predicted by the self-consistent model, Commentz *et al.* (1999) recommended using a model, which takes into account local micromechanical interactions among grains, to more successfully simulate the texture of two-phase polycrystals. Through studying Ag-Ni two-phase polycrystals, Soppa *et al.* (1998) concluded that the deformation process was significantly determined by the interaction between phases. A mesh net with more and smaller elements for the simulated structure is one way to emphasize the importance of the interaction among grains and phases. But by considering the cost of the simulating time, the relative finer meshing on grain boundaries[2] is preferred.

In order to fulfill the above requirements, the mesh is generated by the public domain software OOF (NIST, 2003). This software is aimed to investigate properties of the microstructure for the material simulation when the physical/mechanical properties depend on microstructural details, such as the spatial correlation of the crystallite orientation, the shape and the dispersion of the second phase and local anisotropies.

Figure 6.1 and Figure 6.2 with subfigures of (a), (b), (c) and (d) present the real microstructure, identified phases (black: Fe, white: Cu), identified grains (relative darker ones present Cu grains), and the finite element net with the refined mesh

[1]The axisymmetric simulation is viewed as a special 3D simulation, because it also presents all the 3D information.

[2]Phase boundaries are included in grain boundaries. In this work, we consider that grain boundaries include Fe-Fe, Cu-Cu and Fe-Cu (grain) boundaries. Phase boundary always means the Fe-Cu (grain) boundaries.

on grain boundaries, respectively. Element edges are aligned on grain boundaries. There are no multiphase elements, which means that all the integration points belonging to the same element have identical material properties. The Fe17-Cu83 composite should give a better view of the material flow behaviour than other Fe-Cu composites, because it is composed with a large volume fraction of the copper phase, and the softer phase is the major one which flows in the whole material structure. The Fe50-Cu50 composite provides the largest possibility for phase-to-phase interaction. And this interaction is the key point to study the local deformation behaviour of two-phase polycrystals with large differences in the strength.

Figure 6.3 shows an image of such axisymmetric models. The smallest coordinate of all the nodes in Figure 6.1(d) and 6.2(d) is chosen as 100 in both the X and the Y direction. The 3D model, which is presented by the axisymmetric simulation, is obtained by revolving a symmetrical cross-section.

Table 6.1 lists the information about the number of identified iron and copper grains, the total number of elements, and the element type used in the simulation for the Fe17-Cu83 and the Fe50-Cu50 composite (Figure 6.1(c)(d) and 6.2(c)(d)). The extra marked grain Cu_a in Figure 6.2(c) is a very large grain of the softer phase, the diameter of which is approximately one-half of the total length in the transverse (horizontal) direction and one-third in the loading (vertical) direction. This special grain is supposed to undergo an even larger plastic deformation than the mean value.

Composite	Fe Vol(%)	Grain number		Element	
		Fe phase	Cu phase	total number	type
Fe17-Cu83	22	34	47	10327	CGAX3H
Fe50-Cu50	49	38	29	9449	CGAX3H

Table 6.1: The volume fraction of the Fe phase, the number of grains for the iron/copper phase, the total number of the elements, and the element type for the Fe17-Cu83 and the Fe50-Cu50 composite (Figure 6.1(d) and Figure 6.2(d)).

Due to the fact that the volume of the material associated with the element is that of a body revolution, as shown in Figure 6.3, the volume of a given phase calculated from the 2D axisymmetric cross-section may not exactly present the volume

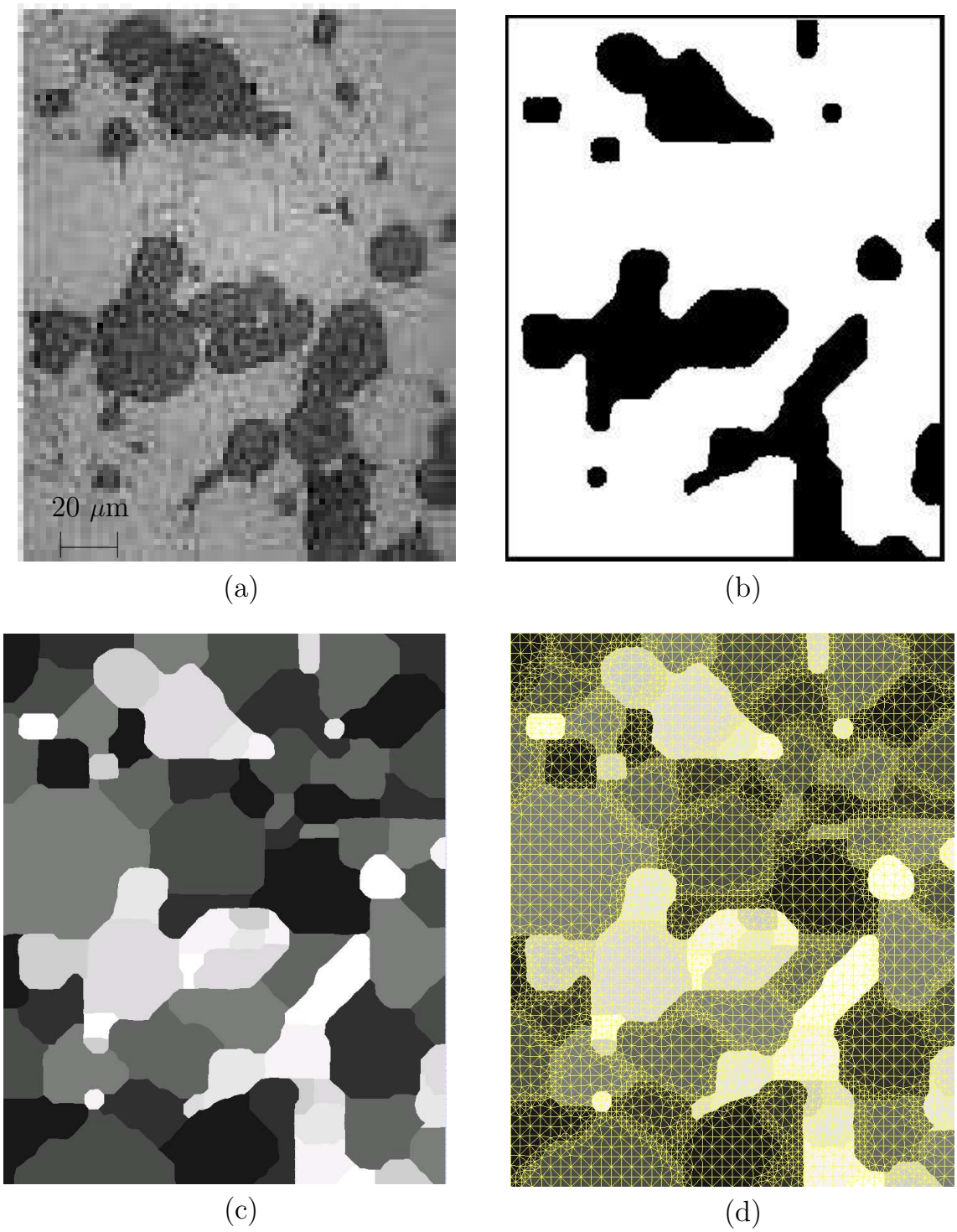

Figure 6.1: The real microstructure (a), the modelled microstructure with the darker phase Fe (b), modelled grains (c), and the finite element net (d).

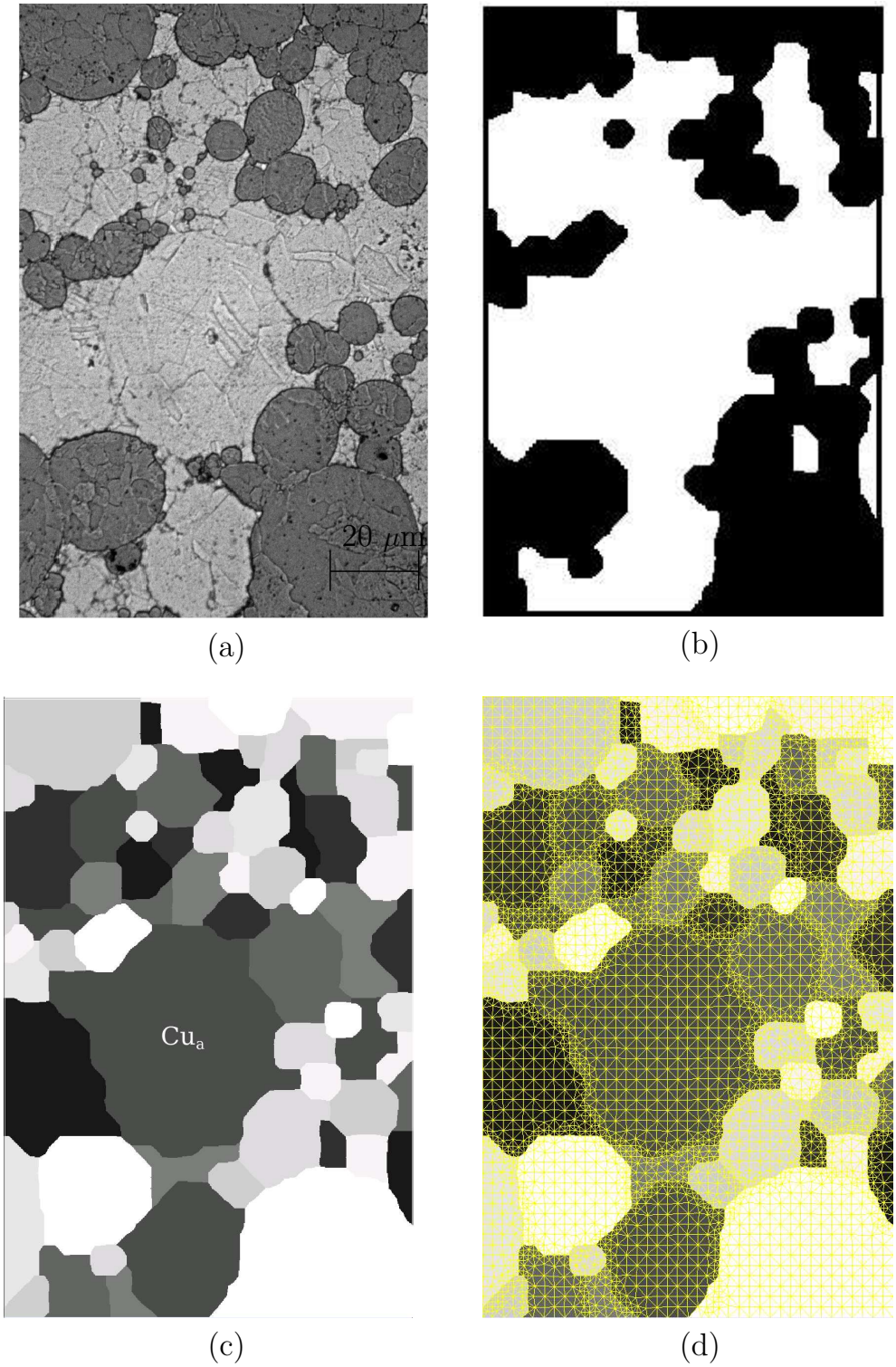

Figure 6.2: The real microstructure (a), the modelled microstructure with the darker phase Fe (b), modelled grains (c), and the finite element net (d).

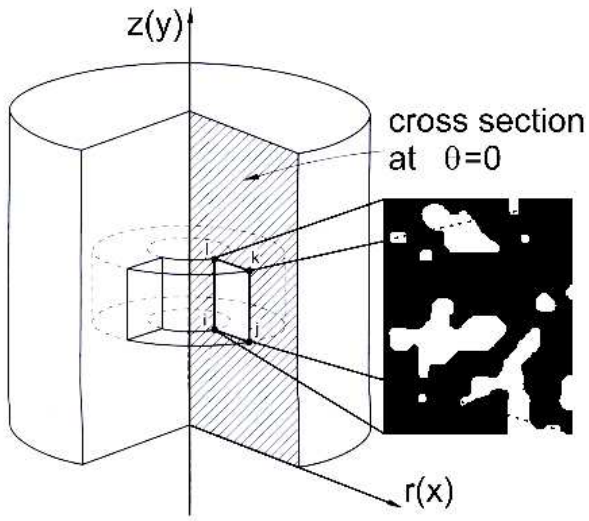

Figure 6.3: A sketch of an axisymmetric model (ABAQUS/Standard, 2003) where the 2D microstructure is cut out from a cross-section of a cylindrical sample.

in the (experimental) 3D case. The volume fraction of the iron phase is 22% and 49% in the simulation for the above-mentioned two composites, respectively. Since there are high heterogeneity and anisotropy in Fe-Cu two-phase polycrystal structures, the element type applied in the models is CGAX3H which belongs to the generalized axisymmetric solid element (ABAQUS/Standard, 2003). Due to the automatic mesh refinement on grain boundaries, the meshing could not provide a corresponding node on the opposite side for each boundary node. Therefore, homogeneous boundary conditions are applied for the simulation.

6.3 Local Behaviour under Simple Compression

6.3.1 Solution Mapping Technique for Large Plastic Deformations

In modelling a material structure under large plastic deformations, the mesh that has deformed significantly from its original configuration has to be replaced by a new mesh with a better quality in order to continue the analysis, i.e., remeshing is necessary. When the strain becomes large in the geometrically nonlinear analysis, generally, elements become so severely distorted that they no longer provide a good discretisation of the problem and could even cause inaccurate solutions.

Besides the plastic or the viscoplastic calculation, the modelling of the rubber elasticity problems, manufacturing processes, fracture propagations in materials and structures, and crack development also frequently require remeshing techniques. By applying the remeshing technique to trace the crack geometry as well as to preserve an adequate element shape, Mediavilla *et al.* (2006) focused their study on the numerical and stability aspects related to the discrete crack propagation in the quasi-static ductile fracture. Logé and Chastel (2006) presented some numerical strategies which included automatic remeshing and can be applied to couple the finite element formulation to metallurgical models. In this work, the loading process could not be performed until ε_p=90% due to the serious distortion of some elements located on grain boundaries or shear bands. The plastic property of a single Fe or Cu grain in its composite is highly anisotropic and related to the grain orientation. When such polycrystals are subjected to large plastic deformations, the strain between neighbouring grains with different orientations is highly incompatible, and the deformation ability of some elements is exhausted before reaching the desired amount of the deformation.

It is one of the necessary steps in such remeshing analysis to map a solution from the old mesh to the new one. Concerning the solution mapping algorithm in ABAQUS (ABAQUS/Standard, 2003), the interpolation technique obtains the solution variables at the nodes of the old mesh by extrapolating all values from the integration points to the nodes of each element and then averaging these values over all similar elements abutting each node. Consequently, variables of the integration point in the new mesh are assigned from the nodes of the old element in which this (new integration) point is located. When this default solution mapping algorithm is applied to the current problem (simulation of the local micromechanical behaviour of Fe-Cu polycrystals by using the real microstructure under large plastic deformations), new elements on the grain boundaries in an Fe grain obtain variables which are averaged from other (old) Fe grains and even from (old) Cu grains. The same problem of the solution mapping also occurs for elements of Cu grains. Such grain boundary elements[1] take quite an amount of the total volume in the material structure used for the simulation (Figure 6.1(d) and 6.2(d)). This causes great inhomogeneity among integration points even in the same grain. Ad-

[1]In this work, the ratio between the mesh after refinement on grain boundaries and that before is approximately 3-4 for the total number of the elements.

ditionally, since high anisotropy and heterogeneity exist among the Fe-Fe, Cu-Cu and Fe-Cu grains, ABAQUS could not start the calculation for the newly meshed structure.

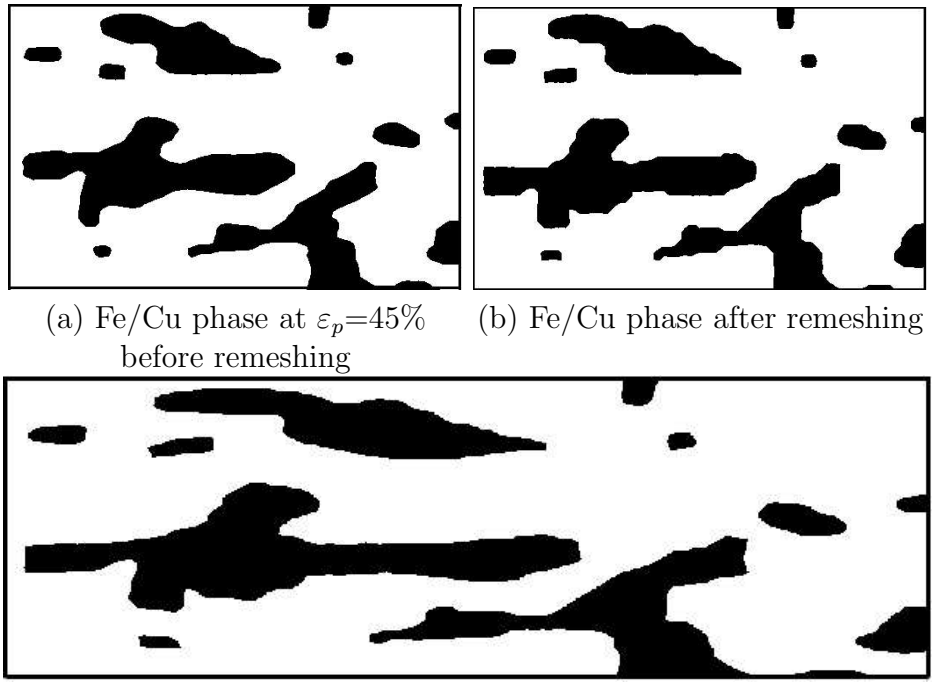

(a) Fe/Cu phase at ε_p=45% before remeshing

(b) Fe/Cu phase after remeshing

(c) Fe/Cu phase at ε_p=90%

Figure 6.4: The iron and the copper phase (black: iron, white: copper), the phase boundary at deformed states predicted by the viscoplastic material model and with the remeshing technique ((a): end state of the 1st calculation, (b): initial state of the 2nd calculation after remeshing, (c): end state of the 2nd calculation).

Figure 6.4(a) presents the deformed iron and copper phase at ε_p=45% at the end of the first calculation (before remeshing), Figure 6.4(b) shows the modelled Fe and Cu phases (identified from the 6.4(a)) at the beginning of the second calculation and 6.4(c) shows the final deformed Fe and Cu phases at ε_p=90% at the end of the second calculation. The tool for the remeshing is still OOF mentioned in Section 6.2. The mesh is also refined on grain boundaries for the new model which has 11,258 elements in total. The solution mapping is done with a grain-to-grain mapping. For a given integration point A in the new mesh, its internal variables are mapped from an integration point B in the same grain of the old mesh. The condition for this mapping is that the distance between points A and B is minimum. Thus, it avoids the problem of mixing properties of the Fe and the Cu in assigning internal variables for the new integration point. The aim of this Section (6.3.1) is to provide a method (remeshing) to solve the

problem of simulating the large plastic deformation for the highly heterogeneous and anisotropic material with a complex morphology.

Whenever the solution is mapped from another mesh, there will be some discontinuity in the solution because of the change in the mesh (ABAQUS/Standard, 2003). For the above-mentioned two composites (Figure 6.1 and Figure 6.2), the simulation has to be performed about twenty times in order to predict the effective stress-strain flow behaviour and the texture development. In this case, the accumulated error resulting from the solution mapping is difficult to estimate. Therefore, the elasto-viscoplastic material model[1] (without remeshing) is preferred to predict the mechanical behaviours of Fe-Cu composites.

6.3.2 Local Deformation Behaviour of the Grains

The overall elastoplastic behaviour of inhomogeneous materials, like Fe-Cu polycrystals, can be strongly influenced by very local events such as the initiation and the propagation of shear bands, recrystallisation processes, grain geometry and orientation. Studies on the grain-level interaction, the deformation and the orientation are carried out on polycrystals (typically containing a number of grains between 10 and 100) to understand the local deformation behaviour of individual grains, particularly, how their interactions cause a locally, highly heterogeneous plastic deformation. This is also the motivation of this section. Acharya and Beaudoin (2000) studied the grain-size dependent hardening in the fcc and the bcc polycrystalline metals at moderately high strains (2-30%). Sachtleber *et al.* (2002) investigated the effect of grain interaction and orientation on the plastic strain pattern for aluminum polycrystals by both experiments and FE simulations. By using Al-Mg-Si sheets as model material, Raabe *et al.* (2003) performed a study on the grain-scale micromechanics of polycrystal surfaces during the plastic straining in order to understand the relationship between the microstrain heterogeneity and the surface roughness.

Different initial orientations, which are randomly generated, are assigned to the iron and copper grains for the simulations in (a) and (b) of Figure 6.5 and Figure 6.6. We take the distance of the orientation space of the crystal orientation from

[1]In this work, this material model is the default one if there is no other specification.

its initial one as the misorientation. Initially, there is no misorientation inside each grain, but it exists between two arbitrary grains.

The rotation of the small harder phase particle b in Figure 6.5(a) is strongly influenced by the grain orientations. The particle c (Figure 6.5(a)) shows the effect of the grain orientation on the displacement of the particle. The above-mentioned influence and the effect are caused not only by the orientation of the particle itself but also by those of its neighbouring grains and particles. The alteration of the initial grain orientation modifies the local deformation which affects the material flow. Since the Fe17-Cu83 composite has a large amount of the softer phase which flows around the harder phase, small particles, like b and c which locate on such material flow ways, behave quite differently for the change of the grain orientation. Furthermore, the grain geometry is another factor which also affects the local deformation behaviour. Generally, the deformation behaviour of the grain or the particle with a large size varies less than small ones due to different grain orientations. In large grains, some parts, which are slender and near grain boundaries, are more sensitive to the change of the crystallographic orientation than other parts, e.g., particles a in Figure 6.5(a). The (microstructure) cut-out of the Fe50-Cu50 composite includes large harder phase particles, e.g., particle a, b, c, and d in Figure 6.6(a). These particles are on the four corners of the cut-out and they (particles and 2D cut-out) share many boundaries with each other. This special particle distribution makes such Fe phase grains even harder, since many boundaries of the aforementiond four grains (particle a, b, c, and d in Figure 6.6(a)) are confined by homogeneous boundary conditions during the deformation process. Both small and large particles (Figure 6.6(a) and (b)) behave like the aforementioned ones (Figure 6.5(a) and (b)), i.e., the sensitivity to the change of the grain orientation.

6.3.3 Local Plastic Deformation and Misorientation

Besides the grain orientation which influences the plastic deformation of the grains in polycrystals, the grain morphology and the phase arrangement also affect the pattern of deformation or the strain distribution of the material structure. Such microstructure should be representatively large enough in order to show some important indications for the plasticity, e.g., shear band, (Soppa *et al.*, 1998).

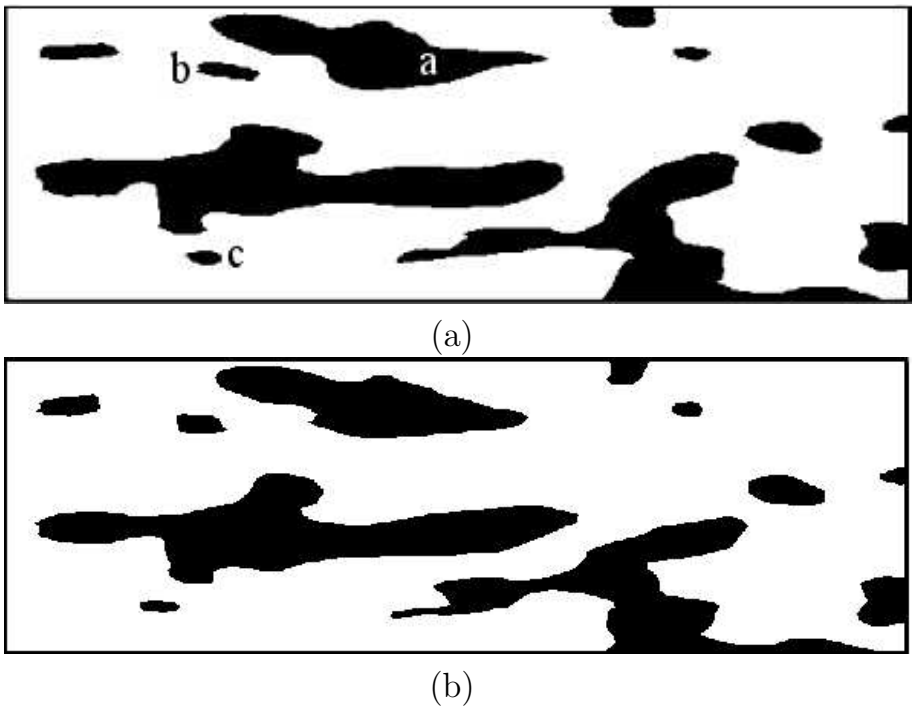

(a)

(b)

Figure 6.5: The influence of the initial orientation of grains (black: iron phase, white: copper phase) on the particle deformation at ε_p=90% for the Fe17-Cu83 composite (letters a to c in (a) indicate iron particles).

The strain rate (traceless part $\|\boldsymbol{D}'\|$) is plotted in Figure 6.7 for the Fe50-Cu50 composite at the plastic strain ε_p=90%, where lines show four major shear bands numbered from 1 to 4. These shear bands surround the largest grain Cu_a (referenced to Figure 6.2(c) in section 6.2) of the softer phase and stop at the boundaries of harder (Fe) phase particles a, b, c, d (referenced to Figure 6.6(a) in section 6.3.2). This pattern of the shear band distribution keeps its form for different initial grain orientations. Shear bands 2 and 4 appear very early. The shear band 3 forms at about $\varepsilon_p = 30\%$. The shear band 1 appears after the band 3. During the loading process, there are also some secondary short shear bands which disappear at high plastic strains. A shear band depends also on the crystallographic orientation of grains since it does not always follow a continuous straight line. Such phenomenon is also observed in Al-0.5wt%Mg polycrystals (Zhang and Tong, 2004). The large grain Cu_a plastically deforms more near the boundary than inside the grain. The plastic deformation of the grain Cu_a is quantitatively analysed by the histogram 6.8. The extremely deformed part which corresponds to the value of $\|\boldsymbol{D}'\| > 1.7^{-3}s^{-1}$ localises in the black region of the shear band 2 in Figure 6.7. Since the mean value of the misorientation for grain Cu_a is increasing

(a)

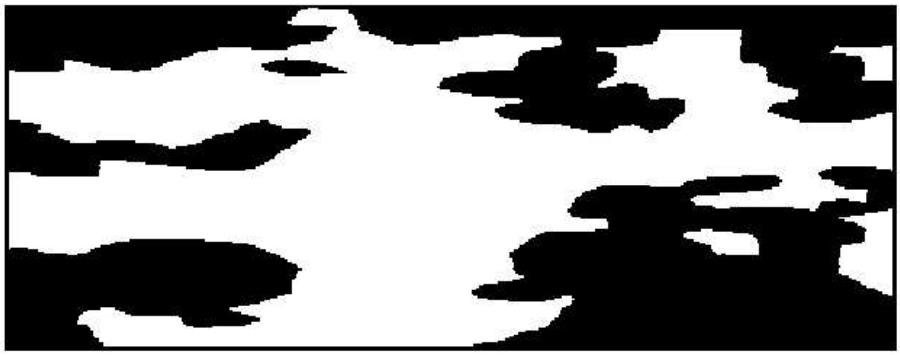

(b)

Figure 6.6: The influence of the initial orientation of grains (black: iron phase, white: copper phase) on the particle deformation at ε_p=90% for the Fe50-Cu50 composite (letter a to e in (a) indicate iron particles).

(Figure 6.9), the anisotropy of the distribution of the lattice rotation within Cu_a is also amplified according to the macroscopic plastic strain. In the experiment (analysed region of the specimen $\approx 250 \times 200$ μm), Tatschl and Kolednik (2003) observed the same property that strong heterogeneities in the in-plane strain and in the local lattice rotation exist within a single grain of copper polycrystals under tension.

Figure 6.10 (left column) displays the distribution of the misorientation for the iron and the copper phases of the Fe17-Cu83 composite. The iron phase shows a lower mean value of the misorientation than the copper phase (Fe: ≈15, Cu: ≈17). But the oscillation of the misorientation distribution is much larger for the iron phase than for the copper phase. The geometry and the distribution of the harder phase particles could be one of the reasons for such distribution. Compared to

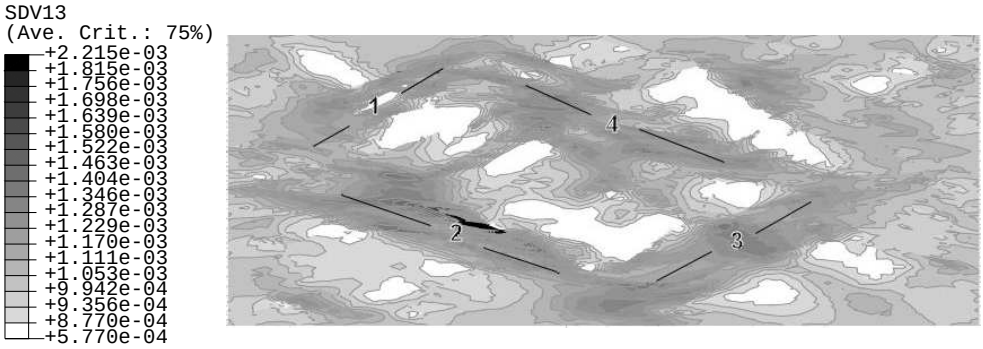

Figure 6.7: The strain rate (traceless part $\|\boldsymbol{D'}\|$) distribution with shear bands shown by lines at ε_p=90% for the Fe50-Cu50 composite.

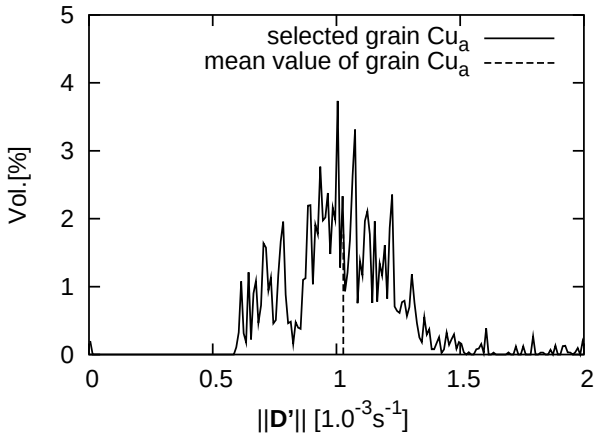

Figure 6.8: Histogram of the strain rate (traceless part $\|\boldsymbol{D'}\|$) distribution at ε_p=90% for grain "Cu_a".

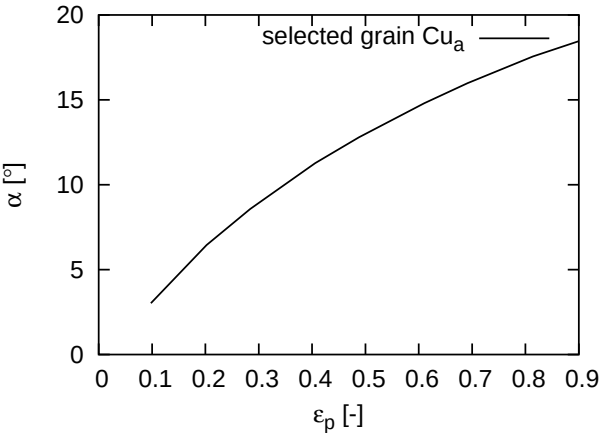

Figure 6.9: The mean value of the misorientation ($\alpha = \angle(\boldsymbol{Q}_t, \boldsymbol{Q}_0)$) for the grain "$Cu_a$" of the Fe50-Cu50 composite until the plastic strain ε_p=90%.

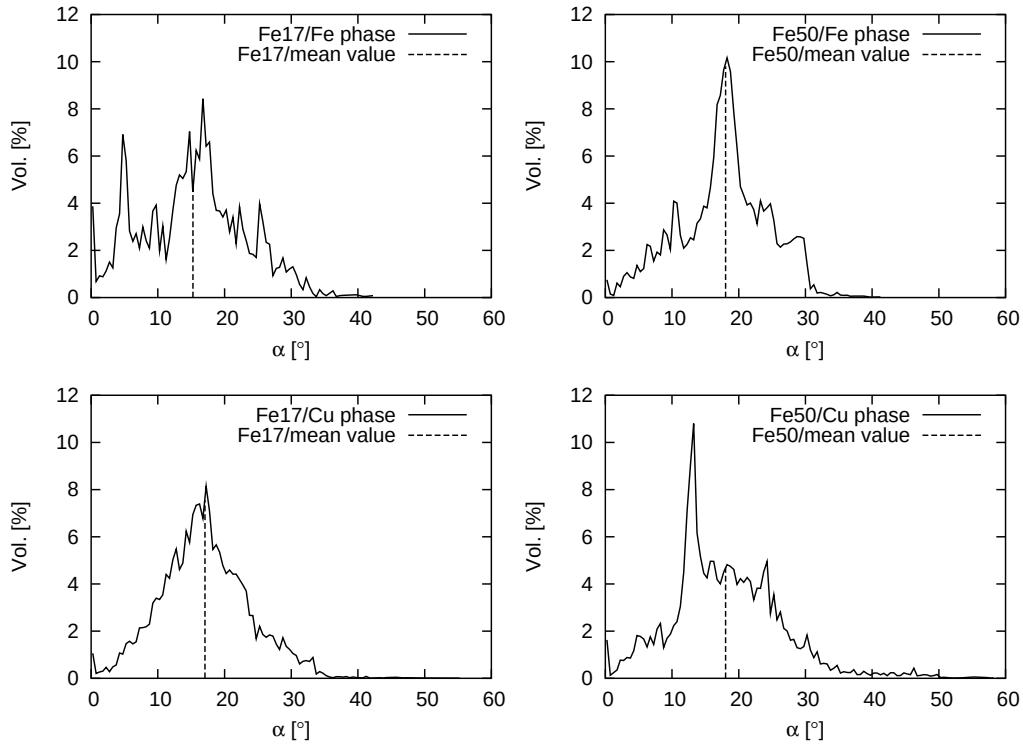

Figure 6.10: Histograph of the misorientation ($\alpha = \angle(\boldsymbol{Q}_t, \boldsymbol{Q}_0)$) distribution of the Fe and the Cu phase at ε_p=90% for Fe17-Cu83 (left column) and Fe50-Cu50 composite (right column).

the particles partly confined by boundary conditions and inside regions of large particles, the rotations are very likely much larger for small particles embedded in the Cu phase and for regions near grain boundaries. The distribution of the misorientation of both the iron and the copper phase of the Fe50-Cu50 composite (Figure 6.10 (right column)) is not so smooth as that of the copper phase of the Fe17-Cu83 composite. This means that the interaction between phases and the four strong shear bands (Figure 6.7) results in a high heterogeneity of the lattice rotation. The mean value for both the iron and the copper phases of the Fe50-Cu50 (Figure 6.10) is higher than those of the Fe17-Cu83 composite. There is no big difference for the misorientation mean value between the iron and the copper phases for Fe50-Cu50. This proves that interactions among phases and grains enhance a non-uniform distribution of the misorientations, in particular for the iron phase.

6.4 Crystallographic Texture and Effective Flow Behaviour under Simple Compression

6.4.1 Modification of the Hardening Rule

The stress-strain curve predicted by the axisymmetric FE model does not match the experimental one well (Figure 6.11), even though the input material parameters (Table 5.4 in section 5.1.2) are identical to those for the Taylor simulation which presents good stress-strain curves compared to those of the experiment (Figure 5.5). This result is reasonable since the Taylor model usually leads to a stiffer behaviour than the FE model for materials with cubic symmetry. To achieve better $\sigma - \varepsilon$ curves predicted by FE simulations, one can use FE simulations to identify the input material parameters by trial-and-error, and apply such parameters in other FE simulations. This is unacceptable due to the cost of the time. The major problem, which causes the misfit of the $\sigma - \varepsilon$ curve (Figure 6.11), is the hardening rate at $\varepsilon_p > 40\%$. The simulated $\sigma - \varepsilon$ curve (Figure 6.11) indicates a slower hardening rate than the reality when the plastic strain ε_p is between 40% and 60%, and is nearly converged at $\varepsilon_p > 60\%$ while the experimental curve hardens until ε_p =90%. By recalling the hardening rule (equation (3.52)), it is obvious that the hardening rate is lower if τ^C is nearer to τ_c^v. Therefore, an extra term is necessary in the hardening rule in order to describe the hardening behaviour observed in experiments.

As indicated in Figure 6.12, the relation between stress τ^C and strain γ can be written as (Kocks and Mecking, 2003) :

$$
\begin{aligned}
\tau^C(\gamma) &= \tau_\infty^C - (\tau_\infty^C - \tau_0^C)\exp(-\frac{\Theta_0}{\tau_\infty^C - \tau_0^C}\gamma) + \Theta_\infty\gamma \\
&\text{with :} \\
\tau_0^C &= \lim_{\gamma\to 0}\tau^C(\gamma) \qquad \tau_\infty^C = \lim_{\gamma\to\infty}\tau^C(\gamma), \\
\Theta_0 &= \lim_{\gamma\to 0}\frac{\mathrm{d}\tau^C}{\mathrm{d}\gamma} \qquad \Theta_\infty = \lim_{\gamma\to\infty}\frac{\mathrm{d}\tau^C}{\mathrm{d}\gamma},
\end{aligned}
\tag{6.1}
$$

or equivalently,

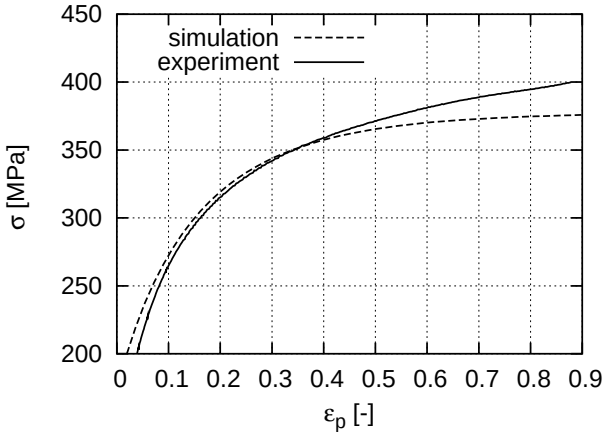

Figure 6.11: Stress-strain curves of the simulation and the experiment for the Fe17-Cu83 composite until ε_p=90% under a simple compression load.

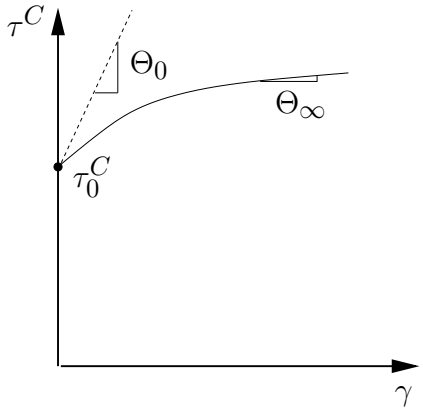

Figure 6.12: A sketch of the stress-strain curve to present the hardening rate coefficient Θ_0 and Θ_∞ in equation 6.1.

$$\begin{aligned} &\tau^C(\gamma) = a + b\gamma + c(1 - \exp(-d\gamma)) \\ &\text{with :} \\ &a = \tau_0^C, \quad b = \Theta_\infty, \quad c = \tau_\infty^C - \tau_0^C \quad \text{and} \quad d = \frac{\Theta_0}{\tau_\infty^C - \tau_0^C}. \end{aligned} \tag{6.2}$$

The input material parameters in equation (6.2) can be deduced from Table (5.4) (Section 5.1.2). In this work, the ratio Θ_∞:Θ_0 is taken as 1:50. When $\dot{\tau}^C = 0$, then $\frac{\tau^C}{\tau_c^v}$=1. It follows that $\tau_c^v = \tau_\infty^C = \tau_{c0}^v |\frac{\dot{\gamma}}{\dot{\gamma}_0^*}|^{\frac{1}{n}}$. For clarity, Table 6.2 indicates the input parameters mentioned in Equation (6.1) or (6.2).

Material	$a = \tau_C^0$(MPa)	$b = \Theta_\infty$	$c = \tau_\infty - \tau_0$	$d = \frac{\Theta_0}{\tau_\infty^C - \tau_0^C}$
Fe(vol.%)/Cu (vol.%)	Fe/Cu	Fe/Cu	Fe/Cu	Fe/Cu
Cu100	-/70	-/6.60	-/86.86	-/3.80
Fe100	187 /-	15.00/-	78.00/-	9.60/-
Fe17-Cu83	180/70	15.60/6.6	66.00/100.00	11.80/3.30
Fe33-Cu67	180/80	16.00/9.32	38.89/90.24	20.57/5.16
Fe50-Cu50	186/80	16.60/9.80	59.00/87.85	14.06/5.57
Fe67-Cu33	186/80	17.20/8.60	66.32/87.2	12.97/4.93
Fe83-Cu17	186/80	17.80/9.00	66.62/90.24	13.38/4.90

Table 6.2: Material parameters for the Fe, the Cu and their composites.

6.4.2 Effective Flow Behaviour

If the morphology of the material structure is fixed, and the other conditions, e.g., loading and boundary conditions, also do not change in the simulation, the microscopic stress-strain behaviour will be modified by the anisotropy of the grain orientation distribution. Thus, the macroscopic flow stress indicates the deviation among the simulations with different initial grain orientations. Therefore, the number of local grain orientations should be large enough to predict $\sigma - \varepsilon$ curves which are comparable with the experimental ones. In Figure 6.13, the $\sigma - \varepsilon$ curve is averaged over 18 calculations with different initial grain orientations for the Fe17-Cu83 composite. Since the volume fraction of the Fe phase is about 22% (as mentioned in Section 6.2) in the axisymmetric simulation, it should be reasonable that the simulated $\sigma - \varepsilon$ curve is between those of the Fe33-Cu67 and the Fe17-Cu83 composite (Figure 6.13). In this sense, the axisymmetric (FE) simulation captures the flow behaviour of the Fe17-Cu83 composite.

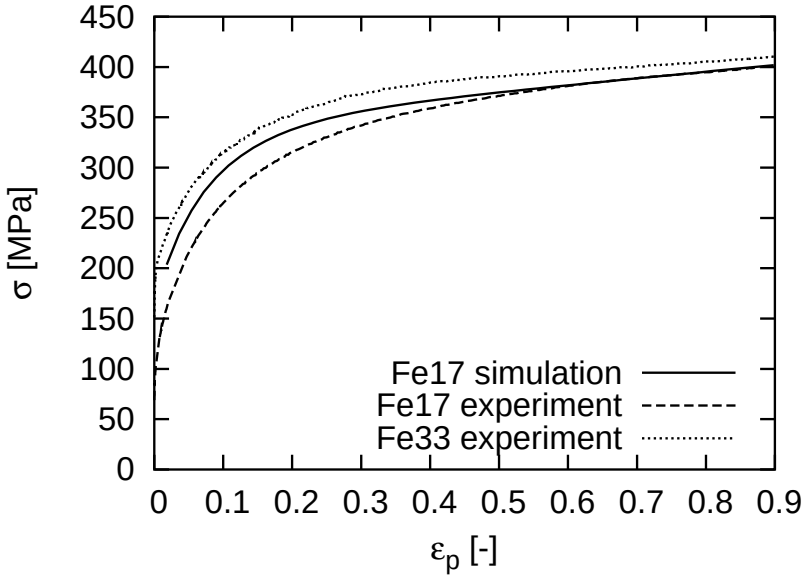

Figure 6.13: Stress-strain curves of the simulation (averaged from 18 calculations with different initial grain orientations, Fe17-Cu83) and experiments (Fe17-Cu83, Fe33-Cu67) until ε_p=90% under the simple compression load.

Figure 6.14 compares $\sigma - \varepsilon$ curves of the experiment and the FE prediction, in which the numerical result is the average over 22 simulations with different initial grain orientations. For the Fe50-Cu50 case, the simulated curve also matches experimental one well. For the experiment, the hardening rate is nearly constant

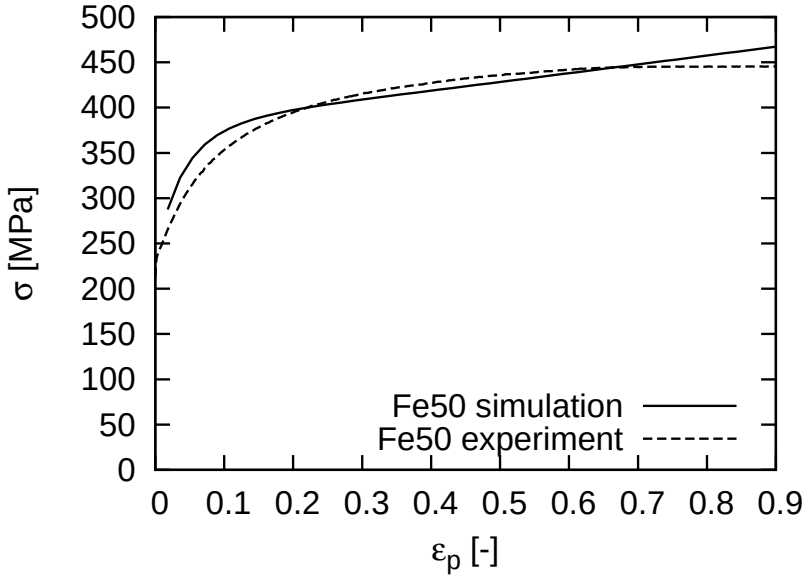

Figure 6.14: Stress-strain curves of the simulation (averaged from 22 calculations with different initial grain orientations) and the experiment for the Fe50-Cu50 composite until ε_p=90% under the simple compression load.

at approximately ε_p<62% and it decreases in the range of 62%<ε_p<70%. After that, the $\sigma - \varepsilon$ curve converges. These hardening behaviours are special for the Fe50-Cu50 composite, which means that such observations are not shown in other composites. The corresponding microscopic mechanisms for the above-mentioned phenomena may be that the relatively large amount of slip systems (from both the iron and the copper phase) are activated between 62%<ε_p<70% to accommodate the local geometrical requirement. As a result, the hardening rate is (approximately) the same. Beyond this deformation range, the stress converges at the macroscopic strain ε_p>70%. The local mechanism (in 62%<ε_p<90% of the Fe50-Cu50 composite) may also be related to the extra soft texture of Fe/Cu phases among all the composites. At a large plastic strain, the material hardens nearly linearly since the term $b\gamma$ (equation 6.2) is the major part for the hardening in the simulation. A more complicated ansatz for the hardening rule is necessary to predict better stress-strain behaviour for Fe50-Cu50. This is not done in the present work since the simulated result fits the reality already well enough (Figure 6.14) and, on the other hand, this special hardening behaviour is only observed in the Fe50-Cu50 composite among mentioned seven samples (pure iron, pure copper and 5 Fe-Cu composites) in this work.

In order to show the influence of the initial grain orientation on the flow behaviour,

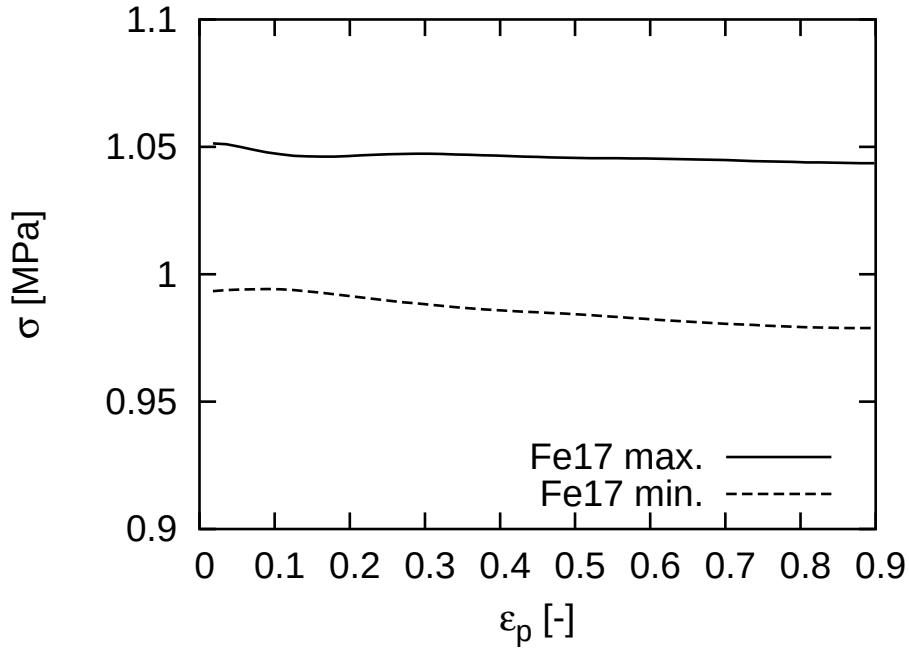

Figure 6.15: Minimum and maximum stress-strain curves among 18 simulations for the Fe17-Cu83 composite where the stress is normalised by the averaged stress (numerical $\sigma - \varepsilon$ curve in Figure 6.13).

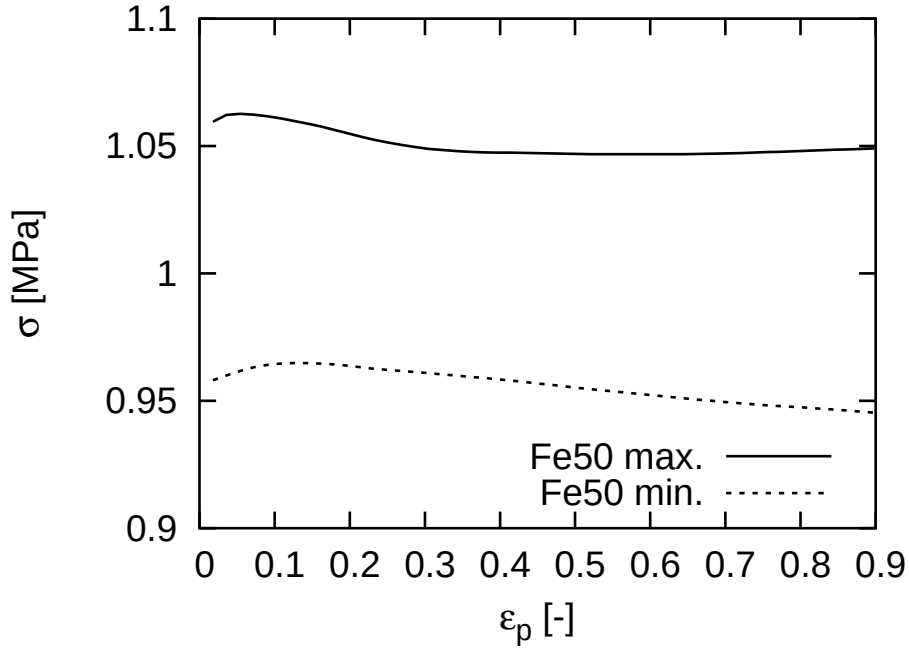

Figure 6.16: Minimum and maximum stress-strain curves among 22 simulations for the Fe50-Cu50 composite where the stress is normalised by the averaged stress (numerical $\sigma - \varepsilon$ curve in Figure 6.14).

Figure 6.15 and 6.16 present the normalized $\sigma - \varepsilon$ curves which are obtained by

$$\begin{aligned} \sigma_N(t) &= \frac{\sigma_{max/min}(t)}{\sigma_{aver}(t)} \\ \sigma_{aver}(t) &= \frac{\sum_{i=1}^{n} \sigma_i}{n}(t) \end{aligned} \tag{6.3}$$

with n=18 for the Fe17-Cu83 and n=22 for the Fe50-Cu50 composite. σ_{max} and σ_{min} are given by the simulated stress-strain curves which locate at highest and lowest position among all the simulations, correspondingly. The averaged stress is calculated from equation (6.3b) which also presents the way to get the simulated stress-strain curves in Figure 6.13 and Figure 6.14. The deviation from the averaged stress-strain curve is about 1% to 2% for the minimum stress-strain curve (dashed line in Figure 6.15) of the Fe17-Cu83 composite while it is about 5% for the maximum case. This 5% deviation remains true also for both "maximum" and "minimum" stress-strain curves for the Fe50-Cu50 composite (Figure 6.16). Therefore, different orientation distributions of grains may cause 5% fluctuation for the local stress-strain curves in the case that the microstructures contain relatively small number of grains[1].

Fe-Cu composites exhibit a greater stiffness than copper and a better ductility than iron. The reason for the former property is that the softer phase transfers the load to the harder phase. Figures 6.17 and 6.18 study the stress flow in each phase for the Fe17-Cu83 and the Fe50-Cu50 composite, respectively. σ_{phase} and σ present the stress for the Fe or Cu phase and the total stress of the composite, where both stresses are the averaged value from 3 simulations. One $\sigma - \varepsilon$ curve is nearest to the averaged $(\sigma - \varepsilon)$ curve among 18 (Fe17-Cu83) and 22 (Fe50-Cu50) calculations. The other two simulations predict the largest, and the smallest stress for a given strain, respectively. At the beginning of the yielding, the strength of the iron phase decreases rapidly, and that of the copper phase exhibits the reverse effect for both composites (Figure 6.17 and 6.18), where a smaller volume fraction of the iron/copper phase indicates the higher rate of this decrement/increment for this phase. This trend diminishes with the increasing of the plastic strain. Finally, the normalized stress in both phases converges to a certain value which

[1] According to Cheong and Busso (2006), such number of grains is between 10 to 100.

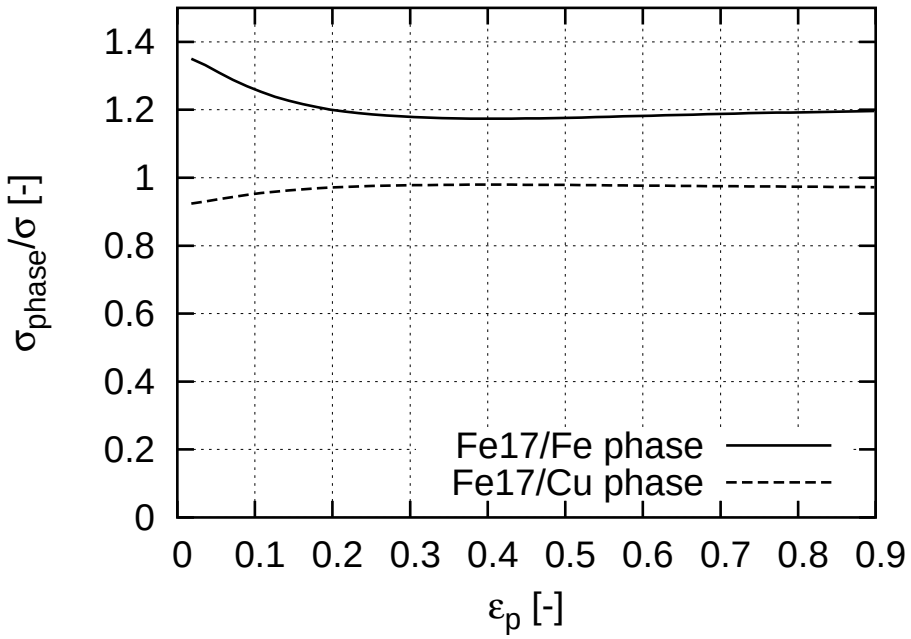

Figure 6.17: Normalised stress-strain curves of Fe and Cu phases for the Fe17-Cu83 composite until the plastic strain ε=90%.

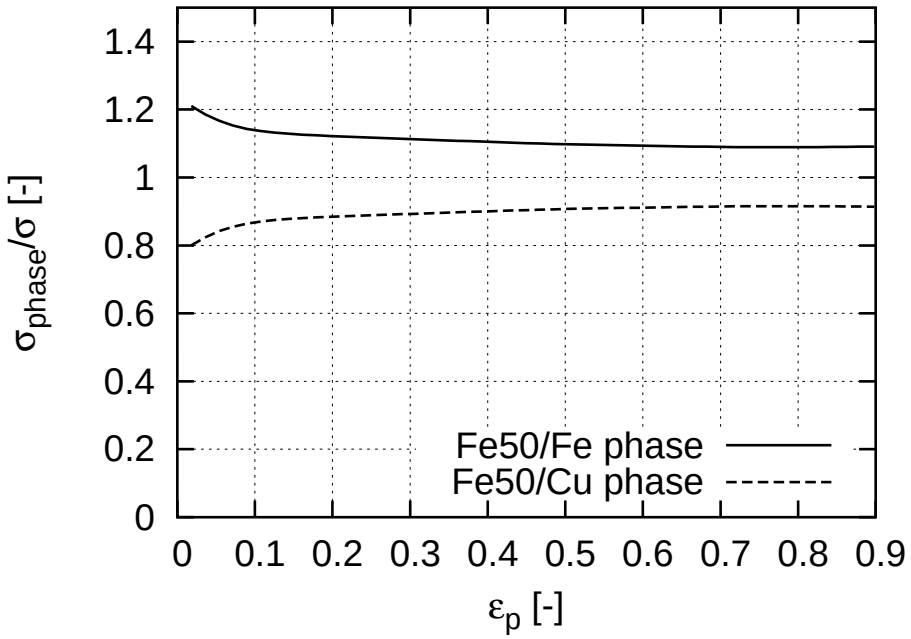

Figure 6.18: Normalised stress-strain curves of Fe and Cu phases for the Fe50-Cu50 composite until the plastic strain ε=90%.

varies according to the ratio of the Fe:Cu phase volume fractions. Based on the FE axisymmetric simulation, Li and Schmauder (2000) studied the relationship among the phase-stress partition in metal matrix composites, the reinforcement volume fraction and the geometry, the matrix hardening behaviour, and the applied strain level.

6.4.3 Crystallographic Texture

The iron-phase texture, presented as the standard inverse pole figure[1], is indicated in Figure 6.19 for both simulations and experiments at the 90% plastic strain. Such a texture is characterised by the fibre type texture (<100>- and <111>-fibere) which is well captured by the simulations for both the Fe17-Cu83 and the Fe50-Cu50 composite. Predictions of FE axisymmetric simulations also grasp the difference of the fibre intensity due to the phase volume variation, even though the maximum value of the fiber intensity is higher than that of the experiment. Since each inverse pole figure[2] includes more than 600 orientations which are initially randomly assigned to each grain, the effect of the local grain orientation on the texture can be neglected. Therefore, the local interaction and the phase arrangement are two major factors influencing the texture evolution. Due to the limited number of grains in both considered real microstructures, the possibility is approximately the same for interactions between Fe and Cu grains for the Fe17-Cu83 and the Fe50-Cu50 composite. Thus, the aforementioned first reason (interaction) is not essential for the analysis of the texture shown in Figure 6.19. The analysing type (axisymmetric model) and the restricted confinement (homogeneous boundary conditions, especially for a limited real microstructure) should be the reasons for the sharper textures in the simulation than real ones. The particle distribution contributes to the denser fibre-intensity of Fe50-Cu50 than that of Fe17-Cu83, while it leads to the even stiffer material structure in which four large iron particles (a, b, c, and d in Figure 6.6) are on boundaries.

The simulated and experimental texture of the copper phase is given in Figure

[1]In the following, the standard inverse pole figure will be called the inverse pole figure. Some detailed information concerning the calculation of the inverse pole figure is given in Appendix B.

[2]Inverse pole figures are obtained from 18 and 22 calculations for the Fe17-Cu83 and the Fe50-Cu50 composite, respectively.

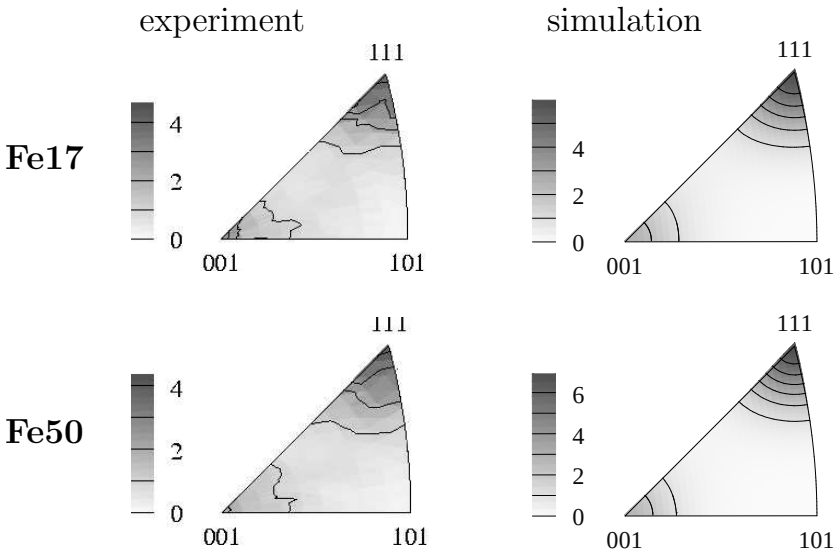

Figure 6.19: Texture (inverse pole figure) of Fe phases from axisymmetric FE simulations and experiments at ε_p=90% for the Fe17-Cu83 and the Fe50-Cu50 composite.

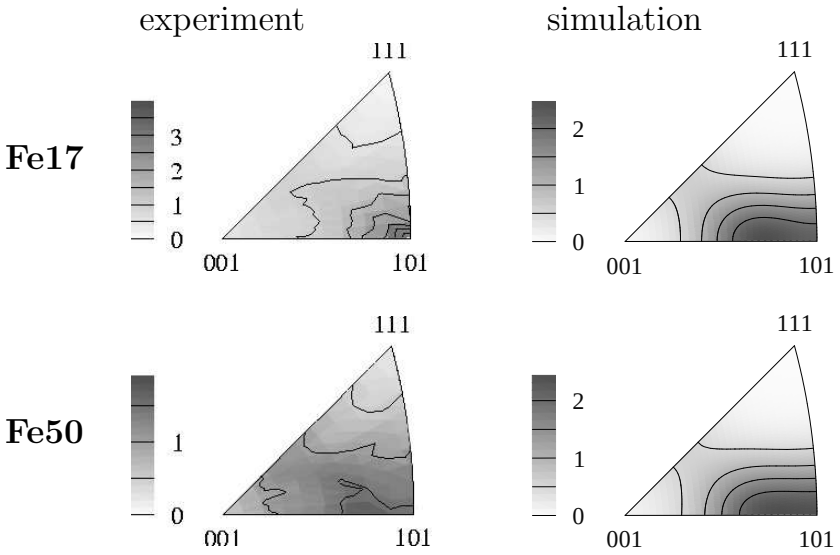

Figure 6.20: Texture (inverse pole figure) of Cu phases from axisymmetric FE simulations and experiments at ε_p=90% for the Fe17-Cu83 and the Fe50-Cu50 composite.

6.20 for the Fe17-Cu83 and the Fe50-Cu50 composite. The pronounced <110>-fibre smears in the <210> direction and develops in the <411> direction (for the position of the <210> and the <411> fibre see Figure B.2 in appendix B), especially in the simulated textures. A rather soft texture of the Cu phase is presented by the measurement for the Fe50-Cu50 composite, which is not well simulated by the FE model. Except for above-mentioned reasons, i.e., the local interaction, the limited material structure, and boundary conditions, the present model is probably not able to catch the local change of the activation of slip systems fast enough due to the isotropic hardening assumption.

6.5 Strain Distribution under Uniaxial Tension

If the polycrystalline structure is under load, the anisotropy of the constituent grains results in high heterogeneities of the stress and strain on the grain level. In order to reveal the deformation process and the plastic strain field of polycrystals on the microlevel, many experiments, FE simulations and theoretical models are investigated. Allais *et al.* (1994) described an (experimental) technique to study the local strain field over a domain representative of the microstructure of the two-phase (e.g., iron/silver and iron/copper) polycrystals. The strain map is also plotted to give qualitative information on the strain-localisation modes. Sachtleber *et al.* (2002) experimentally and numerically introduced the spatial distribution of the accumulated plastic surface strain for aluminum polycrystals which were plastically compressed in a channel die. Through combining the experimental data of the local in-plane strain and the local crystal orientation, Tatschl and Kolednik (2003) estimated slip systems that are locally activated at arbitrary positions within a grain by a simple kinematic model. Harder (1999) developed a crystallographic model to investigate the local deformation processes. In this section, the local strain distribution of the iron and the copper phases is investigated by the FE axisymmetric model considering the real microstructure (Figure 6.1) for the Fe17-Cu83 composite at a tensile plastic strain ε_p=19.8%. Since the slight difference of the size of the copper phase and the production process are not the influential factors for the local strain field and the production process of samples is not considered in the simulation, the microstructure of the Fe17-Cu83 composite in Figure 6.1 is applied for the simulation for the simplicity. Some quantitative

analysis is also presented for the mean value of the plastic strain in each phase.

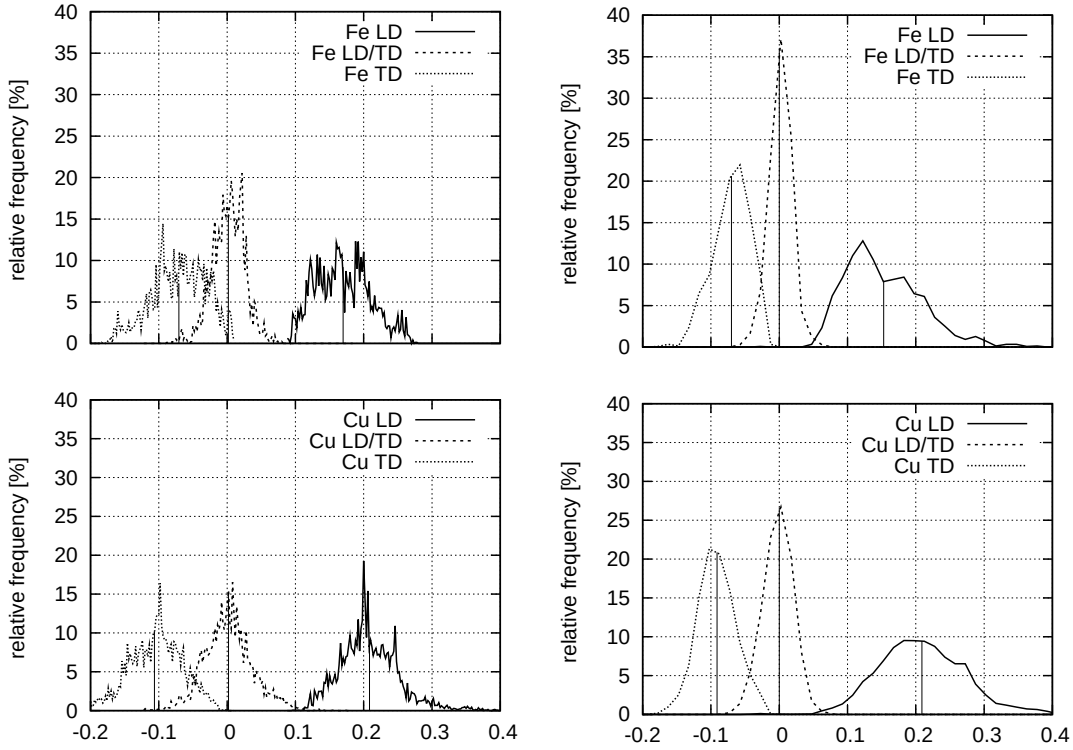

Figure 6.21: Strain field distribution of Fe and Cu phases of axisymmetric FE simulations (left column) and experiments (right column) for the Fe17-Cu83 composite under the tensile loading until ε_p=19.8%.

Figure 6.21 presents the distribution of the local plastic strain for the iron and the copper phases in the simulation (left column) and the experiment (right column), where LD, TD, and LD/TD indicate the loading, the transverse, and the shear direction, respectively.

Both the distribution and the mean value of the plastic strain match the reality well for the iron phase in all the three directions. The strain of the iron phase behaves more heterogeneously in the loading direction (LD) than in the shear direction (LD/TD) due to the wider range and the larger oscillation of the distribution curve in the LD direction, while this nonhomogeneity lies in the middle for the transverse direction (TD). An obvious higher concentration of the strain shows in the LD/TD than that of the LD and the TD directions. The mean value of the plastic strain is ε_{LD}^{Fe}=16.99% in the loading direction for the simulation and ε_{LD}^{Fe}=15.3% for the experiment. Both these two values are much smaller than the mean value of the composite (ε_{LD}^{Fe+Cu}=19.80%). They are ε_{TD}^{Fe}=-7.1% and ε_{TD}^{Fe}=-

7.0% for the transverse direction in the numerical and the experimental prediction, correspondingly. There is only small deviation (of the strain mean value from the total one) for the shear direction. Generally, the (absolute) mean value of the plastic strain for the harder phase is less than that of the whole composite, which corresponds to the general conclusion in the two-phase polycrystal plasticity that the harder phase takes less deformation than the softer one.

For the copper phase, the experiment (lower right in Figure 6.21) clearly presents a wider range of the strain distribution in the loading direction than in the other two directions, i.e., more inhomogeneity in the LD direction. This property is well predicted by the numerical simulation (lower left in Figure 6.21). In the loading direction, the numerical curve even captures the second peak shown at approximately ε_{LD}^{Cu}=27% in the experiment. The mean value of the copper-phase plastic strain is ε_{LD}^{Cu}=20.8% in the simulation and ε_{LD}^{Cu}=20.9% in the experiment. The corresponding results for the TD direction are ε_{TD}^{Cu}=-10.6% for the FE prediction and ε_{TD}^{Cu}=-9.1% for the reality, respectively. Like in the iron phase, this value is still approximately zero for the shear direction. Contrary to the harder phase, the copper phase burdens more plastic deformation, which is indicated from the fact that the mean value of the plastic strain for the Cu phase is higher than that of the total composite.

Chapter 7

Three-Dimensional Finite Element Simulations

7.1 Introduction

In this chapter, the three-dimensional FE model is applied to simulate the crystallographic texture, the stress in each phase, and the local strain. In particular, inverse pole figures of the iron and the copper phases (pure iron/copper and five Fe-Cu composites) are numerically predicted to systematically study the texture evolution due to the phase volume variation, the type change of the inclusion-matrix and the possibility of Fe-Cu phase interactions. The texture evolution according to the change of the volume ratio of Fe:Cu phase is not predicted in detail by the axisymmetric simulation. A material model which can predict well the numerical results statistically requires a number of elements large enough for the material structure, realistic boundary conditions and a microstructure which can well present the real local morphology. A larger material structure with more grains allows for a larger amount of local interactions which is very important for the micro-mechanical behaviour of two-phase materials, like Fe-Cu composites. Due to the systematic errors in the boundary layer of the RVE for the homogeneous boundary condition (Bertram, 2005), the periodic boundary conditions are applied in all the 3D FE simulations with the regular mesh and the Poisson Voronoi tessellation. Compared to axisymmetric models with a small number of iron and copper grains and the HBC, 3D models with more grains (500-1500) and PBC should give even better results.

7.2 Artificial Microstructure and Periodicity

7.2.1 Artificial Microstructure: Poisson Voronoi Mosaics

To evaluate microstructural influences on material properties, it is important to statistically estimate the mean grain size, the grain size distribution and geometrical characteristics. Such geometrical characteristics can give quantitative insight into the effects of the processing parameters (Ohser and Mücklich, 2000). Since the iron and the copper powders have an identical shape geometry in the experiments, the artificial microstructure can be presented by the same type of cells (or grains) for both phases. It is a reasonable assumption that grains are randomly distributed. A random microstructure can be approximately presented by the Voronoi algorithm. For models shown in this chapter, the grain structure is given as Voronoi tessellations (Ohser and Mücklich, 2000) in three dimensions where the points are generated from a Poisson process. In the 3D case, such Voronoi tessellation partitions the Euclidean spaces ($\mathfrak{E}$) into sets ($\mathbb{S}_i$) with non-overlapping interior, which means $\mathfrak{E} = \cup\mathbb{S}_i$ (Andersson, 2005). Let $\{\boldsymbol{p}_i\}$ be a set of points, which are randomly generated and called generator points (Ohser and Mücklich, 2000). Each point in this set generates a cell (or grain) S_i. A certain grain S_i consists of all points which have $\boldsymbol{p}_i$ as their nearest generator point in $\mathfrak{E}$, i.e., if $\boldsymbol{p}_i \neq \boldsymbol{p}_j$

$$\mathbb{S}_i = \{\boldsymbol{x} \in \mathfrak{E} : \|\boldsymbol{p}_i - \boldsymbol{x}\| \leq \|\boldsymbol{p}_j - \boldsymbol{x}\|, \forall \boldsymbol{p}_j\}, \tag{7.1}$$

where $\|\cdot\|$ indicates the distance between two points in $\mathfrak{E}$. For a Poisson Voronoi cell, the number of points is finite in the set $\{\boldsymbol{p}_i\}$, and such generator points are prescribed in a control volume.

Figure 7.1 shows spatial (3D) Voronoi tessellations with respect to a Poisson field. Periodic cells are applied in our 3D FE models. Firstly, generator points are created within a cube. These points are uniformly distributed (Poisson distribution). Secondly, the periodicity is obtained by copying the generator points in the horizontal, vertical and third directions. Finally, there are totally 3^3=27 such point sets (cubes) for the periodic cell in the 3D space. A unique periodic cell is taken from the centre of the above-created Voronoi structure.

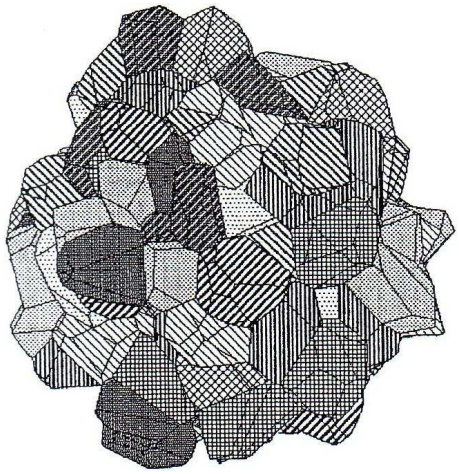

Figure 7.1: Computer simulations of spatial Poisson Voronoi tessellations (Ohser and Mücklich, 2000).

7.2.2 Periodic Boundary Conditions

We consider the RVE and assume that $\bar{\boldsymbol{F}}$ is the mean deformation. For a periodic cell, the boundary condition can be expressed as

$$\boldsymbol{u}^k = (\bar{\boldsymbol{F}} - \boldsymbol{I})\boldsymbol{x}^k + \boldsymbol{w}^k, \tag{7.2}$$

where $\boldsymbol{u}^k$ and $\boldsymbol{x}^k$ present the displacement and position vectors for a given node k, correspondingly. $\boldsymbol{w}^k$ in equation (7.2) denotes the fluctuation of node k. We prescribe the part $(\bar{\boldsymbol{F}} - \boldsymbol{I})\boldsymbol{x}^k$ in equation (7.2). The fluctuation is permitted on the boundaries and set to be equal on the opposite boundaries $\overset{+}{A}$ and $\overset{-}{A}$, i.e.

$$\boldsymbol{w}^\alpha|\,\overset{+}{A} = \boldsymbol{w}^\beta|\,\overset{-}{A}. \tag{7.3}$$

α and β in equation (7.3) denote equivalent boundary nodes according to the periodicity condition. In addition, the stress field is assumed to be equilibrated on opposite boudaries. This can be denoted as

$$\boldsymbol{t}^\alpha|\,\overset{+}{A} = -\boldsymbol{t}^\beta|\,\overset{-}{A}. \tag{7.4}$$

The periodic boundary condition is implemented by the above-mentioned condition (equation (7.2)) with the aid of the finite element method. The requirement of such calculations is a periodic mesh, which means, for a node on an edge, there

is at least one exact equivalent point on the opposite edge of the cell. For simplicity, a regular mesh is preferred for Poisson Voronoi micromechanical models, the element number of which is 25^3 or 36^3. Figure 7.2 presents a model with regular mesh and periodic boundary conditions in the deformed state.

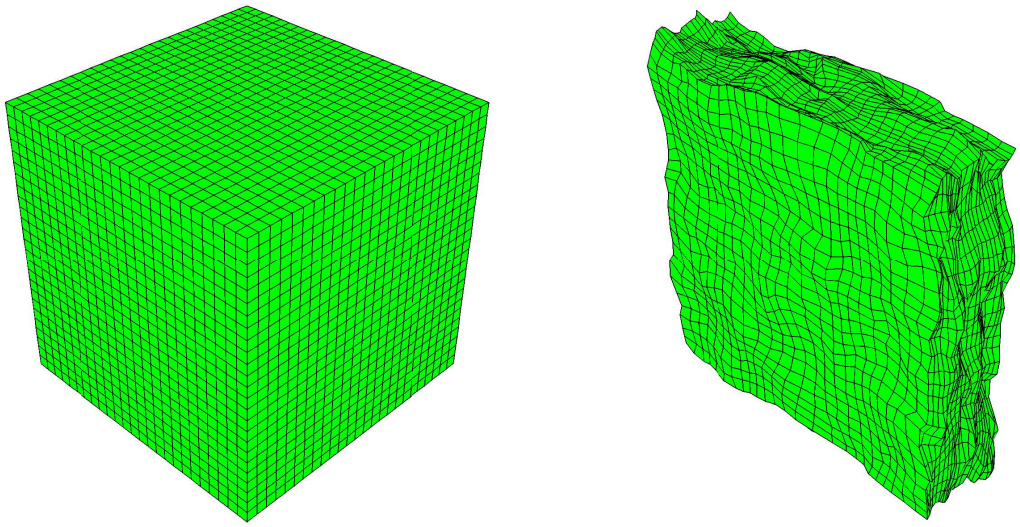

(a) (b)

Figure 7.2: Undeformed 3D finite element model with the regular mesh (a) and the periodic boundary condition in deformed state (b).

To simulate the micromechanical behaviour of two-phase ferrite/pearlitic steels, models based on the Voronoi algorithm and periodic boundary conditions are also applied by Nygards and Gudmundson (2002a) in the 2D case and Nygards and Gudmundson (2002b) in the 3D case.

7.3 Finite Element Simulations Based on a Regular Mesh

In the simulations, the hybrid element C3D8H is chosen as element type, because such elements are primarily intended for the usage with incompressible (or almost incompressible) material behaviour (ABAQUS/Standard, 2003). The number of averaged elements per grain is approximately taken as 30 (30×8=240 integration points). All the integration points inside one grain initially have an identical crystallographic orientation which varies from one grain to another. Since the suitable grain size is also important for the study of the mechanical material

behaviour, the information concerning the grain size is shown in Figure 7.3 for both the iron and the copper phases.

The assumption is made that each integration point presents the $1/x$ volume fraction of the total element which has x integration points. The data in Figure 7.3 are obtained from one calculation of the model with 25^3 elements for the Fe17-Cu83 and the Fe50-Cu50 composite, separately. Except for the copper phase of the Fe50-Cu50 composite, the ratio is between 2 to 15 for the volume fraction of most grains to that of the minimum one in each phase. Even though this ratio is between 5-25 for the copper phase of Fe50-Cu50, such grain size distribution is still suitable. In the experiment, the diameter of the input iron and copper powder is, mostly, between 10-50 μm, and the corresponding mean value is 20.5μm (iron) and 18.3μm (copper). The same distribution is detected for both the iron and the copper phases in the output material (Commentz, 2000). The above observations indicate that the volume ratio of grains considered in our microstructures is acceptable.

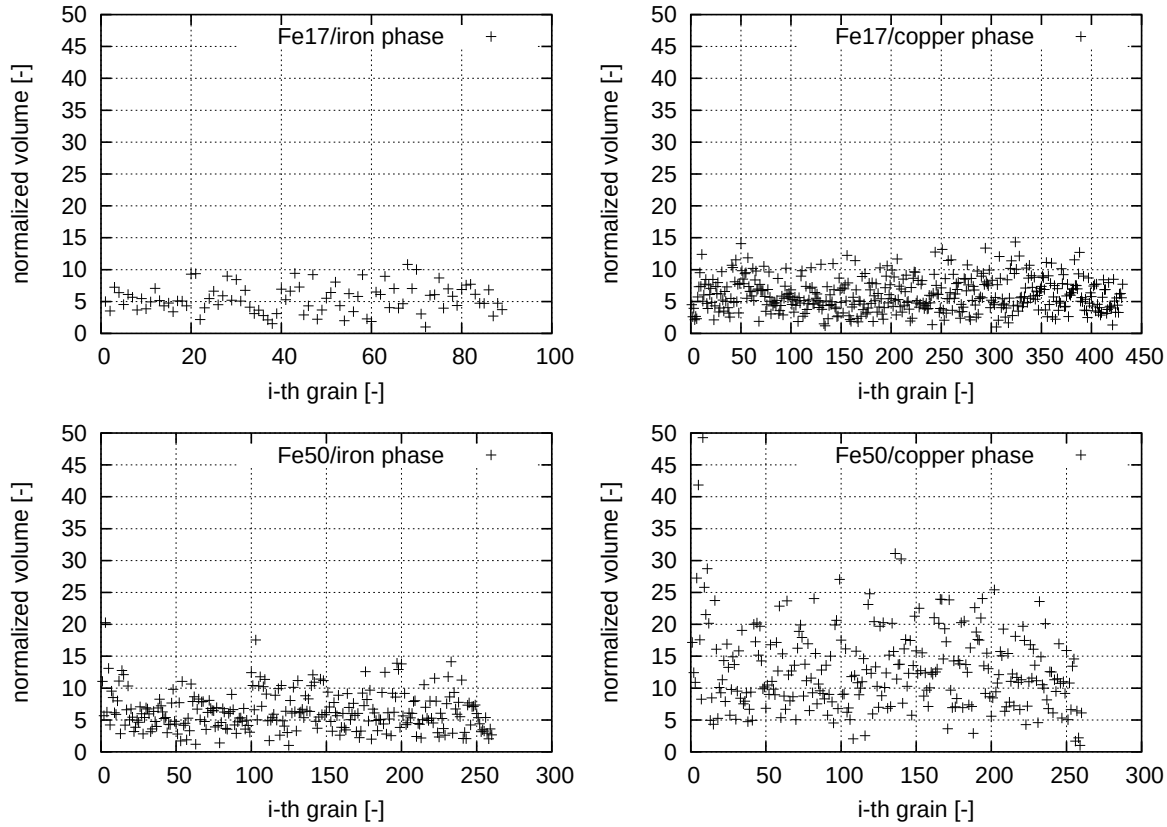

Figure 7.3: Grain size distribution of iron and copper phases for the Fe17-Cu83 (upper row) and Fe50-Cu50 composite (lower row), where the volume of each grain is normalized by the minimum one of the grains in each phase.

Since the grain number should be large enough to analyze the mechanical behaviour of the material, e.g., the flow behaviour and the texture evolution, the simulation is performed more than once for Fe-Cu composites, where a new morphology is applied for each calculation. Table 7.1 gives the information about the simulation of 3D models with 25^3 elements. The number of the initial orientations for the texture analysis is the same as that of the grains of each phase (Table 7.1), since the crystal orientations are initially identical inside the same grain. No identical orientations exist between any different grains. Based on experience, the data obtained from 440 different initial orientations (grains) should also give an accurate enough texture (copper phases of the Fe83-Cu17 composite in Table 7.1). The deviation is less than 1% for the volume fraction of the iron and the copper phase of each composite in the simulation. To be efficient in the simulation time and make the requirement of the hardware lower, models with 25^3 elements are preferred for most simulations, and those with 36^3 elements are applied to improve the texture prediction and to study the mean stresses of the iron and the copper phases.

Material	Grains		vol. (%)		Element type
	Fe	Cu	Fe	Cu	
Cu100	-	520	-	100	C3D8H
Fe100	520	-	100	-	C3D8H
Fe17-Cu83	445	2155	17.16	82.84	C3D8H
Fe33-Cu67	516	1044	32.44	67.56	C3D8H
Fe50-Cu50	520	520	49.27	50.73	C3D8H
Fe67-Cu33	1047	513	66.21	33.79	C3D8H
Fe83-Cu17	2160	440	83.01	16.99	C3D8H

Table 7.1: The number of grain orientations, the volume fraction of the iron and the copper phases, and the applied element type in models with 25^3 elements.

7.3.1 Flow Behaviour and Texture Evolution

Different grain geometries and orientations modify the local stress and the strain field. This influence can diminish to be a minor factor which affects the effective flow behaviour, if a large enough number of grains and grain orientations is considered. Each graph in Figure 7.4 includes the same number of grains as shown in Table 7.1, correspondingly.

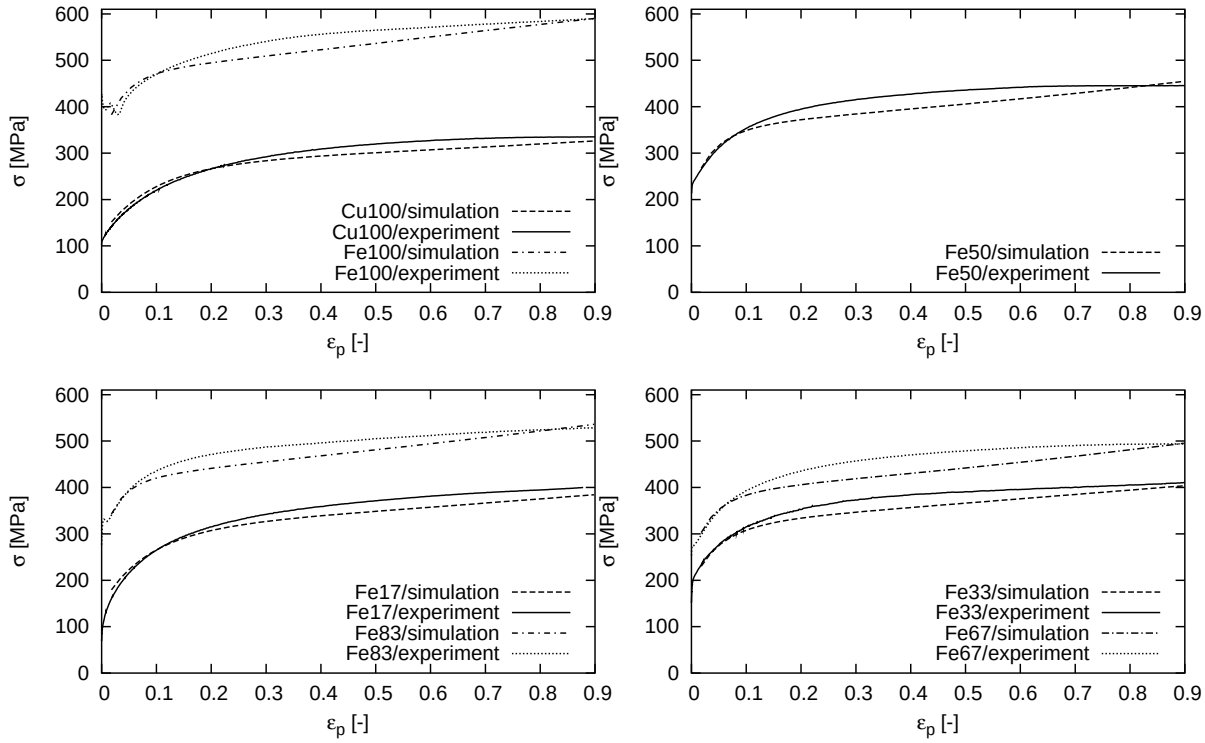

Figure 7.4: Simulated and experimental stress-strain ($\sigma - \varepsilon$) curves for pure iron, pure copper and their composites until 90% plastic strain.

All the simulated $\sigma - \varepsilon$ curves match the experimental ones well until about 10%-15% plastic strain. In the range of 80%-90% plastic strain, the prediction is also good. Among the seven polycrystalline materials mentioned, the flow behaviour of pure copper is captured at best. Due to the complex hardening process, which has not been well understood up to now, in the polycrystalline composites at large plastic strain, some deviation is shown in the range of 15%-80% plastic strain. Compared to the experimental $\sigma - \varepsilon$ curves, the calculated curve for the Fe67-Cu33 composite exhibits the largest deviation which is approximately 10%. The stress flow behaviour is underestimated to a certain extent (mostly less than 10%) by 3D FE models. Compared to the $\sigma - \varepsilon$ curves predicted by the axisymmetric model (Figure 6.14), the 3D FEM analysis predicts a softer material behaviour than the axisymmetric one for the same input parameters. There may be two reasons for this effect. Firstly, since more grains are considered in the microstructures of the 3D case, this leads to a larger amount of interactions between grains and phases on the microlevel, which causes a lower stress. Secondly, the axisymmetric

analysis generally gives stiffer material behaviour due to its special assumption (see section 6.2). Particularly in this work, homogeneous boundary conditions are also responsible for the higher stress predicted in the axisymmetric model.

The texture of the iron phase presented as the inverse pole figure is shown in Figure 7.5 for both the experimental (left column) and the simulation (right column) at the compressive plastic strain ε_p =90%. The measured textures are characterised by the following properties:

- Typical fibre textures are shown, which concentrate on the <100>- and the <111>-fibre.
- The pure iron polycrystal presents the sharpest texture; the presence of the second phase (Cu phase), even with a small amount of volume fraction (17% volume fraction), obviously reduces the sharpness of the texture.
- The effect of the volume fraction of the second phase (copper) on the texture evolution of the iron phase is obvious, if one compares textures among the Fe17-Cu83, the Fe33-Cu67, and the Fe50-Cu50 composites.
- The maximum intensity of the <111>-fibre is similar for composites with the same volume fraction of the inclusion, i.e., Fe83-Cu17 v.s. Fe17-Cu83 and Fe67-Cu33 v.s. Fe33-Cu67.
- Even though the interpenetrating network of iron-copper phases (Fe50-Cu50) has a much higher harder phase content than the Fe17-Cu83 composite, there is not much difference for the sharpness of the texture between the aforementioned two composites.

Since the numerical predictions capture all the above-mentioned experimental observations of the crystallographic texture, we conclude that the elasto-visco-plastic 3D model with Poisson Voronoi microstructures predicts quite well the textures for the harder phase of Fe-Cu polycrystals. Concerning the property in the fourth point, the simulated results are limited to the Fe67-Cu33 and the Fe33-Cu67 composites.

The maximum value of the <111>-fibre density is lower for the iron phase in the Fe17-Cu83 than in the Fe83-Cu17 composite in the simulation. It may result

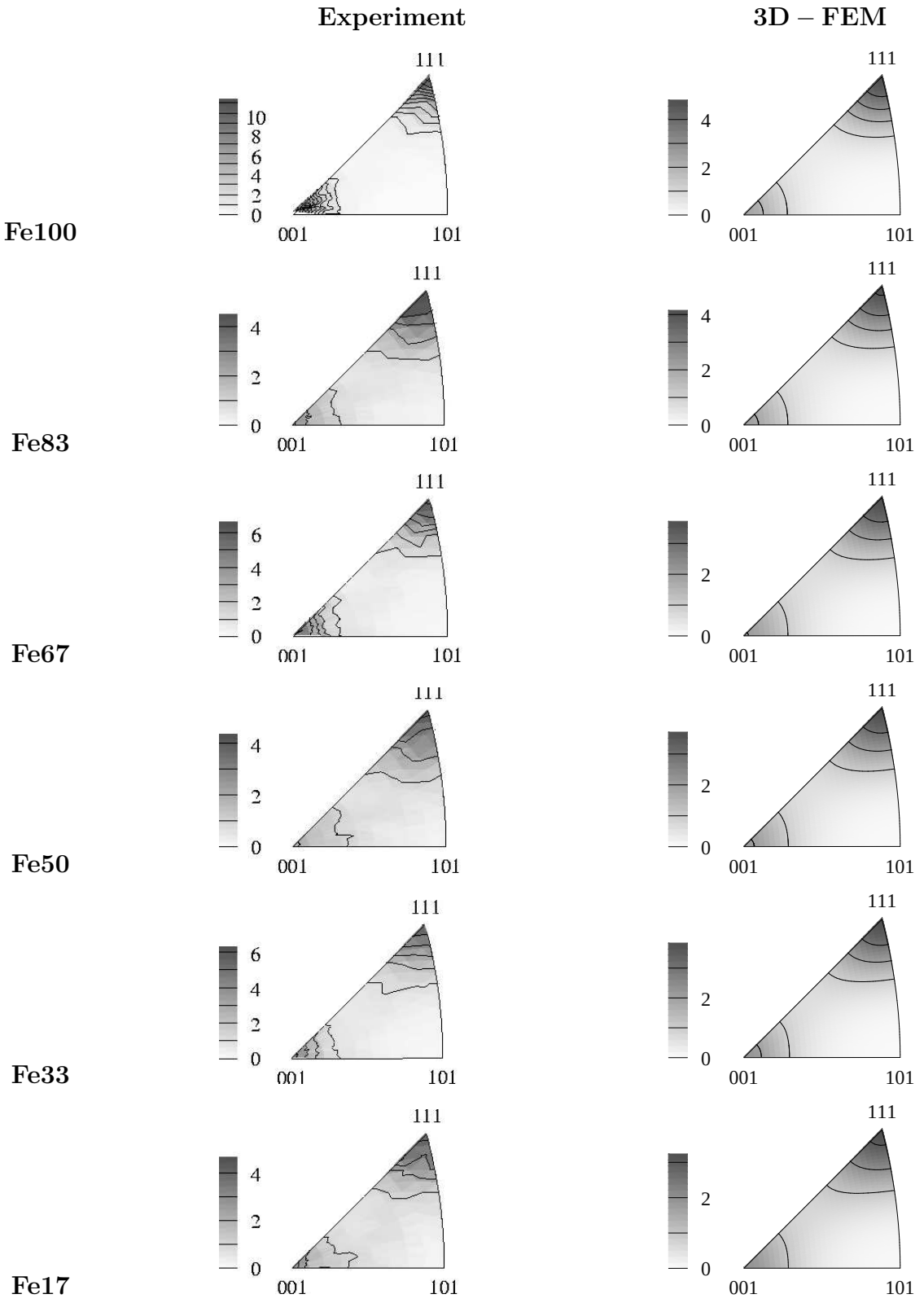

Figure 7.5: Comparison of inverse pole figures of the iron phase in normal direction between the experiment (left) and the 3D finite element simulation (right) under the compressive load at the 90% plastic strain.

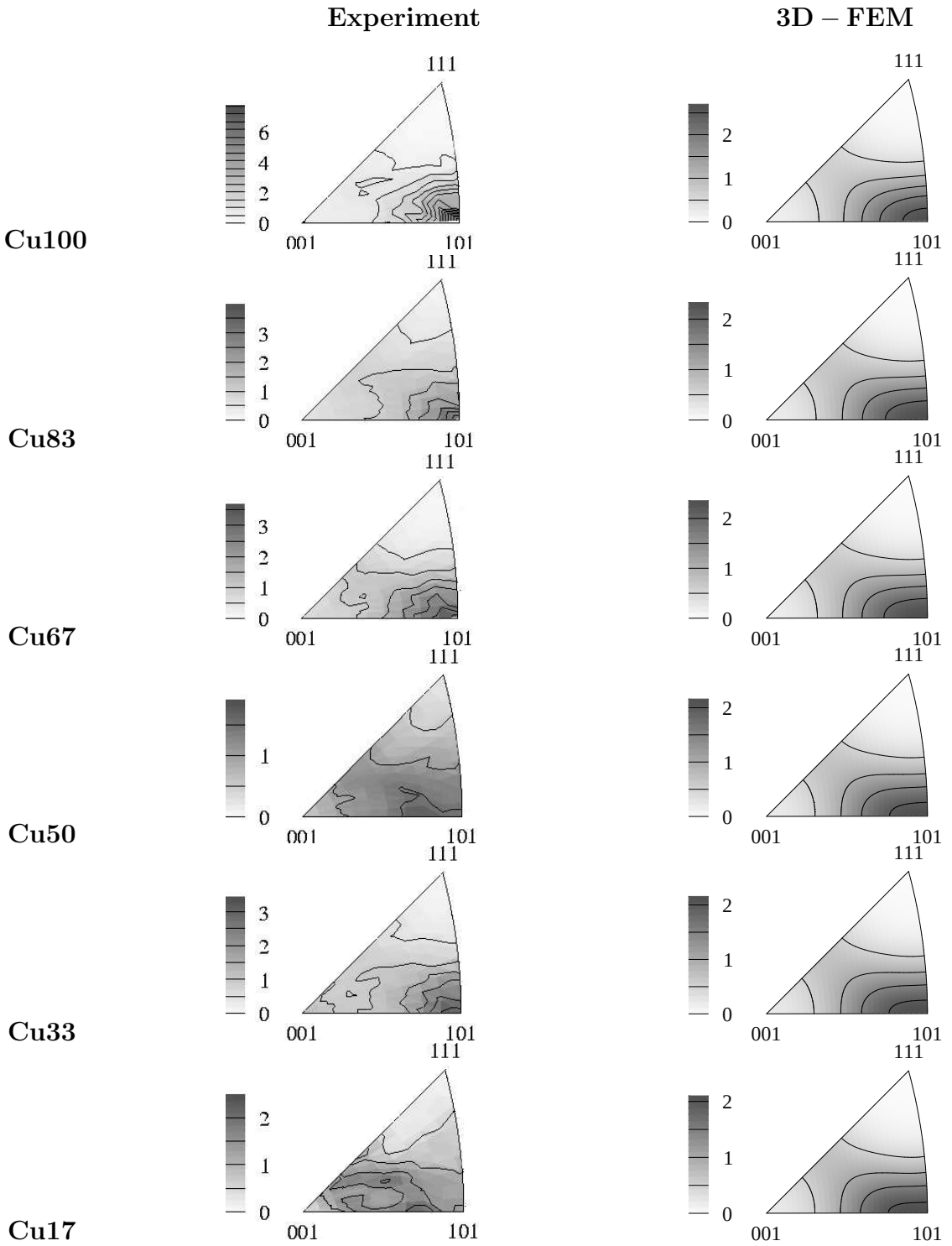

Figure 7.6: Comparison of inverse pole figures of the copper phase in normal direction between the experiment (left) and the 3D finite element simulation (right) under the simple compressive load at the 90% plastic strain.

from the consideration of bcc slip systems (in the calculation) during the hardening process which can be changed by the presence of the copper phase. Besides <111>{110} slip systems, other ones are also observed in the experiment. For the Fe83-Cu17 composite, this disadvantage in the model may be accumulatively large due to the high amount of the iron content. The above-mentioned points 4 and 5 indicate that the local interaction is essential for the texture evolution in the Fe-Cu composite, since the possibility for such interactions is the same for the Fe33-Cu67 and the Fe67-Cu33 (or for the Fe17-Cu83 and the Fe83-Cu17) composites. As mentioned in Section 2.1.1, the size of the input powders of iron and copper has approximately the same size distribution. During the composition, the solubility of the iron in the copper and vice versa is negligible. The Fe/Cu grain size and the size distribution are not changed by the production process. To a large extent, the distribution of the phase-area is in the same range for both phases. However, to fix the above conclusion (the strong influence of the interaction between phases on the texture), more experimental data is necessary, in particular, the distribution of the phase-area for composites with the same volume ratio of the inclusion to the matrix (e.g., Fe17-Cu83 v.s. Fe83-Cu17). Numerical predictions of the iron phase texture show less inflection of the radial width of the <100>- and the <111>-fibres than the experiment.

The texture of the copper phase is presented in Figure 7.6 for the Cu and Fe-Cu composites in the normal direction at 90% plastic strain under a simple compressive load. The measured texture of the copper phase has the following properties:

- The texture of the single-phase (pure) copper strongly concentrates in the <110>-fibre, which develops in the <210>- and the <411>-direction (fibre directions referenced to Figure B.2 in appendix B).
- The copper phase texture becomes much weaker by the presence of the second phase even with only 17% volume fraction, which is similar to the influence of copper on the texture of the iron phase.
- In reality, the maximum pole density and its position varies due to a different phase volume ratio among Fe-Cu two-phase polycrystals.

The above properties are well presented by 3D simulations. Predictions for the above third point capture how the maximum pole density changes according to the

increasing volume fraction of the second (iron) phase, even though the difference is not so big as that in the experiment. For the Fe83-Cu17 composite, the position of the maximum pole density is not predicted by the simulation (last row in Figure 7.6).

In order to give a clear view of the maximum fibre intensity for both phases, Figure 7.7 compares the (maximum) value of the <111>-fibre for the iron phase (upper) and the <110>-fibre for the copper phase (lower) among the mentioned five Fe-Cu composites at a plastic strain ε_p=90%. The grain number in the simulation for the corresponding composite is shown in Table 7.1. For the iron phase, the discussion is referenced to those (points 4 and 5) for Figure 7.5. In the case of the copper phase, the <110>-fibre intensity increases with its volume fraction in the experiment, where the interpenetrating network of Fe-Cu phases is excluded. These experimental measurements mean that the effect of the harder phase on the texture of the softer phase is larger than vice versa. This phenomenon is predicted by simulations, where the maximum intensity of <110>-fibre is approximately the same for the Fe67-Cu33 and the Fe83-Cu17 composite. The difference of the maximum intensities among composites is not so large as those in the experiment for both phases.

For the interpenetrating network of the Fe and Cu phases (Fe50-Cu50 composite) in the experiments, the <111>- and <110>fibre intensity is the lowest one among all the composites for both the iron and the copper phases, correspondingly. This proves that local interactions between iron and copper grains strongly influence the texture development in both phases, i.e. more interactions cause softer texture. The comparison of the aforementioned property is concentrated on the Fe33-Cu67 and the Fe50-Cu50 composite for the numerical results. The reasons for this choice are that, firstly, it is significant to predict that the texture of Fe-Cu polycrystals with less volume fraction of the harder phase gives a higher fibre intensity (maximum value). Secondly, the difference of the Fe-phase volume fraction is kept as small as possible for composites due to the above-mentioned imperfection (bcc slip systems) in the simulation. In numerical predictions, the lower fiber intensity is shown in the interpenetrating network (Fe50-Cu50) compared to the Fe33-Cu67 composite for both the iron and the copper phases (Figure 7.7). The difference of the maximum fibre intensity (the <111>-fibre for the iron phase and the <110>-fibre for the copper phase) between the Fe33-Cu67 and the

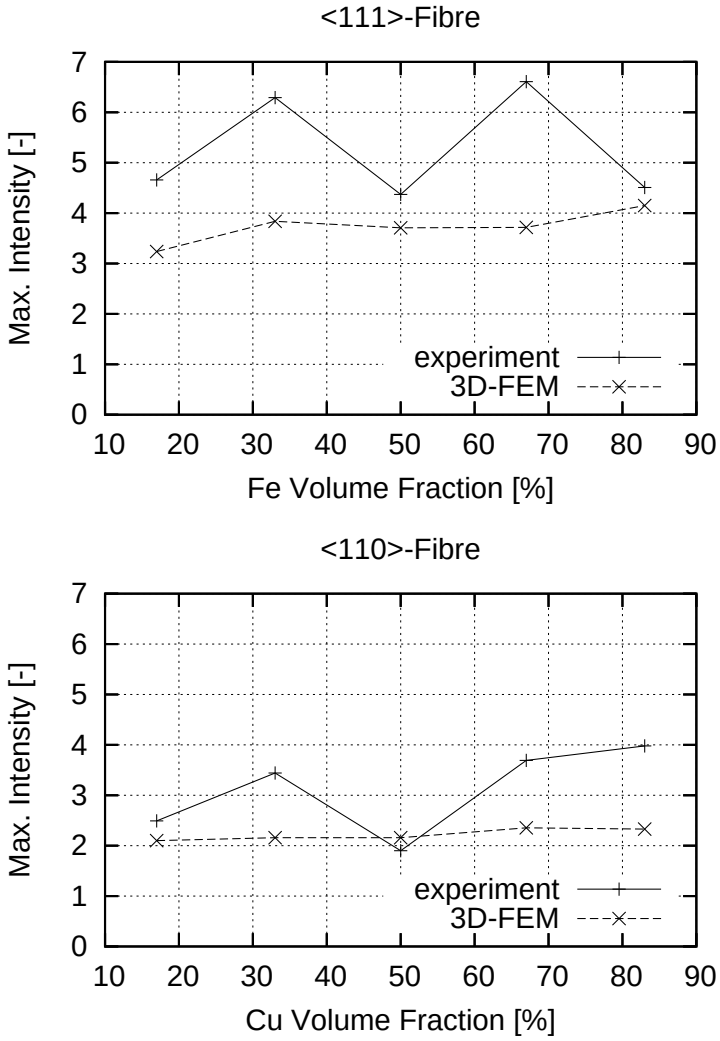

Figure 7.7: Comparison of the maximum intensity of the <111>-fibre for the iron phase (upper) and the <110>-fibre for the copper phase (lower) between the experiment and the 3D FE simulation with 25^3 elements under a compressive load at 90% plastic strain.

Fe50-Cu50 composite is not so big in the simulation as in the experiment. The numerical result would be more convincing if an improved model could enlarge the difference of the maximum fibre intensity. Based on the above discussion, there are two ways to improve the texture prediction, first, to enlarge the total number of grains (orientation) for the texture calculation or, second, enlarge the interaction possibilities for iron and copper grains in each simulation. The minimum number of initial grain orientations considered in these two composites is 516 (for the iron phase of the Fe33-Cu67 composite). The grain number is not the key point to improve the texture prediction. As a result, a model with larger elements (36^3 elements) is preferred, where 1550 grains are considered in the whole microstructure. Figure 7.8 compares the iron-phase texture among the experiment (left column), the simulation with 25^3 elements (middle column), and the simulation with 36^3 elements (right column), where the numerical calculation is performed only once for the model with 36^3 elements to predict the texture. An even better prediction is shown for the variation of the maximum <111>-fibre intensity between these two composites. Compared to numerical results obtained from 25^3 elements, the difference of the <110>-fibre intensity (copper phase in Figure 7.9) between these two composites becomes smaller for the model with 36^3 elements. Briefly, the model with 36^3 elements predicts a slightly better texture for the iron phase but no improvement for the copper phase. This means numerical results predicted by the model with 25^3 elements are already acceptable.

7.3.2 Stress Distribution

In two-phase polycrystalline materials, the harder phase acts as a strong stress concentrator during the deformation (Commentz *et al.*, 1999; Soppa *et al.*, 1998). The normalised stress of the iron and the copper phases is presented for the Fe33-Cu67, the Fe50-Cu50 and the Fe67-Cu33 composite in Figure 7.10 where σ_{phase} and σ indicate the stress of the iron phase or the copper phase, and the total stress of the corresponding composite. The calculation is performed only once by using the model with 36^3 elements.

We define σ_{phase}/σ as the normalized stress in each phase. The stress of the iron phase decreases quickly before 20% plastic strain while that of the copper phase behaves inversely. The rate of this decrease (Fe phase) is faster for a lower Fe phase

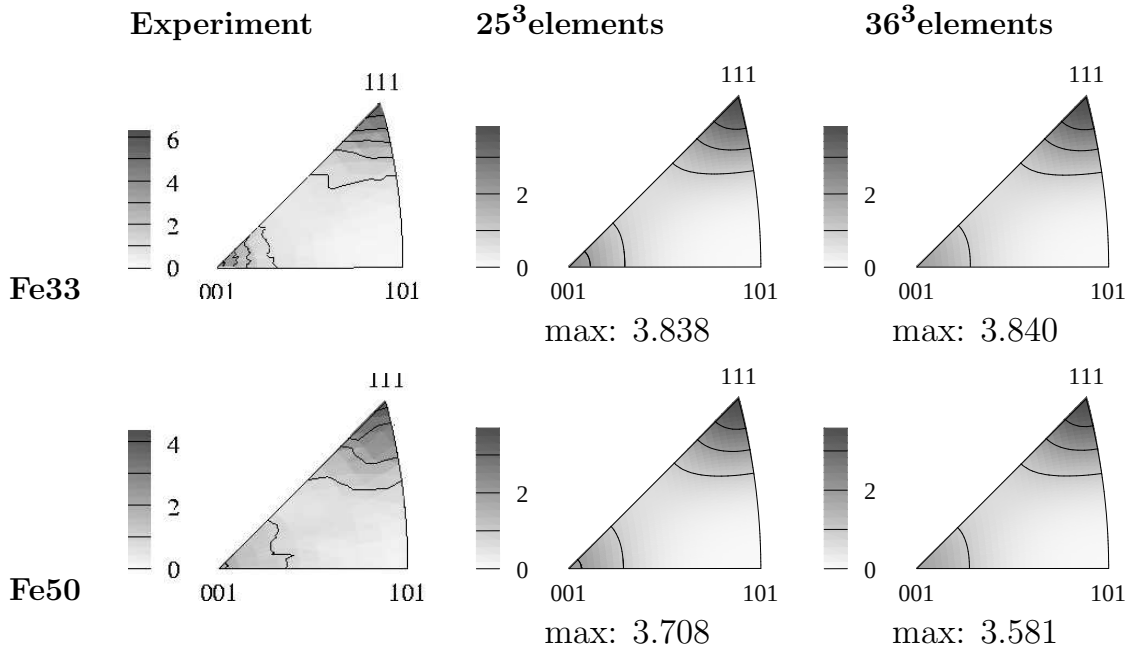

Figure 7.8: Comparison of the texture prediction for the iron phase between the experiment and numerical simulations under compressive load at 90% plastic strain (left column: experiment, middle column: FE model with 25^3 elements, right column: FE model with 36^3 elements, max: maximum intensity of the <111>-fibre).

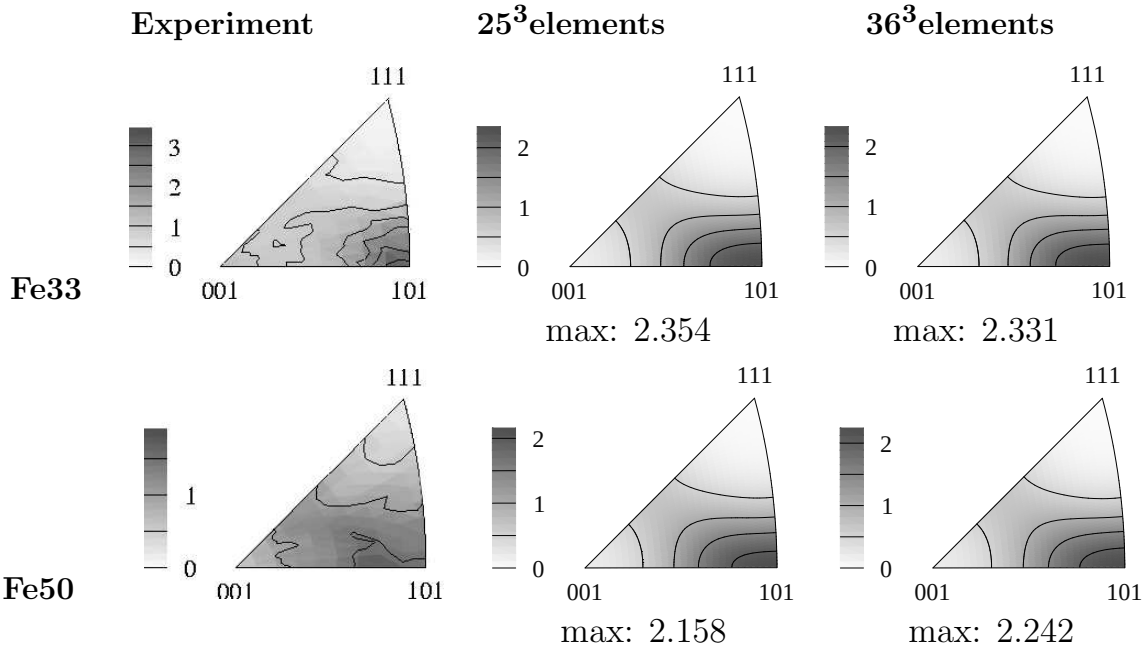

Figure 7.9: Comparison of the texture prediction for the copper phase between the experiment and numerical simulations under compressive load at 90% plastic strain (left column: experiment, middle column: FE model with 25^3 elements, right column: FE model with 36^3 elements, max: maximum intensity of the <110>-fibre).

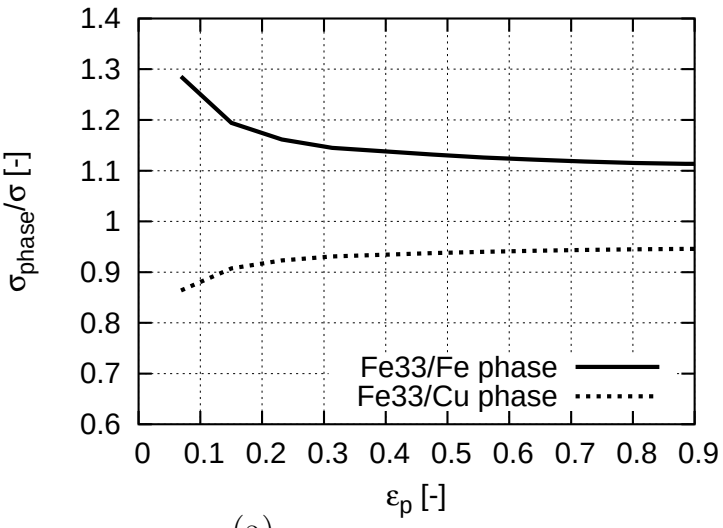

(a)

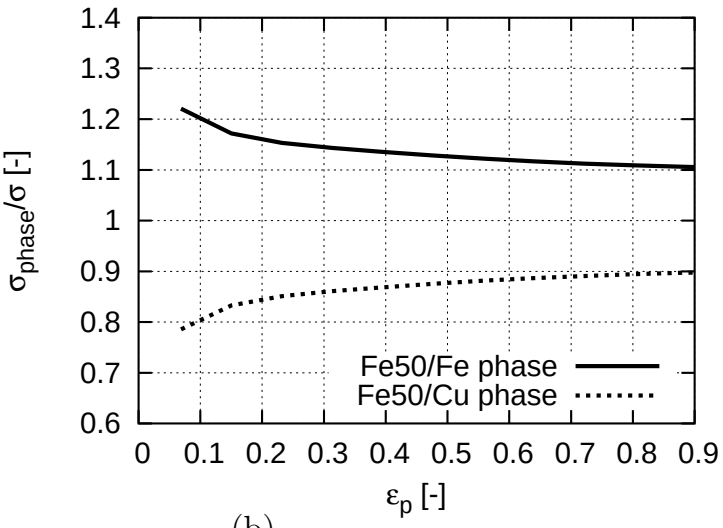

(b)

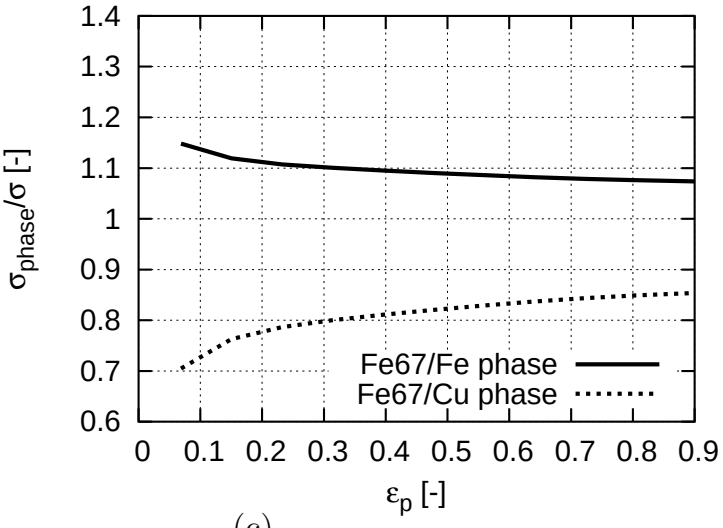

(c)

Figure 7.10: Normalised Fe and Cu phase stresses predicted by 3D finite element models with 36^3 elements for the Fe33-Cu67, the Fe50-Cu50, and the Fe67-Cu33 composite under compressive load until ε_p=90%.

content in composites. The speed of the increase (Cu phase) is slightly slower for a lower Fe phase content in composites. Such phenomenon shows that the local stress field is very sensitive to the plastic deformation at the early stage. The above observation is also shown in the axisymmetric simulation (Section 6.4.2). After such rapid change of stresses in both phases, the normalised stress-strain curves converge to certain values for both the iron and the copper phases. For the iron phase, this value is about 1.1 for all the three composites. The normalized stress-strain curves of the copper phase converge to different values. This value is higher for a lower Fe phase content in composites. Since the stress of the Fe phase converges to the same value for all the three composites but the stress of the Cu phase does not, we conclude that the effect of the iron phase on the copper phase is larger than vice versa. In the experiment (Commentz, 2000), it is observed that the iron phase starts to yield shortly after the beginning of the yielding of the composite. On the other hand, some iron phase is still in the elastic-plastic transition up to higher macroscopic strain (Commentz *et al.*, 1999). This means that the plastic deformation of the iron phase takes place step by step. If the harder phase yields, the load will be transferred back to the softer phase (Daymond *et al.*, 2005). As a result, the stress of the iron phase decreases while the stress of the copper phase presents the opposite effect with the increase of the plastic strain. Observations in the experiment proved that numerical results in Figure 7.10 are reasonable for the flow behaviour of the stress in each phase.

7.3.3 Strain Distribution

The material heterogeneity on the microscale can be studied by the non-uniform distribution of the strain field. Figure 7.11 presents the distribution of the local strain field for both the iron and the copper phase in the simulation (left column) and the experiment (right column) at the macroscopic tensile strain ε_p=19.8%. The grain number considered in numerical calculations is referenced to Table 7.1.

In reality (Figure 7.11) and as mentioned in Section 6.5, the distribution of the local strain field has a higher concentration in the shear direction (LD/TD) than in the other two directions (LD and TD) for both the iron and the copper phase, which means that more nonhomogeneity is shown in the loading (LD) and the transverse directions (TD). Besides, this distribution in the loading direction cov-

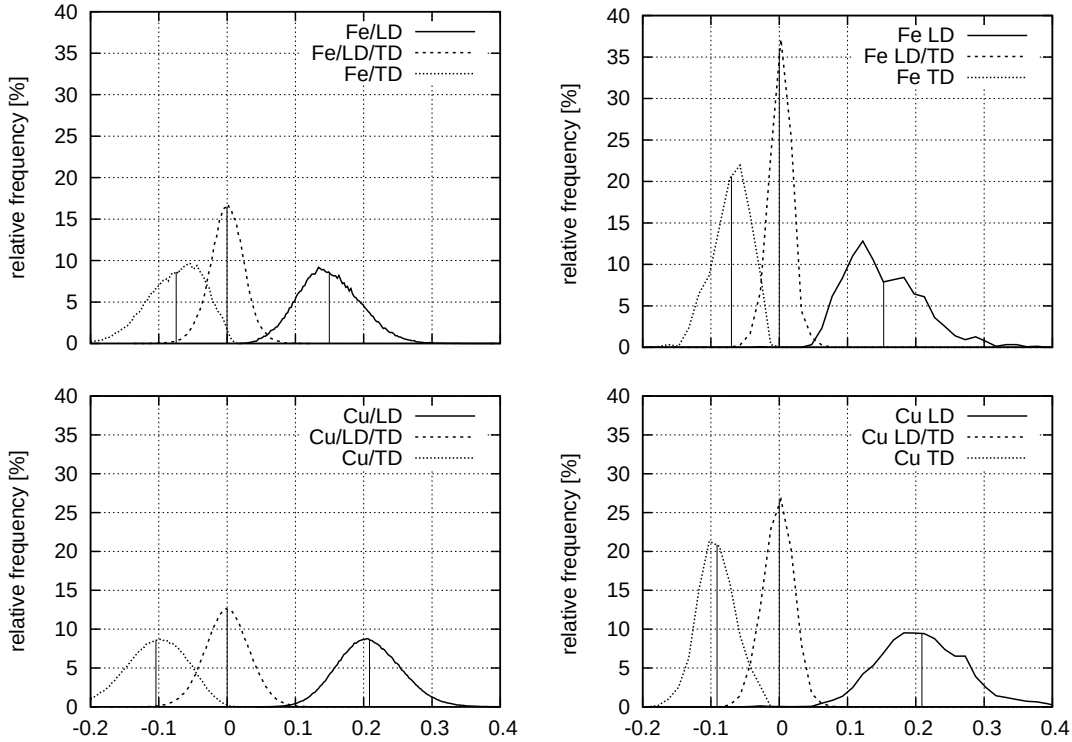

Figure 7.11: Strain field distribution of Fe (upper row) and Cu (lower row) phases of 3D FE simulations (left column) and experiments (right column) for Fe17-Cu83 composite under tensile loading at ε_p=19.8%.

ers the widest range among these three directions. This indicates that the material deforms more heterogeneously in the LD direction than in the TD direction. The numerical results predict all the above-mentioned properties well for both the harder and the softer phase. The simulations also capture how the Fe phase presents less heterogeneity than the Cu phase, especially in the shear direction. There are two indicators for the above conclusion for the comparison between the harder and the softer phases, i.e., the concentration of the distribution curves and the mean values of the local strain in each direction. The former can be obtained from the range of the distribution curve and the maximum (relative) frequency. Averaged values of local strains of the Fe and the Cu phase are exhibited in Table 7.2 for each direction, where a comparison is made between the simulation and the experiment.

For both the iron and the copper phases, the numerical results quantitatively predict the mean value of local strains (Table 7.2) well in all the three directions. The softer phase takes more plastic strains, since its averaged strain (absolute) value is much higher than the harder phase one in both the loading and the

transverse directions.

Direction	Fe phase		Cu phase	
	sim.	exp.	sim.	exp.
LD	0.150	0.153	0.209	0.209
TD	-0.075	-0.070	-0.104	-0.091
LD/TD	0.0	0.0	0.0	0.0

Table 7.2: Mean values of local strains in the loading (LD), the transverse (TD), and the shear (LD/TD) direction in simulations (sim.) and experiments (exp.) for Fe17-Cu83 composite at the tensile plastic strain ε_p=19.8%.

Chapter 8

Summary and Outlook

The aim of the present project is to understand the mechanical behaviour of Fe-Cu composites and, in particular, the coupling of the microscopic and the macroscopic deformation behaviour under large plastic deformations. Seven types of composites have been investigated. These polycrystalline composites are produced from spherical iron and copper powders by powder metallurgy (Hartig and Mecking, 2005). The crystallographic texture, the stress, and the strain data are obtained from simple compression tests until 90% plastic strain. The measurement of the local strain is performed in a tensile test at 19.8% plastic strain (Commentz, 2000). An elasto-viscoplastic material model is used to investigate the plastic properties of the aforementioned two-phase polycrystals. Caused by the complex local deformation mechanisms, the rule of mixture is insufficient to describe the stress-strain behaviour of such polycrystals. Due to limited experimental data for Fe-Cu composites, material parameters of the two-phase composites are obtained from the modification of input parameters of pure iron and copper. The axisymmetric and the three-dimensional simulations are performed by the finite element software ABAQUS. In order to study the influence of the local micromechanical properties on the macroscopic material behaviour, material structures are modelled based on real microscopic cut-outs which are used as cross sections in axisymmetric simulations. In these structures, regions near grain boundaries are finer meshed than other parts. Two composites, i.e., Fe17-Cu83 and Fe50-Cu50, are taken as representative microstructures which are investigated carefully. 3D models with Poisson Voronoi microstructures and periodic boundary conditions are performed for the aforementioned seven polycrystals. We incorporate the micro-morphology,

the grain orientation, and the local interaction in the simulation to numerically study the flow behaviour, the crystallographic texture, and the distribution of the strain.

The following conclusions are obtained for the mechanical behaviour of pure iron, copper, and their composites from the numerical and experimental results.

- **Misorientation Distribution**

  In the axisymmetric simulations, there is only a slight difference between the mean value of misorientation in the iron phase and that in the copper phase, where the misorientation is defined as the distance of the crystal orientation from its initial one.

- **Stress Strain Behaviour**

1. When the local stress is influenced only by initial grain orientations in a given microstructure, i.e., all other conditions are kept identical in axisymmetric simulations, a deviation of 5% to 10% is shown for the local stress normalised by the macroscopic stress in the simulation.
2. The stress of the iron or the copper phase, which is normalised by the total stress ($\sigma^{Fe}/\sigma^{comp.}$, $\sigma^{Cu}/\sigma^{comp.}$), in 3D predictions indicates that the stress of the copper phase increases rapidly and that of the iron phase decreases at the beginning of the yielding.
3. The normalised stress of the iron and the copper phase, which is defined as the ratio of the stress of the iron or copper phase to the stress of composite, converge to different values in the 3D simulations. The ratio of the copper phase stress to the total stress is higher for the composite with a fewer iron-phase content while this ratio is relatively constant for the iron phase.

- **Crystallographic Texture**

1. In the axisymmetry case, the simulated texture of the iron phase describes well the experimental fibre texture. The predicted texture of the Cu phase also captures the experimental fibre texture in the Fe17-Cu83 composite. Due to the limited number of grains in the microstructure for the simulation, the Fe50-Cu50 composite presents a higher fibre intensity than the Fe17-Cu83 composite, which is not the case in the experiment.

2. For both types of composites in the 3D predictions, the presence of the second phase even with a small amount of the volume fraction drastically reduces the sharpness of the crystallographic texture in both phases.
3. The maximum fibre intensities (<100>- and <111>-fibre) of the iron phase are similar for composites of Fe17-Cu83 v.s. Fe83-Cu17 and Fe33-Cu67 vs. Fe67-Cu33. Simulation results predicted by the 3D model capture the above mentioned maximum fibre intensity for the Fe33-Cu67 and the Fe67-Cu33 composite.
4. Without considering the Fe50-Cu50 composite in the 3D case, the fibre intensity (<110>-fibre) of the copper phase increases with a decreasing harder phase content. The same phenomenon for the <110>-fibre is observed in the experiment. This means that the harder phase has a stronger influence on the texture evolution of the softer phase than vice versa.
5. The phase interaction exhibits a significant effect on the texture since the softest texture is shown in the interpenetrating network of the iron and the copper phases (Fe50-Cu50), especially in the copper phase.

• **Strain Distribution**

1. In the normal and the transverse direction, the mean value of the strain in both the harder phase and the softer phase presents a deviation from the total mean value, and the copper phase undergoes larger deformation than the iron phase in the composite. These properties are well predicted by both the axisymmetric and the 3D simulations.
2. The mean value of the strain is quantitatively well predicted for both the iron and the copper phases. This mean value is about 0% in the shear direction for both phases. The deviation of the mean value between the experiment and the prediction is 16% in the transverse direction for the copper phase in the axisymmetric simulation, while this deviation is about 0% in the loading direction. The corresponding values are 14% and ≈0% in the 3D case. For the iron phase, this deviation is 1.4% in the transverse direction and 11% in the loading direction in the axisymmetric simulation and they are 7% and 1.9% in the 3D case, respectively.

For a quantitatively good prediction of the fibre intensity evolution according to the variation of the phase volume fraction, a more realistic activation mechanism

of slip systems should be applied instead of the isotropic hardening, especially for the bcc phase in bcc-fcc composites. If pencil glide systems are considered for the iron phase, it may be possible to give even better results than those presented in this work for the fibre texture. Since the microstructure is also essential for the plastic deformation behaviour of polycrystals, numerical predictions should be improved if a 3D finite element model is used which is based on the real 3D morphology and with a relatively large amount of grains, e.g., approximately 500 grains for each phase.

Appendix A

Numerical Time Integration

A.1 Elasto-viscoplastic Material Model

The differential equation systems for $\tilde{\boldsymbol{F}}$ can be obtained by reforming equation (3.46), i.e.,

$$\begin{aligned} \dot{\tilde{\boldsymbol{F}}}(\tilde{\boldsymbol{F}}, \tau^C) &= \boldsymbol{L}\tilde{\boldsymbol{F}} - \tilde{\boldsymbol{F}}\tilde{\boldsymbol{k}}(\tilde{\boldsymbol{T}}, \tau^C) \\ \text{with} & \\ \tilde{\boldsymbol{T}} &= \tilde{\boldsymbol{F}}^{\mathsf{T}}\boldsymbol{T}^K\tilde{\boldsymbol{F}}^{-\mathsf{T}} = \tilde{\boldsymbol{C}}\tilde{\boldsymbol{T}}^{2PK}. \end{aligned} \tag{A.1}$$

$\tilde{\boldsymbol{T}}$ is the Mandel tensor in the undistorted placement. At room temperature, fcc materials can be approximately taken as isotropic hardening for all the slip systems, i.e., $\tau_\alpha^C = \tau^C$ (Kocks and Mecking, 2003). The differential equation for the hardening (3.52) has the form of

$$\dot{\tau}^C(\tau_\alpha, \tau^C) = \dot{\tau}^C(\tilde{\boldsymbol{F}}, \tau^C). \tag{A.2}$$

Since the evolution equations of (A.1) and (A.2) are coupled, $\tilde{\boldsymbol{F}}$ and τ^C can be written together in a vector $\boldsymbol{h}$ for further consideration.

By applying the backward (implicit) Euler method to solve the equation systems $\dot{\boldsymbol{h}}(\tilde{\boldsymbol{F}}, \tau^C)$,

$$\boldsymbol{h}_{n+1} = \boldsymbol{h}_n + \triangle t \dot{\boldsymbol{h}}_{n+1} \tag{A.3}$$

is used for the time increment $\triangle t$. Obviously, $\boldsymbol{h}_{n+1}$ depends on the $\tilde{\boldsymbol{F}}$ and τ^C at the time steps $t = n$ and $t = n + 1$. The Newton method is preferred to solve the nonlinear equation system $\boldsymbol{g}(\tilde{\boldsymbol{F}}_{n+1}, \tau^C_{n+1})$.

$$\boldsymbol{g}(\tilde{\boldsymbol{F}}_{n+1}, \tau^C_{n+1}) = \boldsymbol{h}_{n+1} - \boldsymbol{h}_n - \triangle t \dot{\boldsymbol{h}}_{n+1} \tag{A.4}$$

The Jacobian matrix

$$\boldsymbol{J}_{n+1} = \frac{\partial \boldsymbol{g}_{n+1}}{\partial \boldsymbol{h}_{n+1}} \tag{A.5}$$

is analytically specified. Since the backward Euler scheme does not preserve the incompressibility condition $\det(\boldsymbol{P}) = \det(\boldsymbol{F}_p) = 1$ (see equations (3.23), (3.32) for $\boldsymbol{P}$ and $\boldsymbol{F}_p$) by nature, a correction of the numerical solution is applied following Böhlke (2001), i.e.,

$$\tilde{\boldsymbol{F}}^*_{n+1} = \sqrt[3]{\frac{\det(\boldsymbol{F})_{n+1}}{\det(\tilde{\boldsymbol{F}})_{n+1}}}\, \tilde{\boldsymbol{F}}_{n+1}. \tag{A.6}$$

Shown in (A.1) and (3.13), $\dot{\tilde{\boldsymbol{F}}}$ and $\boldsymbol{F}$ relate to the velocity gradient $\boldsymbol{L}$. $\boldsymbol{L}_{n+1}$ can be approximated by

$$\boldsymbol{L}_{n+1} = \frac{1}{\triangle t}(\boldsymbol{F}_{n+1} - \boldsymbol{F}_n)\boldsymbol{F}^{-1}_{n+1}. \tag{A.7}$$

The initial condition is considered as

$$\begin{aligned} \tilde{\boldsymbol{F}}(t=0) &= \boldsymbol{Q}(t=0), \\ \tau^C(t=0) &= \tau^C_0. \end{aligned} \tag{A.8}$$

The orthogonal tensor $\boldsymbol{Q} \in SO(3)$ defines the basis of the crystal orientation. This tensor maps the orthonormal (sample) basis $\{\boldsymbol{e}_i\}$ to the orthonormal lattice basis $\{\boldsymbol{g}_i\}$, i.e.

$$\boldsymbol{Q} = \boldsymbol{g}_i \otimes \boldsymbol{e}_i. \tag{A.9}$$

A.2 Viscoplastic Material Model

In order to solve the differential equation of (3.56b) which specifies the evolution of the crystal orientation, the Kirchhoff stress (deviator part $\boldsymbol{T}^{K'}$) should be firstly specified from equation (3.56a). At time t_n, $\boldsymbol{T}^{K'}$ can be expressed in terms of the orientation tensor $\boldsymbol{Q}_n$, and the deviator part of the strain rate tensor $\boldsymbol{D'}$ (see equation (3.16)). $\boldsymbol{D'}$ can be prescribed from $\boldsymbol{L}$ for each time step. Since $\boldsymbol{T}^{K'}$ and $\boldsymbol{D'}$ are symmetric and traceless, they can be formulated in a 5-dimensional vector with the basis $\{\boldsymbol{B}_\alpha\}$ where

$$\begin{aligned} T^{K'} &= \left[\sqrt{\frac{3}{2}}T_{11}^{K'} \ \sqrt{\frac{1}{2}}(T_{22}^{K'} - T_{33}^{K'}) \ \sqrt{2}T_{23}^{K'} \ \sqrt{2}T_{13}^{K'} \ \sqrt{2}T_{12}^{K'}\right] B_i, \\ D' &= \left[\sqrt{\frac{3}{2}}D'_{11} \ \sqrt{\frac{1}{2}}(D'_{22} - D'_{33}) \ \sqrt{2}D'_{23} \ \sqrt{2}D'_{13} \ \sqrt{2}D'_{12}\right] B_i. \end{aligned} \tag{A.10}$$

The corresponding basis $\{\boldsymbol{B}_\alpha\}$ is defined as

$$\begin{aligned} \boldsymbol{B}_1 &= \frac{1}{\sqrt{6}}(2\boldsymbol{e}_1 \otimes \boldsymbol{e}_1 - \boldsymbol{e}_2 \otimes \boldsymbol{e}_2 - \boldsymbol{e}_3 \otimes \boldsymbol{e}_3), \\ \boldsymbol{B}_2 &= \frac{1}{\sqrt{2}}(\boldsymbol{e}_2 \otimes \boldsymbol{e}_2 - \boldsymbol{e}_3 \otimes \boldsymbol{e}_3), \\ \boldsymbol{B}_3 &= \frac{1}{\sqrt{2}}(\boldsymbol{e}_2 \otimes \boldsymbol{e}_3 + \boldsymbol{e}_3 \otimes \boldsymbol{e}_2), \\ \boldsymbol{B}_4 &= \frac{1}{\sqrt{2}}(\boldsymbol{e}_1 \otimes \boldsymbol{e}_3 + \boldsymbol{e}_3 \otimes \boldsymbol{e}_1), \\ \boldsymbol{B}_5 &= \frac{1}{\sqrt{2}}(\boldsymbol{e}_1 \otimes \boldsymbol{e}_2 + \boldsymbol{e}_2 \otimes \boldsymbol{e}_1). \end{aligned} \tag{A.11}$$

Analogously to equation (A.4) and at the time t_n, equation (3.56a) can be written in the form of

$$\boldsymbol{G}_n = (\boldsymbol{D}_n{}', \boldsymbol{Q}_n, \boldsymbol{T}^{K\prime}) = \boldsymbol{0} \tag{A.12}$$

with the 5-dimensional basis. The Jacobian matrix

$$\boldsymbol{J}_n{}' = \frac{\partial \boldsymbol{G}_n}{\partial \boldsymbol{T}^{K\prime}} \tag{A.13}$$

is a 5×5 dimension matrix. The Newton method is applied to find the solution of the equation systems. With $\boldsymbol{T}^{K\prime}$ at the time t_n, $\boldsymbol{Q}_{n+1}$ can be calculated at the time t_{n+1}. Equation

$$\boldsymbol{W}^* = \boldsymbol{Q}^{\mathsf{T}}\dot{\boldsymbol{Q}} = \boldsymbol{Q}^{\mathsf{T}}\boldsymbol{W}\boldsymbol{Q} - skw(\tilde{\boldsymbol{K}}(\boldsymbol{Q}^{\mathsf{T}}\boldsymbol{T}^{K\prime}\boldsymbol{Q}, \tau^C)) \tag{A.14}$$

is reformed from equation (3.56b). An explicit exponential method is used to solve the differential equation (A.14) (Weber and Anand, 1990; Miehe, 1996), i.e.,

$$\boldsymbol{Q}_{n+1} = \boldsymbol{Q}_n \exp(\boldsymbol{W}^* \triangle t). \tag{A.15}$$

The critical resolved shear stress can be explicitly updated by

$$\tau^C{}_{n+1} = \tau^C{}_n + \triangle t \dot{\tau}^C(\boldsymbol{Q}_n, \tau^C_n). \tag{A.16}$$

Using $\boldsymbol{Q}_{n+1}$ and $\tau_{\alpha n+1}$ as input, the Kirchhoff stress $\boldsymbol{T}^K_{n+1}$ can be solved through equation (3.56a).

Appendix B

Slip Systems and Representation of Crystallographic Texture

B.1 Slip Systems

Table B.1 presents the considered glide systems, {111}<110>, for the fcc (copper) crystals (Böhlke, 2001). Glide systems, {110}<111>, for bcc Fe are given in Table B.2 (Nemat-Nasser *et al.*, 1998).

α	1	2	3	4	5	6
$\sqrt{2}\ \tilde{d}^i_\alpha$	[1,0,-1]	[-1,1,0]	[0,-1,1]	[0,1,-1]	[-1,-1,0]	[1,0,1]
$\sqrt{3}\ \tilde{n}^i_\alpha$	(1,1,1)	(1,1,1)	(1,1,1)	(-1,1,1)	(-1,1,1)	(-1,1,1)
α	7	8	9	10	11	12
$\sqrt{2}\ \tilde{d}^i_\alpha$	[-1,0,-1]	[1,-1,0]	[0,1,1]	[0,-1,-1]	[1,1,0]	[-1,0,1]
$\sqrt{3}\ \tilde{n}^i_\alpha$	(-1,-1,1)	(-1,-1,1)	(-1,-1,1)	(1,-1,1)	(1,-1,1)	(1,-1,1)

Table B.1: The glide direction ($\tilde{\boldsymbol{d}}_\alpha$) and the normal direction ($\tilde{\boldsymbol{n}}_\alpha$) of glide planes for fcc glide systems.

B.2 Standard Inverse Pole Figure

To obtain the numerically solved standard inverse pole figure, the orthogonal part $\boldsymbol{R}_e$ of $\tilde{\boldsymbol{F}}$ ($\tilde{\boldsymbol{F}} = \boldsymbol{R}_e\boldsymbol{U}_e$) is taken as the input for crystal orientations ($\boldsymbol{Q}$ in equation

α	1	2	3	4	5	6
$\sqrt{3}\,\tilde{d}^i_\alpha$	[-1,1,1]	[1,-1,1]	[1,1,1]	[1,1,-1]	[1,1,-1]	[-1,1,1]
$\sqrt{2}\,\tilde{n}^i_\alpha$	(1,1,0)	(1,1,0)	(1,-1,0)	(1,-1,0)	(1,0,1)	(1,0,1)
α	7	8	9	10	11	12
$\sqrt{3}\,\tilde{d}^i_\alpha$	[1,1,1]	[1,-1,1]	[1,1,-1]	[1,-1,1]	[1,1,1]	[-1,1,1]
$\sqrt{2}\,\tilde{n}^i_\alpha$	(1,0,-1)	(1,0,-1)	(0,1,1)	(0,1,1)	(0,1,-1)	(0,1,-1)

Table B.2: The glide direction ($\tilde{\boldsymbol{d}}_\alpha$) and the normal direction ($\tilde{\boldsymbol{n}}_\alpha$) of glide planes for bcc $\{110\}\langle 111\rangle$ glide systems.

(3.56) for the viscoplastic material law). The Bunge convention (Bunge, 1993) for Euler angles are used during the texture calculation, i.e.,

$$R_{ij} = \begin{bmatrix} \cos\varphi_1\cos\varphi_2 - \sin\varphi_1\cos\Phi\sin\varphi_2 & \sin\varphi_1\cos\varphi_2 + \cos\varphi_1\cos\Phi\sin\varphi_2 & \sin\Phi\sin\varphi_2 \\ -\cos\varphi_1\sin\varphi_2 - \sin\varphi_1\cos\Phi\cos\varphi_2 & -\sin\varphi_1\sin\varphi_2 + \cos\varphi_1\cos\Phi\cos\varphi_2 & \sin\Phi\cos\varphi_2 \\ \sin\varphi_1\sin\Phi & -\cos\varphi_1\sin\Phi & \cos\Phi \end{bmatrix}.$$

The conversion among different conventions for Euler angles is given in Table B.3.

Bunge	Roe	Canova	Kocks
φ_1	$\alpha = \varphi_1 - \frac{\pi}{2}$	$\omega = -\varphi_1$	$\Psi = \varphi_1 - \frac{\pi}{2}$
Φ	β	$-\Theta$	Θ
φ_2	$\gamma = \varphi_2 - \frac{3\pi}{2}$	$\phi = -\varphi_2$	$\phi = \frac{\pi}{2} - \varphi_2$

Table B.3: The relationship among different conventions for the three Euler angles.

The crystallographic texture can be quantitatively described by the orientation distribution function (ODF). For the approximation of the ODF, a central distribution function can be used, e.g., the Mises-Fischer distribution function (Eschner, 1995). This distribution function (the Mises-Fischer distribution) ensures the requirement of the non-negativity for the ODF. Pole and inverse pole figures can be calculated from the ODF. By applying the Mises-Fischer distribution function, (Böhlke *et al.*, 2006a) considered the problem of approximating a given crystallite ODF by a set of texture components. Instead of the Mises-Fischer distribution functioon, the ODF can also be presented by the tensorial Fourier series. Generally, the nonnegativity of the ODF is not ensured by this (tensorial Fourier coefficient) approach. (Böhlke, 2005) extented the Fourier coefficient approach of

the ODF. In this work, maximum entropy method is applied to estimate the crystallite ODF, where a coordinate-free representation of the distribution is given. By using this maximum entropy approach, a derivation of the evolution equation of the tensorial texture coefficients of the crystallite ODF is given in (Böhlke, 2006).

All the standard inverse pole figures are projected to the normal plane in the present work. In the experiment, the texture is plotted in a 5 grid with the Berkeley texture package (Wenk and Matthies, 1997)[1] developed by Matthies and his co-workers. The Euler angles, φ_1 and φ_2, are presented in Figure B.1 for a crystal orientation projected to the normal (loading) direction. The half-width[2] for the distribution function is chosen as 15. All textures of numerical predictions, including both the axisymmetric and the 3D simulation, are plotted in a 2 increment[3] in both the φ_1 and the φ_2 directions.

Figure B.2 shows the three poles, <001>, <101> and <111>, for the standard inverse pole figure and the fibres, <114> and <102>, which are typical for the copper texture.

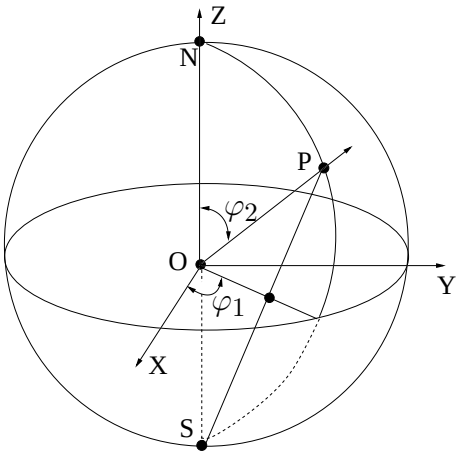

Figure B.1: A sketch of the presentation of the Euler angles,φ_1 and φ_2, with a crystal orientation projected to the normal (loading) direction.

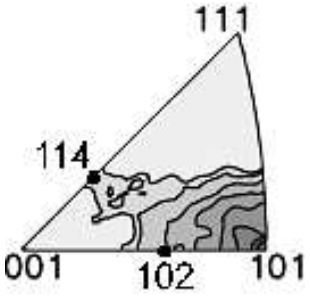

Figure B.2: Texture of single phase (pure) copper under the compressive load at 90% plastic strain (Commentz, 2000).

[1]The standard Euler convention is the Roe convention in this package (programme).

[2]The half-width chosen in the experiment is not equal to 15.

[3]This choice is calculating time favourite and provides the texture in a better quality than in 5. This may be one of the reasons why the simulated textures look smoother than the experimental ones.

Bibliography

ABAQUS/Standard (2003). Hibbitt, Karlsson & Sorensen, Inc.

Acharya, A. and Beaudoin, A. (2000). Grain-size effect in viscoplastic polycrystals at moderate strains. *J. Mech. Phy. Solid*, **48**, 2213–2230.

Allais, L., Bornert, M., Bretheau, T., and Caldemaison, D. (1994). Experimental characterization of the local strain field in a heterogeneous elastoplastic material. *Acta. metall. Mater.*, **42**, 3865–3880.

Andersson, J. (2005). The influence of grain size variation on metal fatigue. *Int. J. Fatigue*, **27**, 847–852.

Asaro, R. J. and Needleman, A. (1985). Overview No. 42: Texture development and strain hardening in rate dependent polycrystals. *Acta Metall.*, **33**, 923–953.

Bertram, A. (1992). Description of finite inelastic deformations. In A. Benallal, R. Billardon, and D. Marquis, editors, *Proceedings of MECAMAT'92, International Seminar on Multiaxial Plasticity*, pages 821–835.

Bertram, A. (1999). An alternative approach to finite plasticity based on material isomorphisms. *Int. J. Plast.*, **15**(3), 353–374.

Bertram, A. (2005). *Elasticity and Plasticity of Large Deformations - an Introduction*. Springer-Verlag.

Bertram, A. and Kraska, M. (1995a). Description of finite plastic deformations in single crystals by material isomorphisms. In D. F. Parker and A. H. England, editors, *Proceedings of IUTAM Symposium on Anisotropy, Inhomogeneity and Nonlinearity in Solid Mechanics, 30.8.-3.9.1994 Nottingham*, pages 77–90.

Bertram, A. and Kraska, M. (1995b). Determination of finite plastic deformations in single crystals. *Arch. Mech.*, **47**(2), 203–222.

Bertram, A. and Olschewski, J. (1991). Formulation of anisotropic linear viscoelastic constitutive laws by a projection method. In A. Freed and K. Walker, editors, *High temperature constitutive modelling: Theory and Application*, pages 129–137. ASME. MD-Vol. 26, AMD-Vol. 121.

Bertram, A., Böhlke, T., and Kraska, M. (1997). Numerical simulation of deformation induced anisotropy of polycrystals. *Comp. Mat. Sci.*, **9**, 158–167.

Berveiller, M. and Zaoui, A. (1979). An extension of the self-consistent scheme to plastically-flowing polycrystals. *J. Mech. Phys. Solids*, **26**, 325–344.

Böhlke, T. (2001). *Crystallographic Texture Evolution and Elastic Anisotropy: Simulation, Modeling, and Applications*. Aachen: Shaker Verlag. Dissertation, Fakultät für Maschinenbau, Otto-von-Guericke-Universität Magdeburg.

Böhlke, T. (2004). The Voigt bound of the stress potential of isotropic viscoplastic FCC polycrystals. *Arch. Mech.*, **56**(6), 425–445.

Böhlke, T. (2005). Application of the maximum entropy method in texture analysis. *Comp. Mat. Sci.*, **32**, 276–283.

Böhlke, T. (2006). Texture simulation based on tensorial Fourier coefficients. *Computers and Structures*, **84**, 1086–1094.

Böhlke, T., Kraska, M., and Bertram, A. (1997). Simulation der einfachen Scherung einer polykristallinen Aluminiumprobe. *Technische Mechanik, Sonderheft*, **47–54**.

Böhlke, T., Risy, G., and Bertram, A. (2005). A texture component model for anisotropic polycrystal plasticity. *Comp. Mat. Sci.*, **32**, 284–293.

Böhlke, T., Haus, U., and Schulze, V. (2006a). Crystallographic texture approximation by quadratic programming. *Acta Mater.*, **54**, 1359–1368.

Böhlke, T., Risy, G., and Bertram, A. (2006b). Finite element simulation of metal forming operations with texture based material models. *Modelling Simul. Mater. Sci. Eng.*, **14**, 365–387.

Bronkhorst, C., Kalidindi, S., and Anand, L. (1992). Polycrystalline plasticity and the evolution of crystallographic texture in fcc metals. *R. Soc. Lond.*, **A341**, 443–477.

Budianski, B. and Wu, T. (1962). Theoretical prediction of plastic strains of polycrystals. In *Proceeding of the 4th US National Congress of Applied Mechanics, Trans. of the ASME*, pages 1175–1185.

Bunge, H.-J. (1993). *Texture Analysis in Material Science*. Cuviller Verlag Göttingen.

Canova, G., Fressengeas, C., Mólinari, A., and Kocks, U. (1988). Effect of rate sensitivity on slip system activity and lattice rotation. *Acta Metall.*, **36(8)**, 1961–1970.

Canova, G., Wenk, H., and Molinari, A. (1992). Deformation modelling of multiphase polycrystals: Case of quartz-mica aggregate. *Acta Metall. Mater.*, **40**(7), 1519–1530.

Cheong, K. and Busso, E. (2006). Effects of lattice misorientations on strain heterogeneities in FCC polycrystals. **54**, 671–689.

Commentz, B. (2000). *Plastische Verformung von zweiphasigen Eisen-Kupfer-Verbundwerkstoffen*. Dissertation, Technische Universität Hamburg-Harburg. Shaker Verlag.

Commentz, B., Hartig, C., and Mecking, H. (1999). Micromechanical interaction in two-phase iron-copper polycrystals. *Comp. Mat. Sci.*, **16**, 237–247.

Cowin, S. (1989). Properties of the anisotropic elasticity tensor. *Q. J. Mech. appl. Math.*, **42**, 249–266.

Dawson, P., Needleman, A., and Suresh, S. (1994). Issues in the finite element modeling of polyphase plasticity. *Mat. Sci. Eng.*, **A175**, 43–48.

Daymond, M. R., Hartig, C., and Mecking, H. (2005). Interphase and intergranular stress generation in composites exhibiting plasticity in both phases. *Acta. Mater.*, **53**, 2805–2813.

deBotton, G. and Ponte Castaneda, P. (1995). Variational estimates for the creep behavior of polycrystals. *Proc. R. Soc. Lond.*, **A448**, 121–142.

Eschner, T. (1995). *Quantitative Texturanalyse durch Komponentenzerlegung von Beugungspolfiguren*. Laborbericht PTB-7.4-95-1. Physikalisch-Technische Bundesanstalt, Braunschweig und Berlin, Abteilung Neutronenphysik.

Eshelby, J. (1957). The determination of the elastic field of an ellipsoidal inclusion, and related problems. *Proc. R. Soc. London*, **A241**, 376–396.

Forest, S. (1996). *Mechanical modelling of non-homogeneous deformation of single crystals*. Thesis, Ecole des Mines de Paris.

Forte, S. and Vianello, M. (1996). Symmetry classes for elasticity tensors. *J. Elast.*, **43**, 81–108.

Gambin, W. (2001). *Plasticity and Textures*. Kluwer Academic Publishers.

Gottstein, G. (2001). *Physikallische Grundlagen der Materialkunde*. Springer, 2 edition.

Hangen, U. and Raabe, D. (1995). Modelling of the yield strength of a heavily wire drawn Cu-20%Nb composite by use of a modified linear rule of mixtures. *Acta metall. mater.*, **43**(11), 4075–4082.

Harder, J. (1997). Simulation lokaler Fließvorgänge in Polykristallen. In *Braunschweiger Schriften zur Mechanik Nr. 28*. Institut für Allgemeine Mechanik und Festigkeitslehre, TU Braunschweig.

Harder, J. (1999). A crystallographic model for the study of local deformation processes in polycrystals. *Int. J. Plast.*, **15**, 605–624.

Harren, S., Lowe, T., Asaro, R., and Needleman, A. (1989). Analysis of large-strain shear in rate-dependent face-centred cubic polycrystals: Correlation of micro- and macromechanics. *Phil. Trans. R. Soc. Lond.*, **A328**, 443–500.

Hartig, C. and Mecking, H. (2005). Finite element modelling of two-phase Fe-Cu polycrystals. *Comp. Mat. Sci.*, **32**, 370–377.

Haupt, P. (2000). *Continuum Mechanics and Theory of Materials*. Springer.

Hershey, A. and Dahlgren, V. (1954). The elasticity of an isotropic aggregate of anisotropic cubic crystals. *J. Appl. Mech.*, **21**, 236–241.

Hill, R. (1963). Elastic properties of reinforced solids: some theoretical principles. *J. Mech. Phys. Solids*, **11**, 357–372.

Hill, R. (1965). Continuum micro-mechanics of elastoplastic polycrystals. *J. Mech. Phys. Solids*, **13**, 89–101.

Honneff, H. and Mecking, H. (1978). A method for the determination of the active slip systems and orientation changes during single crystal deformation. In G. Gottstein and K. Lücke, editors, *Textures of Materials*, pages 265–275.

Hutchinson, J. (1970). Elastic-plastic behavior of polycrystalline metals and composites. *Proc. R. Soc. Lond.*, **A319**, 247–272.

Hutchinson, J. (1976). Bounds and self-consistent estimates for creep of polycrystalline materials. *Proc. R. Soc. Lon.*, **A348**, 101–127.

Kabir, M., Lutz, W., Zhu, K., and Schmauder, S. (2006). Fatigue modeling of short fiber reinforced composites with ductile matrix under cyclic loading. *Comp. Mat. Sci.*, **36**, 361–366.

Kallend, J., Kocks, U., Rollett, A., and Wenk, H.-R. (1991). Operational texture analysis. *Mat. Sci. Eng.*, **A132**, 1–11.

Kocks, U. (1976). Laws for work-hardening and low-temperature creep. *J. Eng. Mater. Techn. (ASME)*, **98**, 75–85.

Kocks, U. and Mecking, H. (2003). Physics and phenomenology of strain hardening: the FCC case. *Progr. Mat. Sci.*, **48**, 171–273.

Kocks, U., Tome, C., and Wenk, H. (1998). *Texture and Anisotropy: Preferred Orientations in Polycrystals and Their Effect on Materials Properties*. Cambridge Univ. Pr.

Kraska, M. (1998). *Textursimulation bei großen inelastischen Verformungen mit der Technik des repräsentativen Volumenelements (RVE)*. Pro BUSINESS. Dissertation, TU Berlin.

Kröner, E. (1958). Berechnung der elastischen Konstanten der Vielkristalls aus den Konstanten des Einkristalls. *Z. Phys.*, **151**, 504–518.

Kröner, E. (1961). Zur plastischen Verformung des Vielkristalls. *Acta. Metall.*, **9**, 155–161.

Kubaschewski, O. (1982). *Iron binary phase diagrams*. Springer.

Lebensohn, R. and Tomè, C. (1993). A self-consistent anisotropic approach for the simulation of plastic deformation and texture development of polycrystals: application to zirconium alloys. *Acta Metall. Mater.*, **41**, 2611–2624.

Lee, Y., Subhash, G., and Ravichandran, G. (1999). Constitutive modeling of textured body-centered-cubic (bcc) polycrystals. *Int. J. Plast.*, **15**, 625–645.

Leffers, T. (1968). *Texturen in Forschung und Praxis*, **184**. Riso. Rep.

Li, H., Li, K., Subhash, G., Kecskes, L., and Dowding, R. (2006). Micromechanical modeling of tungsten-based bulk metallic glass matrix composites. *Mater. Sci. Eng.*, **A429**, 115–123.

Li, Z. and Schmauder, S. (2000). Phase-stress partition and residual stress in metal matrix composites. *Comp. Mater. Sci.*, **18**, 295–302.

LLorca, J. and Segurado, J. (2004). Three-dimensional multiparticle cell simulations of deformation and damage in sphere-reinforced composites. *Mat. Sci. Eng.*, **A365**, 267–274.

Logé, R. and Chastel, Y. (2006). Coupling the thermal and mechanical fields to metallurgical evolutions within a finite element description of a forming process. *Comput. Methods Appl. Mech. Engrg*, **195**, 6843–6857. in press.

Lubarda, V. (2002). *Elastoplasticity Theory*. CRC Press.

Matthies, S. and Wenk, H. (1992). Optimization of texture measurements by pole figure coverage with hexagonal grids. *Phys. Stat. Sol. (a)*, **133**, 253–257.

Mecking, H. (1981). Computer simulation of texture development. In *Sixth Int. Conf. on Textures of Materials, Tokyo*, pages 53–66.

Mediavilla, J., Peerlings, R., and Geers, M. (2006). A robust and consistent remeshing-transfer operator for ductile fracture simulations. *Computers and Structures*, **84**, 604–623.

Méric, L., Cailletaud, G., and Gaspérini, M. (1994). F.E. calculations of copper bicrystal specimens submitted to tension-compression tests. *Acta metall. mater.*, **42**(3), 921–935.

Miehe, C. (1996). Exponential map algorithm for stress updates in anisotropic multiplicative elastoplasticity for single crystals. *Int. J. Num. Meth. Eng.*, **39**, 3367–3390.

Miehe, C. and Schotte, J. (2004). Anisotropic nite elastoplastic analysis of shells: simulation of earing in deep-drawing of single- and polycrystalline sheets by taylor-type micro-to-macro transitions. *Comput. Methods Appl. Mech. Eng.*, **193**, 25–57.

Miehe, C., Schröder, J., and Schotte, J. (1999). Computational homogenization in finite plasticity. Simulation of texture development in polycrystalline materials. *Comp. Meth. Appl. Mech. Engng.*, **171**, 387–418.

Mishnaevsky, L. J. and Schmauder, S. (1999). Advanced finite element techniques of analysis of the microstructure - mechanical properties relationships in heterogeneous materials: a review. *Physical Mesomech.*, **2**(3), 5–20.

Molinari, A., Canova, G., and Ahzi, S. (1987). A self consistent approach of the large deformation polycrystal viscoplasticity. *Acta metall.*, **35**(12), 2983–2994.

Nebozhyn, M., Gilormini, P., and Castaneda, P. (2001). Variational self-consistent estimates for cubic viscoplastic polycrystals: the effects of grain anisotropy and shape. *J. Mech. Phys. Solids*, **49**, 313–340.

Nemat-Nasser, S., Okinaka, T., and Ni, L. (1998). A physically-based constitutive model for bcc crystals with application to polycrystalline tantalum. *J. Mech. Phys. Solids*, **46**(6), 1009–1038.

NIST (2003). *OOF: Object-Oriented Finite Element Analysis of Real Material Microstructures Working Group*. ppm2oof1.1.24. NIST: National Institute of Standards and Technology. http://www.ctcms.nist.gov/oof.

Nygards, M. and Gudmundson, P. (2002a). Micromechanical modeling of ferritic/pearlitic steels. *Mater. Sci. Eng.*, **A325**, 435–443.

Nygards, M. and Gudmundson, P. (2002b). Three-dimensional periodic Voronoi grain models and micromechanical FE-simulations of a two-phase steel. *Comp. Mater. Sci.*, **24**, 513–519.

Ogden, R. (1972). Large deformation isotropic elasticity: on the correlation of theory and experiment for compressible rubberlike materials. *Proc. Royal. Soc. Lond.*, **A328**, 567–583.

Ohser, J. and Mücklich, F. (2000). *Statistical analysis of microstructures in materials science*. John Wiley & Sons, Ltd.

Peirce, D., Asaro, R., and Needleman, A. (1982). Overview 21: An analysis of nonuniform and localized deformation in ductile single crystals. *Acta Metall.*, **30**, 1087–1119.

Popla (8918). *Preferred orientation package Los Alamos*. Los Alamos Naional Lab. LA-CC-89-18, Los Alamos, NM 87545, U.S.A.

Raabe, D., Heringhaus, F., Hangen, U., and Gottstein, G. (1995). Investigation of a Cu-20 mass% Nb in situ composite Part I: fabrication, microstructure and mechanical properties. *Z. Metallkd.*, **86**(6), 405–415.

Raabe, D., Sachtleber, M., Weiland, H., Scheele, G., and Zhao, Z. (2003). Grain-scale micromechanics of polycrystal surfaces during plastic straining. *Acta Mater.*, **51**, 1539–1560.

Ratke, L., Stark, J., and Wassermann, G. (1984). Age hardening of Fe-Cu-composite wires. *Scripta Metallurgica*, **18**, 137–140.

Reuss, A. (1929). Berechnung der Fließgrenze von Mischkristallen auf Grund der Plastizitätsbedingung für Einkristalle. *Z. Angew. Math. Mech.*, **9**(1), 49–58.

Rice, J. (1971). Inelastic constitutive relations for solids: An internal-variable theory and its application to metal plasticity. *J. Mech. Phys. Solids*, **19**, 433–455.

Rychlewski, J. and Zhang, J. (1989). Anisotropy degree of elastic materials. *Arch. Mech.*, **47**(5), 697–715.

Sachs, G. (1928). Zur Ableitung einer Fließbedingung. *Z. Verein dt. Ing.*, **72**, 734–736.

Sachtleber, M., Zhao, Z., and Raabe, D. (2002). Experimental investigation of plastic grain interaction. *Mater. Sci. Eng.*, **A336**, 81–87.

Schmid, E. (1924). Neuere Untersuchungen an Metallkristallen. *Proc. 1st. Int. Congr. Appl. Mech.*, **Delft**, 342–353.

Simo, J. and Miehe, C. (1992). Associative coupled thermoplasticity at finite stains: Formulation, numerical analyses and implementation. *Comp. Meth. Appl. Mech. Eng.*, **98**, 41–104.

Soppa, E., Amos, D., Schmauder, S., and Bischoff, E. (1998). The influence of second phase and/or grain orientations on deformation patterns in a Ag polycrystal and in Ag/Ni composites. *Comp. Mater. Sci.*, **13**, 168–176.

Soppa, E., Doumalin, P., Binkele, P., Wiesendanger, T., Bornert, M., and Schmauder, S. (2001). Experimental and numerical characterisation of in-plane deformation in two-phase materials. *Comp. Mater. Sci.*, **21**(3), 261–275.

Soppa, E., Schmauder, S., Fischer, G., Brollo, J., and Weber, U. (2003). Deformation and damage in Al/Al_2O_3. *Comp. Mater. Sci.*, **28**, 574–586.

Takahashi, H., Motohashi, H., and Tsuchida, S. (1996). Development of plastic anisotropy in rolled aluminim sheets. *Int. J. Plast.*, **12**(7), 935–949.

Tatschl, A. and Kolednik, O. (2003). On the experimental characterization of crystal plasticity in polycrystals. *Mat. Scie. Eng.*, **A356**, 447–463.

Taylor, G. (1938). Plastic strain in metals. *J. Inst. Metals*, **62**, 307–324.

Ting, T. (1996). *Anisotropic Elasticity: Theory and Applications*. Oxford University Press.

Tóth, L. and Molinari, A. (1994). Tuning a self consistent viscoplastic model by finite element results - II: application to torsion textures. *Acta metall. mater.*, **42**, 2459–2466.

Truesdell, C. and Noll, W. (1965). *The Non-Linear Field Theories of Mechanics*, volume III/3 of *Encyclopedia of Physics*. Springer.

Voigt, W. (1910). *Lehrbuch der Kristallphysik*. Teubner Leipzig.

Šilhavý, M. (1997). *The Mechanics and Thermodynamics of Continuous Media*. Springer.

Weber, G. and Anand, L. (1990). Finite deformation constitutive equations and a time integration procedure for isotropic, hyperelastic-viscoplastic solids. *Comp. Meth. Appl. Mech. Eng.*, **79**, 173–202.

Weng, G. (1981). Self-consistent determination of time-dependent behavior of metals. *J. Appl. Mech.*, **48**, 41–46.

Weng, G. (1982). A unified, self-consistent theory for the plastic-creep deformation of metals. *J. Appl. Mech.*, **49**, 728–734.

Wenk, H. and Matthies, S. (1997). *BEARTEX-Berkeley Texture Package v.1.0.*

Xia, Z., Zhang, Y., and Ellyin, F. (2003). A unified periodical boundary conditions for representative volume elements of composites and applications. *Int. J. Sol. Str.*, **40**, 1907–1921.

Yang, Q. and Qin, Q. (2004). Micro-mechanical analysis of composite materials by BEM. *Eng. Analy. Bound. Ele.*, **28**, 919–926.

Zhang, N. and Tong, W. (2004). An experimental study on grain deformation and interactions in an Al-0.5%Mg multicrystal. *Int. J. Plas.*, **20**, 523–542.

Zheng, Q.-S. and Boehler, J. (1994). The description, classification, and reality of material and physical symmetries. *Acta Mech.*, **102**, 73–89.

List of Figures

List of Tables